AFRL-AFOSR-VA-TR-2023-0235

The Mode Sensing Hypothesis

Wereley, Norman
MARYLAND UNIV COLLEGE PARK
230 W 41ST STREET FL 7
NEW YORK, NY,
US

12/29/2022
Final Technical Report

Air Force Research Laboratory
Air Force Office of Scientific Research
Arlington, Virginia 22203
Air Force Materiel Command

REPORT DOCUMENTATION PAGE

PLEASE DO NOT RETURN YOUR FORM TO THE ABOVE ORGANIZATION.

1. REPORT DATE
20221229

2. REPORT TYPE
Final

3. DATES COVERED

START DATE
20140315

END DATE
20200314

4. TITLE AND SUBTITLE
The Mode Sensing Hypothesis

5a. CONTRACT NUMBER

5b. GRANT NUMBER
FA9550-14-1-0068

5c. PROGRAM ELEMENT NUMBER
61102F

5d. PROJECT NUMBER

5e. TASK NUMBER

5f. WORK UNIT NUMBER

6. AUTHOR(S)
Norman Wereley

7. PERFORMING ORGANIZATION NAME(S) AND ADDRESS(ES)
MARYLAND UNIV COLLEGE PARK
230 W 41ST STREET FL 7
NEW YORK, NY
US

8. PERFORMING ORGANIZATION REPORT NUMBER

9. SPONSORING/MONITORING AGENCY NAME(S) AND ADDRESS(ES)
Air Force Office of Scientific Research
875 N. Randolph St. Room 3112
Arlington, VA 22203

10. SPONSOR/MONITOR'S ACRONYM(S)
AFRL/AFOSR RTB2

11. SPONSOR/MONITOR'S REPORT NUMBER(S)
AFRL-AFOSR-VA-TR-2023-0235

12. DISTRIBUTION/AVAILABILITY STATEMENT
A Distribution Unlimited: PB Public Release

13. SUPPLEMENTARY NOTES

14. ABSTRACT

The mode-sensing hypothesis (MSH) posits that insect sensorimotor systems are specifically matched to the natural modes of motion of the insect’s flight dynamics, which in turn are determined by the complex interaction of flight morphology, musculoskeletal output, and flight physics. The MSH Project seeks to validate this hypothesis through an interdisciplinary effort that combines theoretical, experimental and modeling approaches along with a comparative aspect across related dipteran fly species (hoverflies, blowflies, and fruit- flies).

15. SUBJECT TERMS

16. SECURITY CLASSIFICATION OF:

a. REPORT
U

b. ABSTRACT
U

c. THIS PAGE
U

17. LIMITATION OF ABSTRACT
UU

18. NUMBER OF PAGES
95

19a. NAME OF RESPONSIBLE PERSON
PATRICK BRADSHAW

19b. PHONE NUMBER *(Include area code)*
425-8492

Standard Form 298 (Rev.5/2020)
Prescribed by ANSI Std. Z39.18

REPORT DOCUMENTATION PAGE	*Form Approved* *OMB No. 0704-0188*

1. REPORT DATE *(DD-MM-YYYY)* 11/25/2020	**2. REPORT TYPE** Final Report	**3. DATES COVERED** *(From - To)* 4/1/2014-4/1/2020

4. TITLE AND SUBTITLE The Mode Sensing Hypothesis	**5a. CONTRACT NUMBER** N/A
	5b. GRANT NUMBER FA9550-14-1-0068
	5c. PROGRAM ELEMENT NUMBER N/A
6. AUTHOR(S) J. Sean Humbert, Holger G. Krapp and Graham K. Taylor	**5d. PROJECT NUMBER** N/A
	5e. TASK NUMBER N/A
	5f. WORK UNIT NUMBER N/A
7. PERFORMING ORGANIZATION NAME(S) AND ADDRESS(ES) University of Colorado Boulder 1111 Engineering Drive Boulder, CO 80309	**8. PERFORMING ORGANIZATION REPORT NUMBER** N/A
9. SPONSORING/MONITORING AGENCY NAME(S) AND ADDRESS(ES) AFOSR 801 N Randolph St. Arlington VA 22203	**10. SPONSOR/MONITOR'S ACRONYM(S)** AFOSR
	11. SPONSOR/MONITOR'S REPORT NUMBER(S) N/A

12. DISTRIBUTION/AVAILABILITY STATEMENT
Distribution A: Approved for public release

13. SUPPLEMENTARY NOTES

14. ABSTRACT

The mode-sensing hypothesis (MSH) posits that insect sensorimotor systems are specifically matched to the natural modes of motion of the insect's flight dynamics, which in turn are determined by the complex interaction of flight morphology, musculoskeletal output, and flight physics. The MSH Project seeks to validate this hypothesis through an interdisciplinary effort that combines theoretical, experimental and modeling approaches along with a comparative aspect across related dipteran fly species (hoverflies, blowflies, and fruit- flies).

15. SUBJECT TERMS
Insect sensorimotor systems; natural modes; flight dynamics

16. SECURITY CLASSIFICATION OF:			**17. LIMITATION OF ABSTRACT**	**18. NUMBER OF PAGES**	**19a. NAME OF RESPONSIBLE PERSON**
a. REPORT	**b. ABSTRACT**	**c. THIS PAGE**			J. Sean Humbert
					19b. TELEPHONE NUMBER *(Include area code)*
UU	UU	UU	UU	94	303 492 8250

Standard Form 298 (Rev. 8/98)
Prescribed by ANSI Std. Z39.18

The Mode Sensing Hypothesis

Final Report

AFOSR Grant Number FA9550-14-1-0068

25 November 2020

J. Sean Humbert
Department of Mechanical Engineering
University of Colorado Boulder
sean.humbert@colorado.edu

Holger G. Krapp
Department of Bioengineering
Imperial College, London
h.g.krapp@imperial.ac.uk

Graham K. Taylor
Department of Zoology
Oxford University
graham.taylor@zoo.ox.ac.uk

Table of Contents

1 Overview and Executive Summary

We begin by giving a brief overview of how all of the component parts of this project come together. The Mode Sensing Hypothesis (MSH) posits that insect sensorimotor systems are matched to the natural modes of motion of the insect's flight dynamics, which in turn are determined by the complex interaction of flight morphology, musculoskeletal output, and flight physics. In other words, the mapping from motor input $\boldsymbol{u}(t)$ to sensor output $\boldsymbol{y}(t)$ that is involved in flight control embodies a principle of evolutionary design that is related to the characteristic ways in which the state of the system $\boldsymbol{x}(t)$ varies through time. The simplest possible model of the mapping from $\boldsymbol{u}(t)$ to $\boldsymbol{y}(t)$ linearizes the system about a state of flight equilibrium, and treats the insect as a linear time-invariant system of the form:

$$\dot{\boldsymbol{x}}(t) = \mathbf{A}\boldsymbol{x}(t) + \mathbf{B}\boldsymbol{u}(t) + \mathbf{G}\boldsymbol{d}(t)$$
$$\boldsymbol{y}(t) = \mathbf{C}\boldsymbol{x}(t)$$

where $\boldsymbol{u}(t)$ is a vector of motor inputs, $\boldsymbol{d}(t)$ is a vector of external disturbances, $\boldsymbol{y}(t)$ is a vector of sensor outputs, and $\boldsymbol{x}(t)$ is the state of the system, which for a flying animal must minimally include perturbations to the 6 degrees of freedom (6-DoF) of rigid-body motion from a reference state of equilibrium flight. The $\mathbf{C}$ matrix describes how the sensor output $\boldsymbol{y}(t)$ depends on the system state $\boldsymbol{x}(t)$, and therefore captures how, for example, optical flow sensitive interneurons in the motion vision system are matched to particular directions of self-motion. The $\mathbf{A}$ matrix describes how the system state $\boldsymbol{x}(t)$ evolves through time in the absence of motor input, which contains stability derivatives modelling how the aerodynamic forces and moments depend on the system state, and elements of the insect's inertia tensor. The $\mathbf{B}$ matrix describes how motor input $\boldsymbol{u}(t)$ causes the system state $\boldsymbol{x}(t)$ to change, which depends not only on the aerodynamics of flapping flight, captured by control derivatives modelling how the aerodynamic forces and moments depend on motor input, but also on the specific kinematic couplings with which these motor inputs are associated. The $\mathbf{G}$ matrix describes how disturbances $\boldsymbol{d}(t)$ cause the system state $\boldsymbol{x}(t)$ to change and is derived from the aerodynamic contributions to the $\mathbf{A}$ matrix.

Testing the MSH therefore amounts to testing how the $\mathbf{C}$ matrix describing the physiology of the insect's sensory system is matched to the $\mathbf{A}$, $\mathbf{B}$ and $\mathbf{G}$ matrices describing the insect's flight physics. In our approach, tools from dynamical systems theory and control theory are utilized to characterize the nature of the matching. In particular, the geometry (singular values σ_i and vectors $\mathbf{v}_i$) of the various gramian structures calculated from the resulting $\mathbf{A}$, $\mathbf{B}$, $\mathbf{G}$ and $\mathbf{C}$ matrices provide dynamically significant directions in state space for the animal, such as motions that require the least amount of energy, disturbances that generate the largest perturbations from equilibrium, sensor locations and weightings that exhibit the best noise reduction properties, and couplings of sensor and actuator directions that exhibit the optimal energy throughput for the system. These directions $\mathbf{v}_i$ can be compared directly to the rows of the $\mathbf{C}$ matrix, which correspond to directions in state space encoded by LPTCs, allowing for both quantification of and control-relevant insights into the matching.

This is a challenging task, because whereas the elements of the state vector $\boldsymbol{x}$ can be elucidated from first principles, the elements of the control input vector $\boldsymbol{u}$ and sensor output vector $\mathbf{y}$ can only be established empirically. Building and analysing a model of this form for any one insect is therefore a significant endeavor that spans several academic disciplines, requiring:

(i) neuroanatomical understanding to define $\mathbf{y}$;
(ii) neurophysiological measurements to define $\mathbf{C}$;
(iii) kinematic measurements and modelling to define $\boldsymbol{u}$;
(iv) physical measurements to define the inertia tensor for $\mathbf{A}$ and $\mathbf{B}$;
(v) aerodynamic modelling to define the stability and control derivatives in $\mathbf{A}$, $\mathbf{B}$ and $\mathbf{G}$;
(vi) dynamical systems analysis of $\mathbf{A}$, $\mathbf{B}$, $\mathbf{G}$ and $\mathbf{C}$.

Broadly speaking, Imperial has led on (i-ii) in conjunction with Colorado, Oxford has led on (iii-iv) in conjunction with Leeds, Maryland has led on (v) in conjunction with Colorado and Oxford; and Colorado has led on (vi) in conjunction with Oxford and Imperial. This report describes the fruits of that endeavor, with a primary focus on the blowfly *Calliphora*.

1.1 Status of Modeling and Data Collection

Green – complete; Yellow- partially complete; Red – significant effort remains

***Table 1**: Status of Modeling and Data Collection*

Species	**Kinematics**	**A / G Matrix**	**B Matrix**	**C Matrix**
Calliphora	Data sets have been recorded and have been reduced for the proper control vector	Blade element modelling has been used to identify longitudinal and lateral A matrices; CFD analysis was performed in Year 6	Blade element modelling has been used to identify B matrix for the proper control vector; CFD analysis was performed in Year 6	Significant number of directional templates have been recorded and reduced. New spiking LPTCs analysis was performed in Year 6
Eristalis	Data sets have been recorded and have been reduced for the proper control vector	Blade element modelling has been used to identify longitudinal and lateral A matrices; CFD analysis yet to be completed	Blade element modelling has been used to identify B matrix for the proper control vector; CFD analysis yet to be completed	Accumulated data on spiking LPTCs including both H- and V-cells
Drosophila	Data sets have been recorded and have been reduced for the proper control vector	Blade element modelling has been used to identify longitudinal and lateral A matrix; CFD analysis yet to be completed	Blade element modelling has been used to identify B matrix for the proper control vector; CFD analysis yet to be completed	Potential to collaborate with Reiser et. al. using novel method of identification to obtain a full set

1.2 Status of Publications

The work has produced five peer-reviewed publications to date, with another five papers now in final draft. Seven further papers are at an advanced stage of preparation by the PIs, including the key joint papers with to test the mode sensing hypothesis. A summary is provided below:

Published papers:

(1) Walker, S.M., Taylor, G.K. (2020). A semi-empirical model of the aerodynamics of manoeuvring insect flight. bioRxiv 2020.01.09.900654. [preprint, now in revision at J. R. Soc. Interface] https://doi.org/10.1101/2020.01.09.900654.
(2) Nagesh, I., Walker, S.M., Taylor, G.K. (2019). Motor output and control input in flapping flight: a compact model of the deforming wing kinematics of manoeuvring hoverflies. J. R. Soc. Interface 16, 20190435. https://doi.org/10.1098/rsif.2019.0435.
(3) Huang, J.V., Wei, Y. and Krapp H.G.: Biohybrid Fly-Robot Interface system performs active collision avoidance in corners. *Journal of Bioinspirations and Biomimetics*, **14**, (2019) 065001, https://doi.org/10.1088/1748-3190/ab3b23.
(4) Windsor, S.P. & Taylor, G.K. (2017). Head movements quadruple the range of speeds encoded by the insect motion vision system in hawkmoths. Proc. R. Soc. B 284(1864), 20171622. https://doi.org/10.1098/rspb.2017.1622.
(5) Hardcastle B.J. and Krapp H.G.: Evolution of gaze stablilization. *Current Biology*, **26**(20), R1010-1021 (2016). https://www.cell.com/current-biology/pdf/S0960-9822(16)31004-1.pdf

Papers at final draft:

(1) Page, J., Walker, S.M. & Taylor, G.K. Four-dimensional micro-tomographic imaging reveals the control muscle mechanisms of blowflies. Prepared for submission to eLife.
(2) Nagesh, I., Dawson, I. Walker, S.M., & Taylor, G.K. A comparative analysis of the wing kinematic couplings involved in the control of flight manoeuvres across four species of dipteran fly. Prepared for submission to J. R. Soc. Interface.
(3) Walker, S.M. & Taylor, G.K. Wingbeat-averaged forces of free-flying hoverflies are captured by a blade element model with only two fitted parameters. Prepared for submission to J. R. Soc. Interface.
(4) Nagesh, I., Walker, S.M., Taylor, G.K. Modelling the deforming wing kinematics and control mechanisms of maneuvering Eristalis hoverflies in compact form through functional principal components analysis. Prepared for submission to J. R. Soc. Interface.
(5) Page, J., Walker, S.M. & Taylor, G.K. Four-dimensional micro-tomographic imaging reveals the control muscle mechanisms of blowflies. Prepared for submission to eLife.

Papers now in preparation:

(1) Humbert, J.S., Krapp, H.G., Taylor, G. K. et al.: The Mode Sensing Hypothesis: Relationship between sensory measuring axes and motor coordinate systems in a flying insect. (in preparation).
(2) Huang, J.V., Yang, Y., Zabolotniy, M., Krapp, H.G.: A goniometric recording platform to study the response properties of wide-field motion sensitive interneurons. (in preparation).

(3) Yang, Y., Huang, J.V., Zabolotniy, M., Krapp, H.G.: Comparative study of wide-field visual interneurons supporting binocular optic flow processing across dipteran fly species. (in preparation).
(4) Nagesh, I., Walker S.M. & Taylor, G.K. Lateral-longitudinal flight dynamics and control of Eristalis hoverflies with empirically-identified control inputs and semi-empirical flight mechanics modelling. In preparation for J. R. Soc. Interface.
(5) Nagesh, I., Müller, T.C. & Taylor, G.K. Forward models are needed to explain the optomotor yaw response of free-flying hawkmoths in a model parameterized using tethered-flight measurements. In preparation for Nature Comms.
(6) Nagesh, I., Walker S.M. & Taylor, G.K. Flight dynamics and controllability of Eristalis hoverflies with empirically-identified control inputs and semi-empirical flight mechanics modelling. In preparation for PLoS Biol.
(7) Nagesh, I., Walker S.M. & Taylor, G.K. A comparative analysis of the longitudinal flight dynamics and control of three species of dipteran flies. In preparation for J. R. Soc. Interface

Additional planned high-impact publications:

(1) Additional standalone or comparison journal publication on The Mode Sensing Hypothesis using *Eristalis* data – (Taylor, Humbert, Krapp)
(2) Journal publication on the implementation of Mode Sensing Hypothesis principles for control of multirotor systems – (Humbert, Krapp, Taylor)

Additional peer-reviewed publications that can partially be attributed to the grant:

(1) Longden K.D. Wicklein M., Hardcastle B.J., Huston S.J. and Krapp H.G.: Spike interval coding of translatory optic flow and depth from motion in the fly visual system. *Current Biology,* 27(21)*, 3225-3236.e3* (2017).
(2) Longden K.D., Muzzo T., Cook D., Schultz S.R., and Krapp H.G.: The Nutritional State Modulates the Neural Processing of Visual Motion. *Current Biology*, 24(8), 890-895 (2014).
(3) Huang J.V., Wei Y., and Krapp H.G.: Active collision free closed-loop control of a biohybrid fly-robot interface. In: Biomimetic and Biohybrid Systems, Living Machines, Springer (accepted).
(4) Huang J.V. Krapp H.G.: Neuronal distance estimation by a fly-robotic interface. In: Biomimetic and Biohybrid Systems, Living Machines, Springer, pp. 204-215 (2017).
(5) Huang J.V., Wang Y., and Krapp H.G.: Wall-following in a semi-closed-loop fly-robotic interface. In: Biomimetic and Biohybrid Systems, Living Machines 2016, Lecture Notes in Computer Science, vol 9793. Springer, pp. 85-96 (2016).
(6) Huang J.V. and Krapp H.G.: Closed-loop control in an autonomous bio-hybrid robot system based on binocular neuronal input. In: Biomimetic and Biohybrid Systems, Living Machines 2015, Springer, ISBN: 978-3-319-22978-2 (Print) 978-3-319-22979-9 (Online), pp. 164-174 (2015).
(7) Krapp H.G.: Flies, optic flow, and multisensory stabilization reflexes. In: Flow Sensing in Air and Water. Bleckmann H. et al. (eds.), Springer, Berlin, Heidelberg, pp. 215-243, (2014) DOI: 10.1007/978-3-642-41446-6_9

1.3 Summary of Accomplishments in Year 6

Oxford: Work during the final year of this research effort has been focused on: (i) publishing our new PCA method for defining the control inputs $\boldsymbol{u}$ of an insect (Nagesh *et al*., 2019); (ii) applying this PCA method comparatively across *Eristalis*, *Calliphora*, and *Drosophila*, to identify the range of the control input subspace of each dipteran species using new kinematic data (Nagesh et al., in prep, a); (iii) publishing the semi-empirical blade element model that we have developed for modelling the aerodynamics of *Eristalis* flight maneuvers (Walker & Taylor, 2020); (iv) using the blade element model and PCA description of $\boldsymbol{u}$ to derive a lateral-longitudinal state space model of *Eristalis* flight dynamics and control (Nagesh et al., in prep, b); and (v) using the CFD model for *Calliphora* developed by Colorado/Maryland to derive a state space model of *Calliphora* flight dynamics and control using the PCA description of $\boldsymbol{u}$. Work toward these objectives was undertaken by postdoc Dr Indira Nagesh and PI Prof. Graham Taylor with co-PI Dr Simon Walker (Leeds University).

Imperial College London: During the final year of the project we have been (i) expanding the data base on receptive fields (directional templates) of heterolateral LPTCs in various dipteran fly species, (ii) computing the preferred self-motion parameters of heterolateral LPTCs axes using the KvD algorithm, (iii) performing (circular/spherical) statistical analyses to assess potential sexual dimorphisms and inter-specific differences of preferred motion parameters and (iv) improving the Goniometric Recording Platform (GRP, cf. report year 4) for applications in the field. The main lab-based activities, data analysis and technical development of the GRP have been carried out by Dr Jiaqi Huang (postdoc), supervised by the PI Prof. Krapp, who also coordinated and contributed to efforts (ii) and (iii).

Colorado/Maryland: The team's efforts this final year have been focused on (i) computational fluid dynamics of *Calliphora* to estimate the state space open loop **A** matrix and the corresponding **B** matrix according to the PCA description of the control inputs $\boldsymbol{u}$, and (ii) analysis of LPTC directional templates in the context of the newly-derived, CFD-based state space model's dynamically significant directions. Objective (i) has being undertaken by postdoc Yong Su Jung, currently at the University of Maryland, supervised jointly by PI Prof. Sean Humbert (CU) and Prof. James Baeder. Objective (ii) is being performed by PI Prof. Sean Humbert.

1.4 Status of Funding and Expenditures

The original proposal spanned four years and was revised to a five-year period of performance where 90% of the first-year funds went to Imperial College to kickstart the electrophysiology effort. The official start date was 15 March 2014, and a total of $2,166,706 (92%) of the proposed $2,337,222 has been received by Maryland ($349,998 on 10 March 2014, $165,561 on 24 Aug 2015, $347,928 on 1 Oct 2015, $175,376 on 1 Oct 2016, $365,638 on 1 Oct 2017, $572,205 on 1 Oct 2018, and $190,320 on 25 July 2018). A 1-year extension was granted by AFOSR on 14 March 2019. The PIs understand and appreciate the fact that the funding is being provided by AFRL and is on a year-to-year basis and are grateful for the generous support. As of the end of the contract, UMD had expensed $345,852, Colorado had expensed $485,401.83, Imperial College had expensed $814,363.07 and Oxford had expensed $671,137.79 (Figure 1, Table 2).

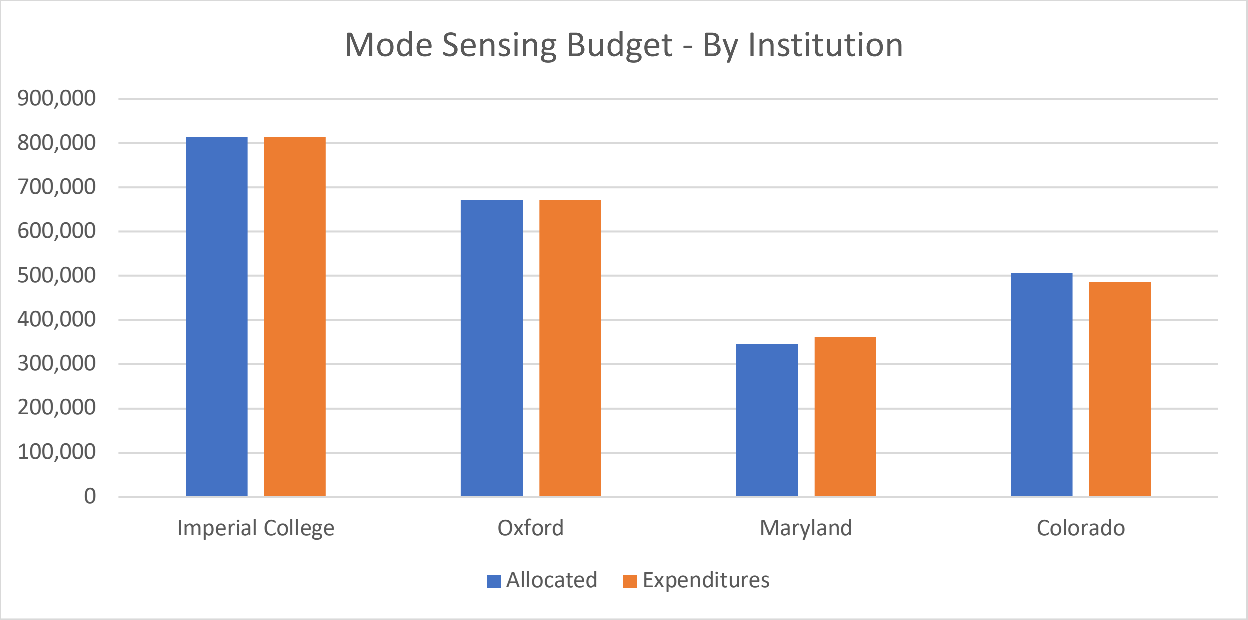

***Figure 1**: Budget and Expenditures*

***Table 2**: Budget and Expenditures*

	Allocated	Final Expenditures
Imperial College	814,355	814,363
Oxford	671,030	671,138
Maryland	345,852	361,450
Colorado	505,985	485,401
Totals	2,337,222	2,332,353

2 **Comparative Kinematics and Dynamics of Dipteran Flight** (Graham K. Taylor, Indira Nagesh, Inés Dawson, Oxford University; Simon M. Walker, Leeds University)

2.1 A comparative analysis of the dominant wing kinematic couplings involved in the flight control of four species of manoeuvring dipteran fly

Even quite closely related species of insect can vary in the detailed actuation of their flight motor. Coupled with interspecific variation in the structure of the wings, this means that each species of insect has its own characteristic wing kinematics and its own characteristic way of varying these in flapping flight control. Identifying the species-specific kinematic couplings that are involved in insect flight control is therefore essential to defining the input vector $\mathbf{u}$ that forms the starting point of any analysis of flight control. This has not previously been attempted for any species of insect, and the analytical framework that we have developed to do this (Nagesh *et al*., 2019 and below) is as novel as the empirical data that we have collected to enable this analysis (Dawson, unpublished thesis). The comparative analysis of dipteran wing kinematics that we describe below is the most detailed and extensive analysis of insect wing kinematics ever undertaken, based on an analysis of over 32,000 wingbeat pairs. It provides a natural vector basis in which to define the input vector $\boldsymbol{u}$ and against which to specify the control matrix $\mathbf{B}$ for four species of dipteran fly, including *Calliphora*.

2.1.1 *Materials and methods*

The kinematic analysis on which this paper is based utilises a free-flight dataset collected from two species of *Eristalis* hoverflies that was first described by Walker *et al*. (2012), and which was subsequently used by Nagesh *et al*. (2019) to develop the analytical techniques that we apply here comparatively for the first time. In the present analysis, this published dataset is split by species, so that we analyse the $N = 20{,}987$ wingbeat pairs collected from 676 flights by $n = 30$ individual *Eristalis tenax* separately from the $N = 5{,}554$ wingbeat pairs collected from 203 flights by $n = 6$ individual *E. pertinax*. These existing datasets are supplemented by two entirely new free-flight datasets comprising $N = 2{,}708$ wingbeat pairs collected from 205 flights by $n = 28$ individual blowflies *Calliphora vicina*, and $N = 2{,}959$ wingbeats from 274 flights representing an unknown number of individual fruit flies *Drosophila melanogaster*. The resulting analysis, based on a total of $N = 32{,}208$ wingbeat pairs collected from 4 model species of dipteran flies during manoeuvres representing 1,358 separate flights is by far the most extensive analysis of insect flight control to date. We begin by describing the experimental methods and reconstruction techniques that we used to collect the data, before describing the functional principal components analysis (FPCA).

2.1.1.1 Experimental methods

Wild *Eristalis tenax* and *E. pertinax* were caught as adults in Oxford, and were fed on sugar solution before being flown. Larval *Calliphora vicina* were obtained from a local pet store, and were reared on red meat at 20˚C until pupation; the adult flies were fed on a combination of milk powder formula and mashed banana, and were flown from 2-3 days post-eclosion. Cultured *Drosophila melanogaster* (Oregon R) were reared on a standard growth medium at 20˚C on a 12h daylight cycle, and were not flown from at least 5 days post-eclosion. Whereas *Eristalis* and *Calliphora* were released individually into the flight chamber, *Drosophila* were released in groups of 5-20 individuals to maximise the efficiency of data collection. The methods used to collect data from *Calliphora* were similar to those described previously for *Eristalis* Walker *et al.* (2012). Individuals were allowed to fly freely within a 1 m diameter opaque acrylic sphere with diffuse overhead lighting. An ultraviolet light placed at the top of the arena served as an attractive stimulus for *Calliphora*, whereas a white LED light source was used to encourage sustained hovering by *Eristalis*. The interior of the arena was decorated with pieces of card to provide a visual stimulus for *Calliphora*, which proved important in encouraging sustained flight. Groups of *Drosophila* were released within a clear polyester cylinder of 0.3 m length and 0.2 m diameter placed at the centre of the arena, and were stimulated to fly by vibrating the cylinder; cotton balls dipped in ethanol and vinegar were used as local attractants. High-speed video sequences were captured using four synchronized Photron SA3 cameras (Photron Ltd, West Wycombe, UK) with 180 mm macro lenses (Sigma Imaging Ltd, Welwyn Garden City, UK) viewing the insect through clear portholes in the upper hemisphere, recording at 3.8 kHz and 768×640 pixels for *Eristalis* and *Calliphora*, and at 4.8 kHz and 640×576 pixels for *Drosophila*. A pair of 200 W pulsed infrared lasers (HSI-5000, Oxford Lasers Ltd, Oxford, UK; pulse duration: 20 μs) slaved to the cameras provided intense back-illumination via four Fresnel lenses at an 805 nm wavelength invisible to the insects. Recordings were triggered as the insect passed through the centre of the sphere, usually capturing hovering or forward flight punctuated by the fast saccadic manoeuvres that are typical of dipteran flies.

2.1.1.2 Kinematic reconstruction

All of the subsequent analysis was performed in MATLAB (The Mathworks, Inc.). The cameras were calibrated using a nonlinear least squares bundle adjustment routine, based on images of a calibration grid presented in a wide range of positions and orientations Walker *et al*. (2009). We used background subtraction and automatic thresholding to segment the pixels in frame, and used a shape-carving method to identify the set of voxels containing the wings and body (Walker *et al*., 2012). We reprojected the wing voxels as a mask for tracing the outline of the wing in each frame, and used the shape-carving algorithm on this linear feature to reconstruct the leading and trailing edges in three dimensions (3D). We used the major axis of the body voxels to define the insect's *x*-axis, signed positive anteriorly. We measured the insect's heading speed as the component of its body velocity resolved in the direction of the horizontal projection of its *x*-axis, and defined the insect's horizontal advance ratio J as the ratio of its heading speed to the mean speed of its wing tip oscillation. We took the line connecting the wing roots to define the insect's transverse *y*-axis, and used these axis definitions to construct a right-handed body axis system in which to measure the kinematics of the right wing, and a left-handed body axis system in which to measure the kinematics of the left wing.

The wing kinematics were measured by defining an extrinsic *y-x-z* rotation sequence bringing the *x*-axis of a set of rotating axes initially aligned with the body axes into alignment with the wing chord connecting the trailing edge to the leading edge at some given spanwise position (r). The local pitch angle of the wing (ω), is defined as the first angle in this rotation sequence, and was measured at 6 evenly-spaced spanwise stations on the interval $r \in [0.3,0.8]$, where r is expressed as a proportion of wing length. We summarised the instantaneous spanwise variation in ω by fitting the regression model $\omega[r] = \omega_0 + \omega_r r + \epsilon[r]$, where $\epsilon[r]$ is a gaussian error term. We call ω_0 the twist offset, and ω_r the twist gradient. The deviation angle θ and stroke angle ϕ represent the second and third angles in the extrinsic *y-x-z* rotation sequence, and effectively describe the elevation and azimuth of the wingtip in a set of body axes originating at the wing root. It follows that the insect's wing kinematics are measured by estimating $\phi[t]$, $\theta[t]$, $\omega_0[t]$, $\omega_r[t]$ for the right and left wings separately at every sample time t. Our use of right- versus left-handed axis conventions for the right and left wings means that the time history of these variables looks similar, as opposed to mirrored, for the two wings.

For each flight sequence, we fitted quintic smoothing splines modelling $\phi[t]$, $\theta[t]$, $\omega_0[t]$, and $\omega_r[t]$ for each wing as analytical functions of continuous time t. The spline tolerance that we used for each kinematic variable was chosen to preserve information up to the 3rd harmonic of wingbeat frequency for ϕ and θ, and up to the 5th harmonic for ω_0 and ω_r. We then used a piecewise linear transform to map continuous time t onto wingbeat phase $\varphi(t)$, by taking the turning point of the summed angular velocity of both wingtips in the stroke plane to define $\varphi = 0$ as the start of the downstroke. Finally, we evaluated the splines at 101 evenly-spaced phases of each wingbeat on the interval $\varphi \in [0,2\pi]$, so that all wingbeats were directly comparable despite the variation in wingbeat period and differences in sampling rate between species. Fitting each wingbeat separately, we then used multiple regression with time-linear and time-periodic predictor variables to model the four primary kinematic variables $\phi[\varphi]$, $\theta[\varphi]$, $\omega_0[\varphi]$, and $\omega_r[\varphi]$ as de-trended Fourier series of the form:

$$f[\varphi] = K_{\mathrm{L}}(\varphi - \pi) + K_0 + \sum_{k=1}^{P} \left(K_{2k-1}\cos(k\varphi) + K_{2k}\sin(k\varphi)\right) + \epsilon[\varphi]$$

where $\epsilon[\varphi]$ is a gaussian error term, and where K_L and $K_0 \dots K_{2P}$ are fitted coefficients. The time-linear coefficient K_L accounts for the fact that any actual wingbeat cycle is unlikely to begin and end in exactly the same kinematic state, and multiplies $(\varphi - \pi)$ rather than φ so that this term has zero mean over the wingbeat cycle. The Fourier coefficients $K_0 \dots K_{2P}$ are fitted with $P = 3$ for ϕ and θ, and with $P = 5$ for ω_0 and ω_r, to capture all of the harmonic content preserved by the quintic smoothing splines.

Collecting the Fourier coefficients for a single wingbeat together as:

$$\mathbf{K}^{\phi} = \left[K_0^{\phi} \dots K_{2P}^{\phi}\right]$$

for the stroke angle ϕ, and similarly for the other primary kinematic variables, we may summarise the time-periodic variation for all \$N\$ wingbeat pairs in the matrix:

$$\mathbf{X}_{\mathrm{P}} = \begin{bmatrix} \mathbf{K}^{\phi}[1] & \mathbf{K}^{\theta}[1] & \mathbf{K}^{\omega_r}[1] & \mathbf{K}^{\omega_0}[1] \\ \vdots & \vdots & \vdots & \vdots \\ \mathbf{K}^{\phi}[2N] & \mathbf{K}^{\theta}[2N] & \mathbf{K}^{\omega_r}[2N] & \mathbf{K}^{\omega_0}[2N] \end{bmatrix}$$

For completeness, the time-linear coefficients for each wingbeat are stored in the matrix:

$$\mathbf{X}_{\mathrm{L}} = \begin{bmatrix} \mathrm{K}_L^{\phi}[1] & \mathrm{K}_L^{\theta}[1] & \mathrm{K}_L^{\omega_r}[1] & \mathrm{K}_L^{\omega_0}[1] \\ \vdots & \vdots & \vdots & \vdots \\ \mathrm{K}_L^{\phi}[2N] & \mathrm{K}_L^{\theta}[2N] & \mathrm{K}_L^{\omega_r}[2N] & \mathrm{K}_L^{\omega_0}[2N] \end{bmatrix}$$

although we do not use this further in the analysis here. These two matrices $\mathbf{X}_{\mathrm{P}} \in \mathbb{R}^{2N\times 36}$ and $\mathbf{X}_{\mathrm{L}} \in \mathbb{R}^{2N\times 4}$ contain all of the information needed to reconstruct the kinematics of every recorded wingbeat in dimensionless form. They are treated separately because we conceptualise insect flight as a form of limit cycle control in which the wing transitions continuously from one steady-state oscillation to the next. Specifically, whereas $\mathbf{X}_{\mathrm{P}}$ captures the variation in the steady-state oscillations of the wing, $\mathbf{X}_{\mathrm{L}}$ describes how the wing transitions between successive steady-state oscillations subject to a continuity constraint. Hence, once a sequence of steady-state oscillations is established, the associated sequence of linear transitions is determined by the continuity constraint, so does not add any new degrees of freedom. For this reason, we consider only the matrix of time-periodic coefficients $\mathbf{X}_{\mathrm{P}}$ in the remainder of the analysis.

2.1.1.3 Functional Principal Component Analysis (FPCA)

We use functional principal components analysis (FPCA) to decompose the Fourier series representations of the wingbeat oscillations for each species into a new set of time-periodic basis functions characterising the kinematic couplings involved in their flight control. This is implemented by subtracting the column means from the matrix of Fourier coefficients $\mathbf{X}_{\mathrm{P}}$ to yield the centered matrix $\mathbf{X} = \mathbf{X}_{\mathrm{P}} - \overline{\mathbf{X}}_{\mathrm{P}}$ and computing its singular value decomposition:

$$\mathbf{X} = \mathbf{U}\mathbf{\Sigma}\mathbf{V}^{\mathrm{T}}$$

Here, $\mathbf{\Sigma} \in \mathbb{R}^{36\times 36}$ is a diagonal matrix containing the singular values of $\mathbf{X} \in \mathbb{R}^{2N\times 36}$, which are the positive square roots of the eigenvalues of $\mathbf{X}^{\boldsymbol{T}}\mathbf{X}$ arranged in descending order. The columns of $\mathbf{V} \in \mathbb{R}^{36\times 36}$ contain the right-singular vectors of $\mathbf{X}$, which are the corresponding eigenvectors of $\mathbf{X}^{\boldsymbol{T}}\mathbf{X}$, normalized such that $\mathbf{V}^{\boldsymbol{T}}\mathbf{V} = \mathbf{I}$. Because $\mathbf{X}^{\boldsymbol{T}}\mathbf{X}$ is a scalar multiple of the covariance matrix of $\mathbf{X}$, the orthonormal basis $\mathbf{V}$ that its eigenvectors define is aligned with the principal directions of the kinematic variation between wingbeats. For this reason, $\mathbf{V}$ is called the principal component (PC) matrix, the entries of which are Fourier coefficients, such that each of its columns defines a distinct time-periodic kinematic coupling referred to hereafter as PC1, PC2, etc. With these definitions, the rows $\mathbf{W} = \mathbf{U}\mathbf{\Sigma}$ contain scores measuring the involvement of each PC on a given wingbeat, with $\mathbf{W} \in \mathbb{R}^{2N\times 36}$. In summary, the FPCA decomposes the time-periodic kinematics of all $2N$ wingbeats for each species as $\mathbf{X}_{\mathrm{P}} = \overline{\mathbf{X}}_{\mathrm{P}} + \mathbf{W}\mathbf{V}^{\mathrm{T}}$, which describes every wingbeat as a deviation from the mean wingbeat kinematics $\overline{\mathbf{X}}_{\mathrm{P}}$, in the directions specified by the PC coefficients in $\mathbf{V}$, to the extent described by the PC scores in $\mathbf{W} = \mathbf{U}\mathbf{\Sigma}$, in which $\mathbf{\Sigma}$ measures the overall importance of each PC. The data and code required to perform this decomposition are provided in MATLAB format as Supplementary Data 1, and the resulting matrices are provided as text files in Supplementary Data 2.

A key motivation for introducing the FPCA decomposition is to facilitate quantitative analysis of the variation in the time-periodic wingbeat kinematics across species. We measure the similarity in the mean wingbeat kinematics of a given pair of species using the normalized inner product $\bar{S}$ of the column means of $\mathbf{X}_\mathrm{P}$ for each species. This metric is defined as $\bar{S} = \hat{\mathbf{x}}_1 \hat{\mathbf{x}}_2^T$, where $\hat{\mathbf{x}}_1$ and $\hat{\mathbf{x}}_2$ are unit vectors in the directions specified by the repeated rows of $\bar{\mathbf{X}}_\mathrm{P}$ for the two species in the dyad. This overall similarity metric $\bar{S}$ quantifies the typical kinematic similarity within a given species pair, with a maximum value of 1. Moreover, having used the FPCA to define a meaningful basis $\mathbf{V}$ in which to describe the coupled variation in the time-periodic wing kinematics of each species, it becomes possible to quantify any similarity in how they vary their wing kinematics. Using $\mathbf{V}_1$ and $\mathbf{V}_2$ to denote the PC matrices for the two species in a dyad, any diagonal structure in their matrix of inner products $\mathbf{R} = \mathbf{V}_1^\mathrm{T}\mathbf{V}_2$ indicates similarity in the specific time-periodic kinematic couplings used in manoeuvring flight. This similarity can be quantified by the metric $\tilde{S} = \frac{1}{36}\sum_{i,j=1}^{36}\left|R_{ij}\right|$, where R_{ij} is the $(i,j)^{th}$ entry of $\mathbf{R}$, and where only its absolute value is considered because the sense of the eigenvectors in $\mathbf{V}_1$ and $\mathbf{V}_2$ is arbitrary. This mean similarity metric $\tilde{S}$ takes values on the interval from 0 to 1, and measures the average similarity of the i^{th} PC of one species to the j^{th} PC of another for all $i = j$. It therefore ignores any similarity that may exist between the i^{th} PC of one species and the j^{th} PC of the other for $i \neq j$, which is problematic if different PCs explain similar amounts of variation so that their ordering is volatile.

To address this limitation, we reorder the PCs for the first species of each dyad using the Munkres algorithm, such that when the reordered PC coefficient matrix $\mathbf{V}_{1*}$ is used to define the permuted matrix of inner products $\mathbf{R}^* = \mathbf{V}_{1*}^\mathrm{T}\mathbf{V}_2$, the similarity metric $\tilde{S}^* = \frac{1}{36}\sum_{i,j=1}^{36}\left|R_{ij}^*\right|$ is maximised. This maximal similarity metric $\tilde{S}^*$ measures the mean similarity of the best-matching pairs of PCs between species, weighting all pairs equally regardless of their relative importance. It therefore measures the overall similarity of the orthonormal basis for each species, rather than measuring the variation that is most important to the insects' flight control. We address this by calculating the weighted mean similarity metric $\tilde{S}_w^*$ for the best-matching pairs of PCs using the products of the singular values of the PCs as weights:

$$\tilde{S}_w^* = \frac{\sum_{i,j=1}^{36} \sigma_{ij}^2 \left|R_{ij}^*\right|}{\sum_{i,j=1}^{36} \sigma_{ij}^2}$$

where σ_{ij}^2 denotes the $(i,j)^{th}$ entry of the matrix $\mathbf{\Sigma}_{1*}^\mathrm{T}\mathbf{\Sigma}_2$, in which $\mathbf{\Sigma}_{1*}$ is the permuted matrix of singular values for the first species and $\mathbf{\Sigma}_2$ is the matrix of singular values for the second. This weighted mean similarity metric $\tilde{S}_w^*$ effectively measures the similarity in the PCs that are most strongly involved in the insects' flight control, and again takes values on the interval from 0 to 1.

2.1.2 *Results*

2.1.2.1 Forward flight condition correlates with body and stroke plane tilt

In all three genera, the horizontal advance ratio J (see Methods) was positively correlated with stroke plane tilt (Pearson's correlation coefficient: *Drosophila*: $r = 0.58$; *Calliphora*: $r = 0.45$; *Eristalis*: $r = 0.39$), which was in turn tightly coupled to body pitch angle (Pearson's correlation coefficient: *Drosophila*: $r = 0.78$; *Calliphora*: $r = 0.80$; *Eristalis*: $r = 0.85$). These correlations are consistent with the hypothesis that flies adjust their horizontal flight speed by tilting their body, and hence their stroke plane, so as to redirect the resultant aerodynamic force (Figure 2). This in itself says nothing about how body pitch is controlled, but it is clear by inspection of the wing tip kinematics (Figure 2) that tilting of the body and stroke plane with respect to the vertical is accompanied by detailed changes in wingtip trajectory with respect to the body axes. In principle, these changes in wingtip trajectory might be produced through parametric control of the wing's root-flapping motion, or aerodynamic forcing as a result of changes in wing twist.

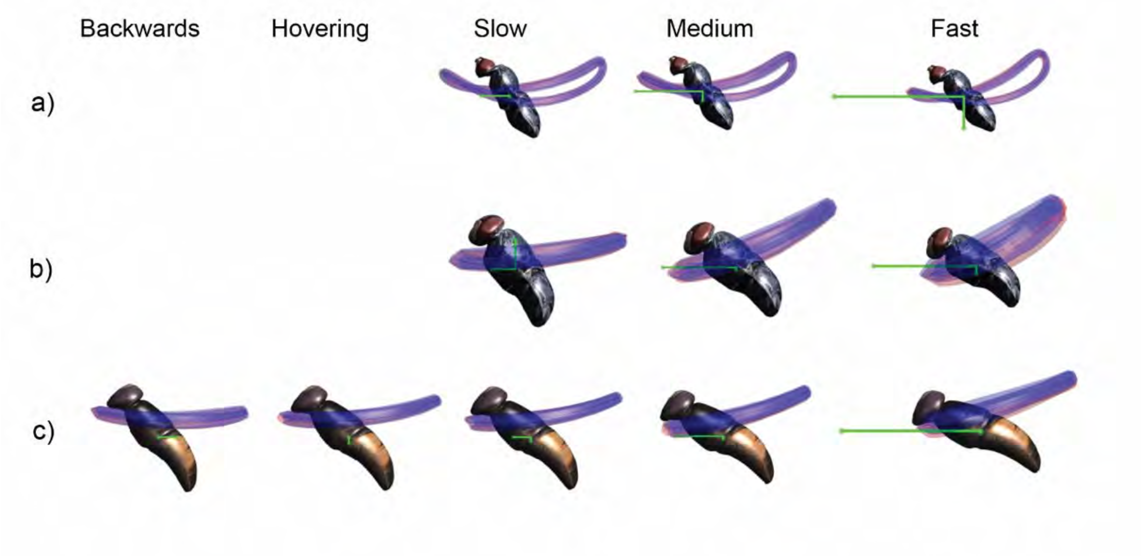

Figure 2. *Systematic variation in mean wingtip trajectory and body pitch for three genera of dipteran fly: (A) Drosophila; (B) Calliphora; (C) Eristalis. Kinematic data are binned by horizontal advance ratio J as follows: backward flight, $J < -0.01$; hovering flight, $-0.01 \leq J \leq 0.01$; slow forward flight, $0.01 < J \leq 0.05$; moderate forward flight, $0.05 < J \leq 0.13$; fast forward flight, $0.13 < J$. There were too few wingbeats in the backward and hovering flight categories for Drosophila and Calliphora to provide a representative sample; data from E. tenax and E. pertinax are pooled accordingly. Green arrows indicate the horizontal and vertical components of mean body velocity, to scale, in each flight condition. Note the increasing nose-down body pitch and stroke plane tilt with increasing advance ratio J.*

2.1.2.2 Forced limit-cycle oscillations in the mean wingbeat kinematics

All four species show a high degree of similarity in their mean wingbeat kinematics ($\bar{S} > 0.90$ for all species dyads), and the mean wingbeat kinematics of the two Eristalis species are practically self-similar with $\bar{S} > 0.99$ (Table 2). Even so, the high overall similarity of the four species belies some important dynamical differences between them, which we now explore. In both species of *Eristalis* (Figure 2), the wingtip sweeps a nearly planar trajectory, tracing almost a great circle path on the upstroke and downstroke, in something approaching a simple harmonic motion (Walker *et al.*, 2010). Focussing on the better-sampled of the two species, the mean wingtip trajectory of *E. tenax* (Figure 3) describes a simple closed curve on the phase plane defined by the spherical coordinates $\{\phi, \theta\}$. In principle, it can therefore be treated as a limit cycle oscillation of a plane autonomous system, $\dot{\phi} = \Phi(\phi, \theta)$ and $\dot{\theta} = \Theta(\phi, \theta)$, where Φ and Θ are functions that do not depend explicitly on time. The mean wingtip trajectory of Calliphora also describes a simple closed curve, so can be treated similarly, but traces a quite different path on the upstroke and downstroke owing to the presence of significant higher-harmonic content (Figure 3). This harmonic content is even more pronounced in Drosophila, in which the mean wingtip trajectory intersects on the upstroke and downstroke (Figure 3), thereby requiring treatment as a non-autonomous system, $\dot{\phi} = \Phi(\phi, \theta, t)$ and $\dot{\theta} = \Theta(\phi, \theta, t)$, where the functions Φ and Θ now depend explicitly on time. The root-flapping motion of the wings therefore shows unambiguous evidence of forced harmonic content in *Drosophila*, and possible evidence of this in *Calliphora*. Summarising across species, these findings are consistent with the hypothesis that the limit cycle oscillation of the wing's root-flapping motion is subject to external aerodynamic forcing, with the effects of this forcing being stronger in *Drosophila* than in *Calliphora* than in *Eristalis*.

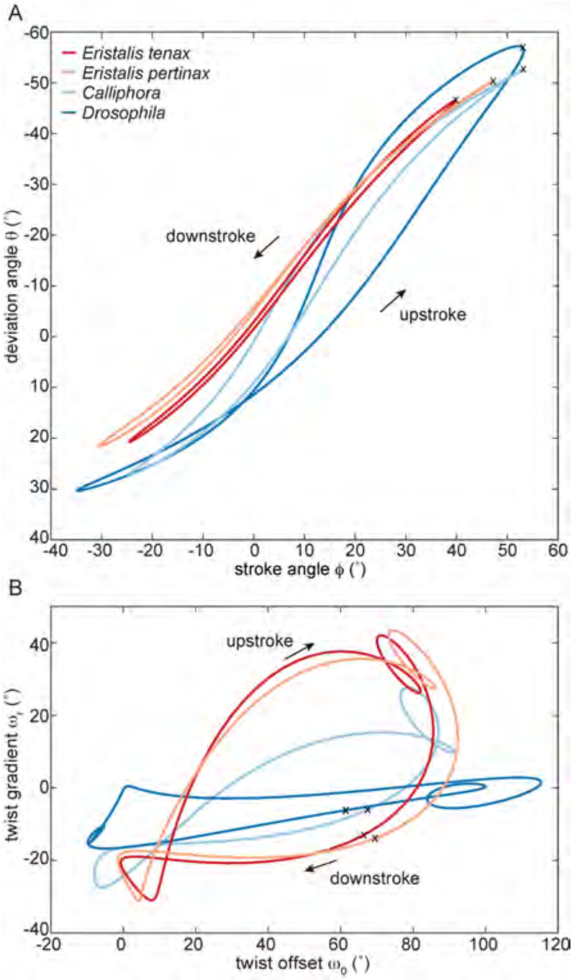

Figure 3. *Phase-plane plots of the mean time-periodic wingbeat kinematics for four species of dipteran fly. (A) Wing tip kinematics, plotting deviation angle $\theta(t)$ against stroke angle $\phi(t)$. (B) Wing twist kinematics, plotting twist gradient $\omega_r(t)$ against twist offset $\omega_0(t)$. Black crosses denote the beginning of the downstroke (i.e. wingbeat phase $\varphi = 0$); black errors indicate the direction of progression around the closed curves. Loops in the trajectories indicate the presence of forced harmonic content.*

It is reasonable to suppose that any such aerodynamic forcing will be coupled to the wing twist kinematics, which are described by the twist offset $\omega_0(t)$ measuring the pitch angle of the wing at its root, and the twist gradient $\omega_r(t)$ measuring the linear change in pitch angle from root to tip.

Because the wing is only actuated at its root, the twist offset $\omega_0(t)$ is effectively a direct forcing term, whereas the twist gradient $\omega_r(t)$ effectively characterises its first torsional vibration mode. These vibrations will be forced by the musculoskeletal torque that produces wing pronation and supination, and may also be subject to aeroelastic excitation. Accordingly, the mean twist kinematics follow a non-simple closed curve on the $\{\omega_0, \omega_r\}$ phase plane in all four species (Figure 3), with multiple intersecting loops reflecting the presence of significant forced harmonic content. However, in *Drosophila*, the amplitude of the mean twist gradient oscillation is six times less than that of the mean twist offset oscillation (Figure 3). In contrast, the amplitude of the mean twist gradient oscillation is approximately half that of the mean twist offset oscillation in *Calliphora*, and the two are of similar amplitude in *Eristalis* (Figure 3). Hence, the wing's first mode of torsional vibration is much more pronounced in *Eristalis* than in *Calliphora* than in *Drosophila*, so in this sense, the complexity of the twist kinematics is inversely related to the complexity of the tip kinematics (Figure 3).

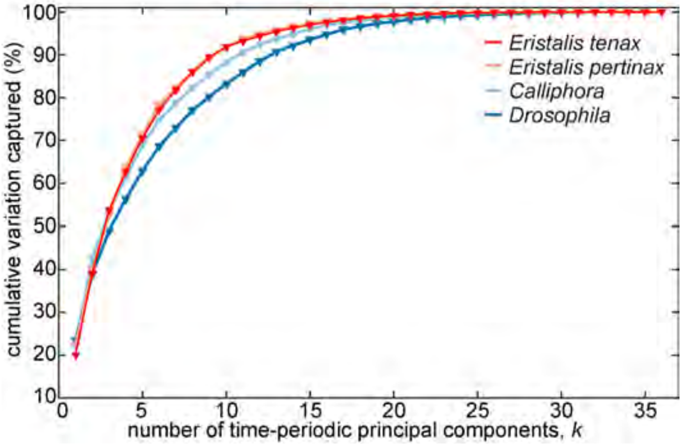

Figure 4. *Cumulative percentage of the between-wingbeat variation in the time-periodic wingbeat kinematics that is captured by the first* k *principal components for four model species of dipteran fly.*

2.1.2.3 Kinematic couplings in the variation between wingbeats

The time-periodic couplings that characterise the mean wingbeat kinematics for each species (Figure 3) are subject to variation between wingbeats – this being the primary mechanism of flight control in insects. The FPCA serves to identify the kinematic couplings that underpin this variation between wingbeats, thereby providing a natural basis for analysing the available control inputs. Specifically, the leading time-periodic PCs characterise the dominant kinematic couplings that are used in the flight control of each species. In fact, the kinematic subspace defined by PCs 1-3 is already sufficient to capture approximately half of the kinematic variation in the time-periodic wingbeat oscillations of each species (Figure 4). Moreover, it is apparent from their respective contributions to the time-periodic PCs (Figure 5) that the time-history of the wing twist variables $\omega_0(t)$ and $\omega_r(t)$ is subject to much greater variation between wingbeats than is the time history of the wing tip variables $\phi(t)$ and $\theta(t)$. These conclusions hold across all of the species that we have studied.

Each PC describes a specific mode of oscillation with respect to the orbital trajectory characterising the mean wingbeat kinematics. It is clear by inspection that the main contribution of PCs 1-3 is a tilting of the stroke plane with respect to the body axes–obvious exceptions being PC2 in *Calliphora*, which describes a wholesale fore-aft displacement of the stroke plane; and PC1 in *Drosophila*, which involves almost no change in wing tip trajectory (Figure 6). This tilting of the stroke plane is typically accomplished by varying the fore-aft sweep of the wing, as can be seen directly from the $\{\phi, \theta\}$ phase-plane plots (Figure 6). Changes in the dorso-ventral motion of the wing play a lesser part in effecting changes in stroke plane angle, which is reflected in the fact that the deviation angle θ contributes less strongly to the leading PCs than does the stroke angle ϕ. As a result, the wing tip path becomes longer as it becomes shallower, such that tilting of the stroke plane is closely coupled to changes in stroke amplitude (Figure 5).

These coupled changes in the tip kinematics are in turn coupled to changes in the twist kinematics. The complexity of the $\{\omega_0, \omega_r\}$ phase-plane plots makes these changes in wing twist much harder to interpret (Figure 7). Nevertheless, it is clear that the twist gradient $\omega_r(t)$ is usually perturbed in opposition to the twist offset $\omega_0(t)$ (Figure 7), which in effect means that any increased pitching motion of the wing at its root is attenuated moving further out along the span. This conclusion holds for all four species, and for all of PCs 1--3, at nearly all phases of the wingbeat, which makes sense as a damped elastic response to forcing. Even so, these coupled changes in twist gradient and offset are often concentrated at specific phases of the stroke (Figure 7). For example, PC1 in *E. tenax* and PC2 in *E. pertinax*, *Calliphora*, and *Drosophila* all involve marked changes in twist gradient and offset at around the time of ventral stroke reversal (i.e. at wingbeat phase $\varphi \approx \pi$). Conversely, PC1 in E. pertinax and PC3 in *Drosophila* emphasise changes in twist gradient and offset at around the time of dorsal stroke reversal (i.e. at wingbeat phase $\varphi \approx 0$). The remaining PCs involve substantial changes in twist gradient and offset throughout most of the stroke, which is particularly clear for PC3 in *E. tenax* and *E. pertinax*.

Although the wing twist offset $\omega_0(t)$ and gradient $\omega_r(t)$ vary most strongly at dorsal and ventral stroke reversal (Figure 7), they tend to vary in opposition and therefore counteract each other in their effects on the local pitch angle of the wing $\omega(r, t)$. As is apparent from the time history of the local pitch angle of the wing at mid-span (Figure 7), this means that the net perturbation of the local pitch angle can be most substantial at phases of the stroke cycle involving weaker but synergistic perturbations in $\omega_r(t)$ and $\omega_0(t)$. For example, of the four PCs that emphasise changes in twist gradient and offset at ventral stroke reversal (i.e. at wingbeat phase $\varphi \approx \pi$), only PC2 in *Drosophila* produces changes in mid-span pitch angle that are greatest at ventral stroke reversal. In most other cases, the resulting changes in mid-span pitch angle are greatest towards the middle of the upstroke or downstroke (Figure 8).

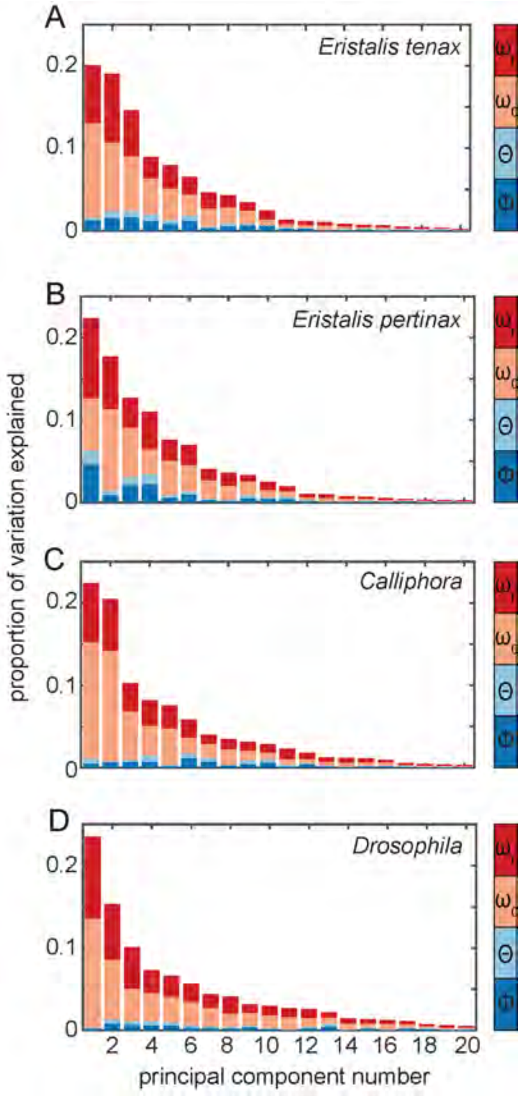

Figure 5. *Proportion of the between-wingbeat variation in the time-periodic wingbeat kinematics that is explained by the first 20 principal components for four species of dipteran fly, partitioned according to the variation in stroke angle* ϕ*, deviation angle* θ*, twist offset* ω_0*, and twist gradient* ω_r*. Note the strong contribution of the wing twist variables to the kinematic variation between wingbeats.*

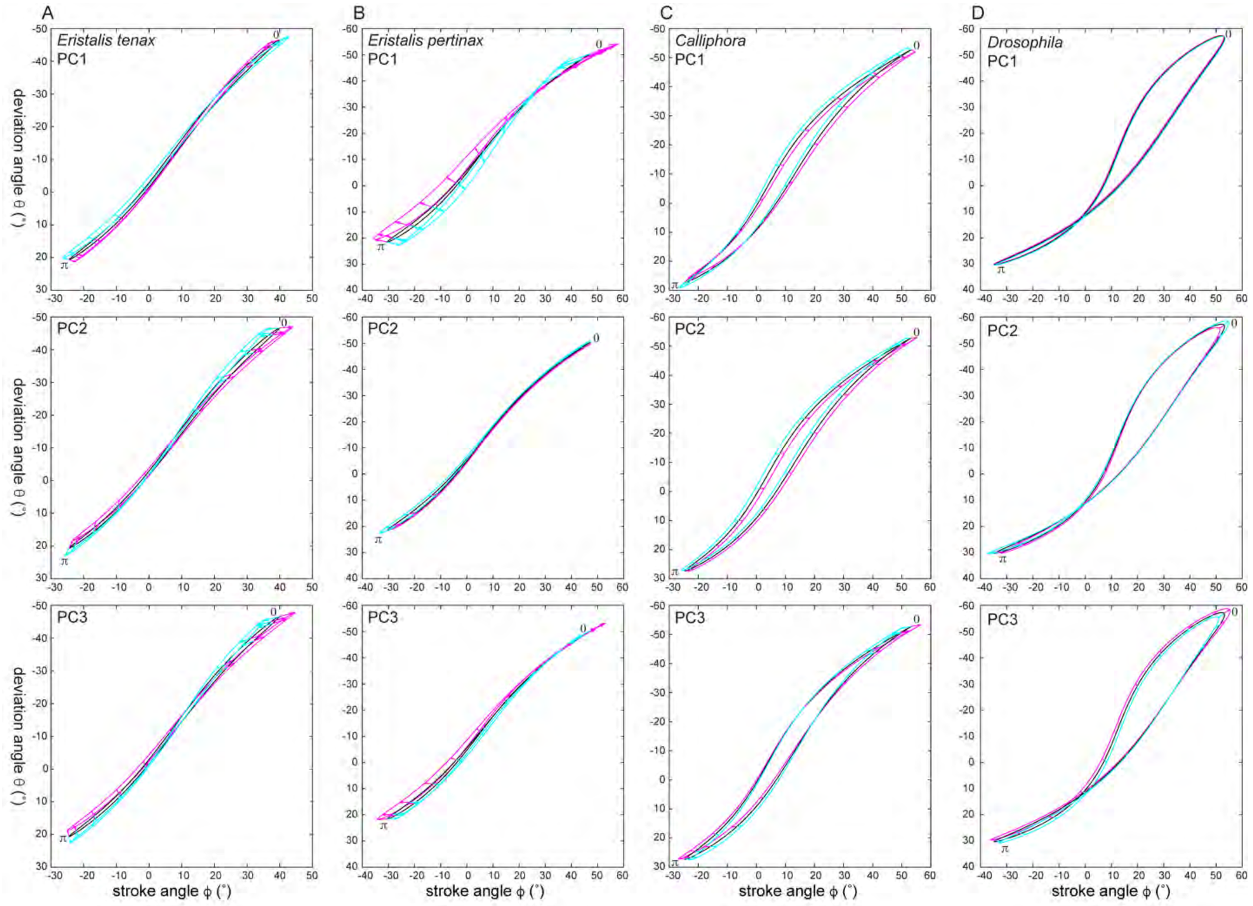

Figure 6. *Phase-plane plots showing the variation in the time-periodic wing tip kinematics described by each of the first three principal components (PC1-PC3) for four species of dipteran fly. Black lines display the mean wing tip kinematics; cyan and magenta lines display the effect of a ±1 SD perturbation in each PC; arrows connect points of equivalent phase. The point of dorsal stroke reversal is defined as phase* $\varphi = 0$*; the point of ventral stroke reversal corresponds approximately to phase* $\varphi = \pi$*. Note that the primary effect of perturbing these PCs is to tilt the stroke plane with respect to the body axes–exceptions being PC2 in Calliphora, which describes a wholesale fore-aft displacement of the stroke plane; and PC1 in Drosophila, which involves almost no change in wing tip trajectory. These changes in the wing tip kinematics are coupled with the changes in wing twist kinematics shown in Figure 7.*

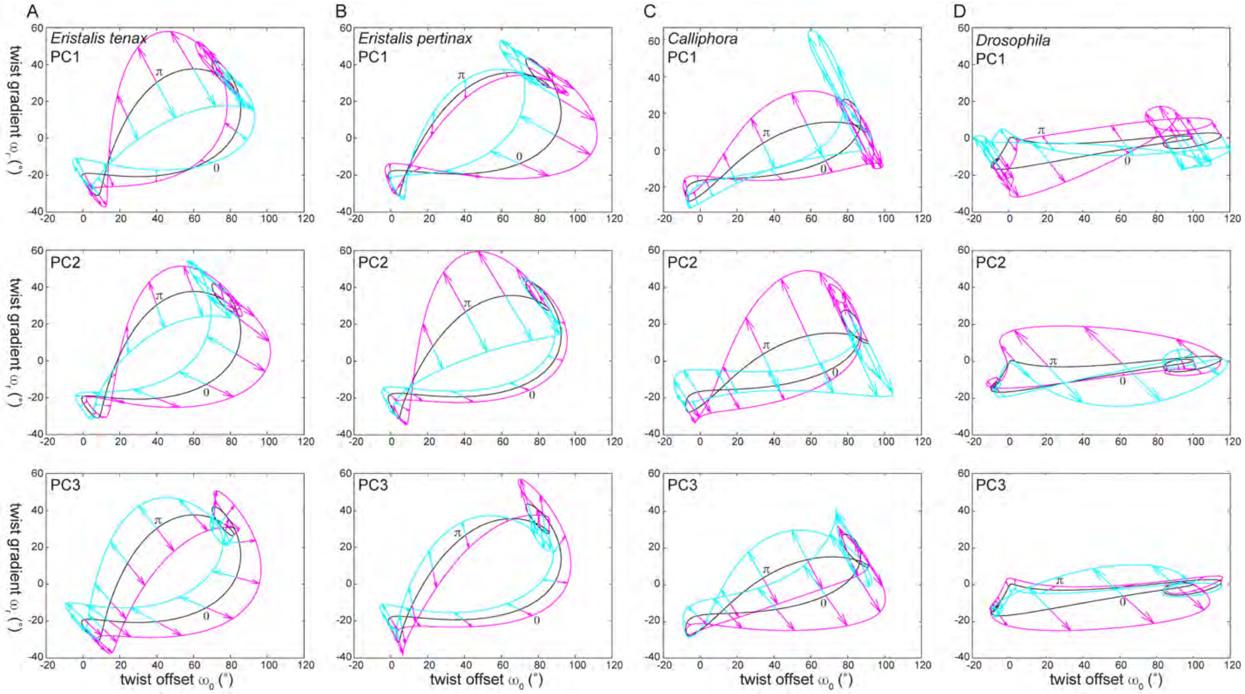

Figure 7. *Phase-plane plots showing the variation in the time-periodic wing twist kinematics described by each of the first three principal components (PC1-PC3) for four species of dipteran fly. Black lines display the mean wing twist kinematics; cyan and magenta lines display the effect of a ±1 SD perturbation in each PC; arrows connect points of equivalent phase. The point of dorsal stroke reversal is defined as phase* $\varphi = 0$*; the point of ventral stroke reversal corresponds approximately to phase* $\varphi = \pi$*. Note that the tilting of the stroke plane that these same PCs describe (see Figure 6) is shown here to be coupled with some quite complicated changes in the wing twist kinematics, which vary most as the wing undergoes rapid pronation (or supination) at dorsal (or ventral) stroke reversal.*

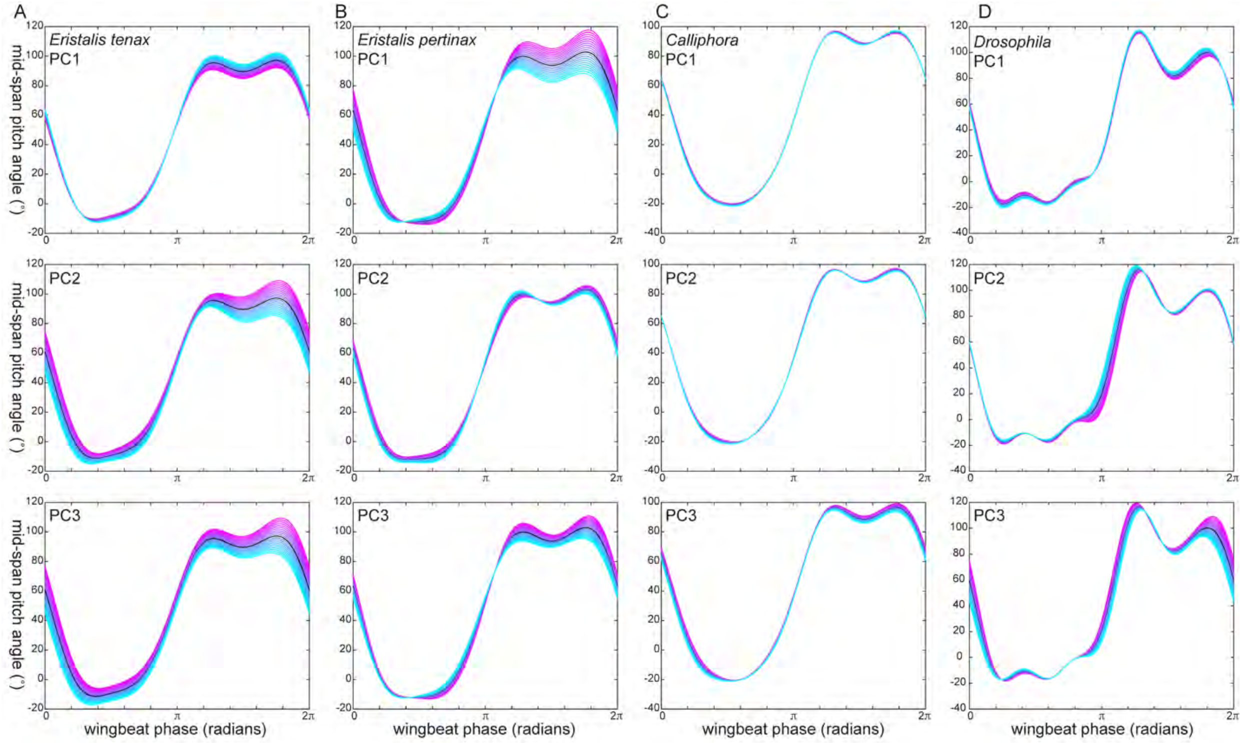

Figure A7. *Time history of the mid-span pitch angle of the wing, showing the effect of each of the first three principal components (PC1-PC3) for four species of dipteran fly. Black lines display the mean wing twist kinematics; cyan and magenta lines display the effect of a ±1 SD perturbation in each PC. The point of dorsal stroke reversal is defined as phase* $\varphi = 0$*; the point of ventral stroke reversal corresponds approximately to phase* $\varphi = \pi$*. Note that although the wing twist kinematics vary most at dorsal (or ventral) stroke reversal (Figure 7), opposing perturbations to the wing twist offset and gradient will counteract one another in their effects on the local pitch angle of the wing. The resulting change in the mid-span pitch angle is therefore often greatest at mid-upstroke or mid-downstroke, when the translational speed of the wing is highest.*

2.1.2.4 Cross-species similarities in flight control

Notwithstanding the complexity of the multi-dimensional kinematic couplings that they describe (Figures 6-7), each PC is specified by a vector of Fourier coefficients forming one of the columns of the PC matrix $\mathbf{V}$. The complete set of vectors for each species forms a unique orthonormal basis spanning the entire kinematic space that we have defined, and any similarity of the ordered basis $\mathbf{V_1}$ of one species to the ordered basis $\mathbf{V_2}$ of another is represented by diagonal structure in their matrix of inner products $\mathbf{R} = \mathbf{V_1^T V_2}$ (see Methods). Moreover, because the PCs contained in $\mathbf{V_1}$ and $\mathbf{V_2}$ are ordered according to the amount of variation that they explain, any diagonal or block-diagonal structure in the upper-left block of $\mathbf{R}$ indicates similarity among the first few PCs of each species, and hence similarity in the kinematic subspace that they utilise. Conversely, any diagonal or block-diagonal structure in the lower-right block of $\mathbf{R}$ indicates similarity among the last few PCs of each species, and hence similarity in the kinematic subspace that they do not–or cannot–utilise. Such diagonal structure can be seen in the bitmap plots of the absolute values of $\mathbf{R}$ for each species dyad (Figure 9), and is most obvious between *E. tenax* and *E. pertinax*–particularly for the last few PCs representing their un-utilised kinematic subspace.

Although there is a high degree of similarity in the ordered basis that the FPCA identifies for *E. tenax* and *E. pertinax* respectively ($\tilde{S} = 0.74$), neither species' ordered basis displays more than a moderate similarity to that of *Calliphora* ($0.50 \leq \tilde{S} \leq 0.52$), and the ordered basis identified for *Drosophila* is quite dissimilar to those of the other species ($0.26 \leq \tilde{S} \leq 0.28$). Even so, there is more similarity between the genera than first appears. For instance, it is clear by inspection that PC1 in *E. pertinax* corresponds closely to PC2 in *Calliphora* (Figure 9). Optimally reordering the PCs to best-match the pairs within a dyad (Figure 10) reveals an even higher similarity in the basis identified for *E. tenax* and *E. pertinax* ($\tilde{S}^* = 0.82$), high similarity in the basis identified for *E. tenax* or *E. pertinax* and *Calliphora* ($0.69 \leq \tilde{S}^* \leq 0.73$), and moderate similarity in the basis identified for Drosophila and each of the other three species ($0.57 \leq \tilde{S}^* \leq 0.58$). It is important to note, however, that these statements relate only to the similarity in the basis that the FPCA identifies for each species, and need not imply a high degree of similarity in the leading PCs describing the kinematic subspace that the insects actually use in their flight control. The latter is better assessed by the weighted mean similarity metric $\tilde{S}_w^*$ (see Methods) which uses the singular values describing the importance of each of the PCs as weights. This metric reveals a moderate to high degree of similarity among all of the species ($0.58 \leq \tilde{S}_w^* \leq 0.73$), with *Calliphora* and the two species of *Eristalis* being generally quite similar in the kinematic couplings that they prioritise in their flight control ($0.67 \leq \tilde{S}_w^* \leq 0.73$), and *Drosophila* being less so $0.58 \leq \tilde{S}_w^* \leq 0.63$.

Table 2. *Kinematic similarity within the six species dyads. Here, the metric $\bar{S}$ is the normalised inner product of the vectors of Fourier coefficients describing the mean wingbeat kinematics of the species within a dyad; $\tilde{S}$ is the mean absolute inner product of their ordered principal component (PC) coefficient vectors; $\tilde{S}^*$ is the mean absolute inner product of their optimally-reordered PC coefficient vectors; $\tilde{S}_w^*$ is the weighted mean absolute inner product of their optimally-reordered PC coefficient vectors, using their singular values as weights. All metrics take values on the interval from 0 to 1; see Methods for further details.*

species dyad			$\bar{S}$	$\tilde{S}$	$\tilde{S}^*$	$\tilde{S}_w^*$
E. pertinax	×	*E. tenax*	0.998	0.736	0.817	0.710
E. pertinax	×	*Calliphora*	0.977	0.504	0.690	0.671
E. tenax	×	*Calliphora*	0.969	0.520	0.727	0.732
E. pertinax	×	*Drosophila*	0.916	0.255	0.583	0.633
E. tenax	×	*Drosophila*	0.902	0.256	0.567	0.577
Calliphora	×	*Drosophila*	0.962	0.276	0.566	0.586

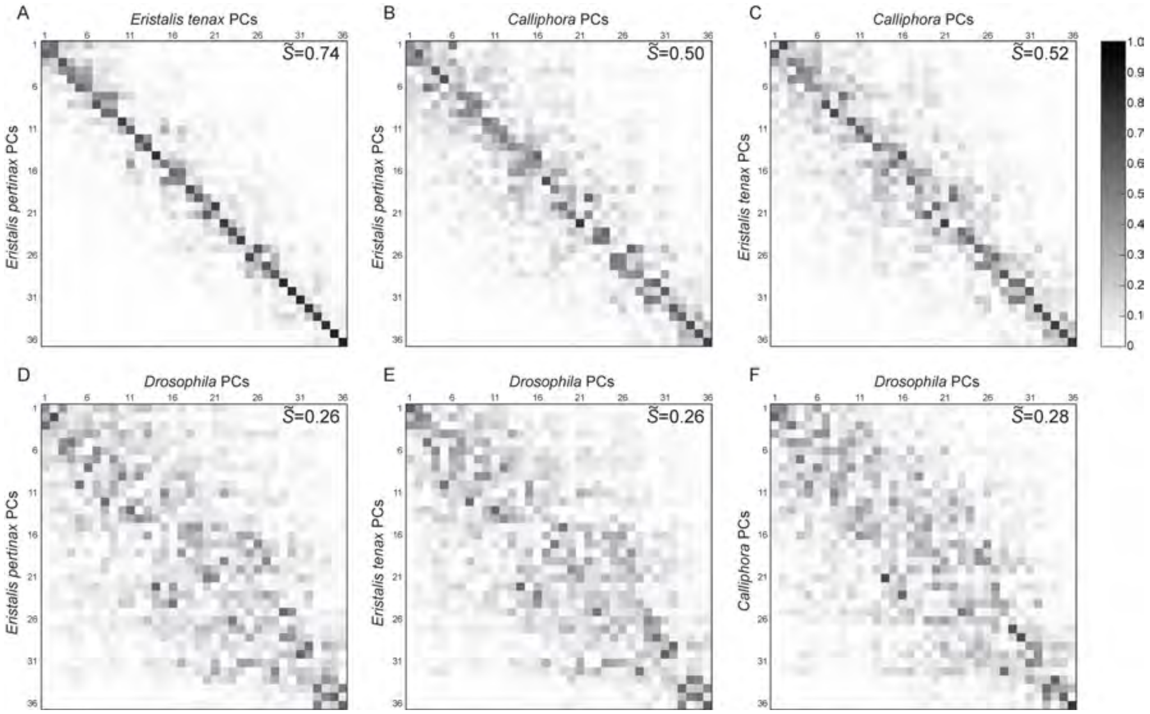

***Figure 9**. Bitmap of the matrix of inner products $\boldsymbol{R} = \boldsymbol{V}_1^T\boldsymbol{V}_2$ comparing the ordered basis defined by the principal component (PC) matrix for one species of dipteran fly ($\boldsymbol{V}_1$) to that of another ($\boldsymbol{V}_2$). The grayscale value of the elements is linearly related to the magnitude of the inner product R_{ij} between the i^{th} PC for one species and the j^{th} PC for the other: black indicates perfect similarity, $|R_{ij}| = 1$; white indicates no similarity, $|R_{ij}| = 0$. The overall degree of similarity between the ordered basis identified for each species within a dyad is summarised by the mean similarity metric $\tilde{S}$, where $\tilde{S} = 1$ would denote perfect similarity implying diagonality of $\boldsymbol{R}$. Note (A) the presence of strong block diagonal structure between Eristalis tenax and E. pertinax; (B,C) the weaker block diagonal structure present between Eristalis spp. and Calliphora; and (D-F) the lack of much clear structure when comparing any of these three species to Drosophila. Any such diagonal structure indicates similarity in the ordered basis describing the kinematic couplings of the species within a dyad, and implies that the two species prioritize these couplings similarly in their flight control.*

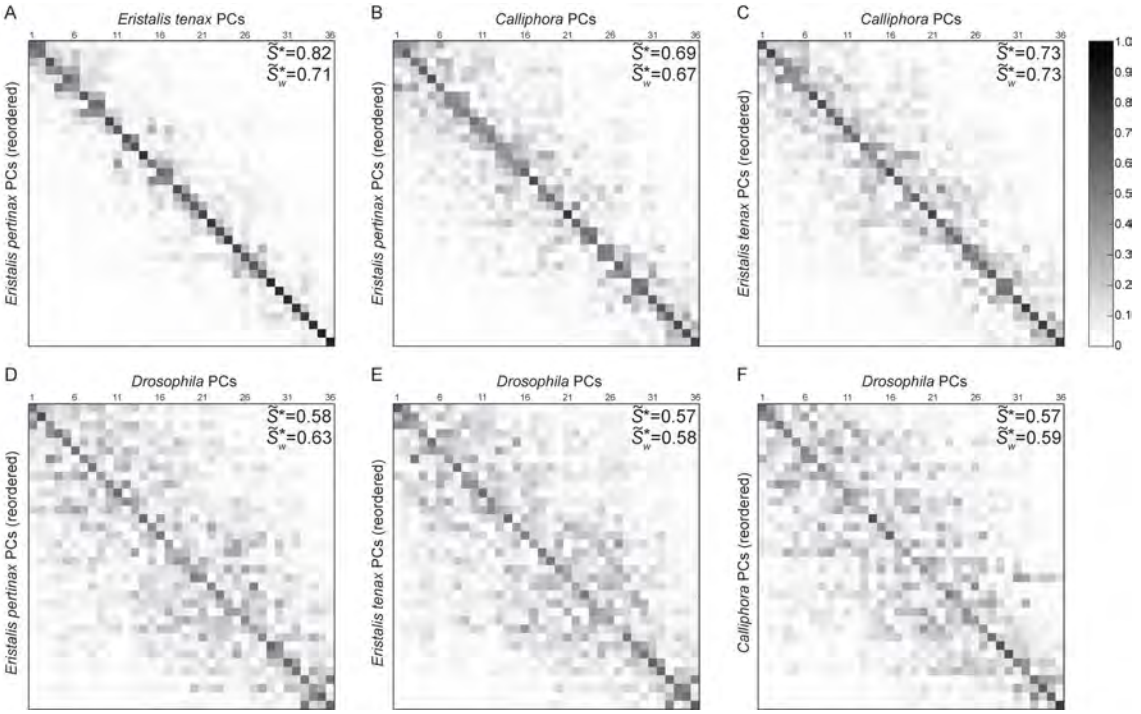

Figure 10. *Bitmap of the permuted matrix of inner products $\boldsymbol{R}^* = \boldsymbol{V}_{1*}^{\mathrm{T}}\boldsymbol{V}_2$ comparing the basis defined by the principal component (PC) matrix for one species of dipteran fly ($\boldsymbol{V}_{1*}$) to that of another ($\boldsymbol{V}_2$), having reordered the PCs in $\boldsymbol{V}_{1*}$ so as to maximise the trace of the absolute values of $\boldsymbol{R}^*$. The grayscale value of the elements is linearly related to the magnitude of the inner product R^*_{ij} between the i^{th} re-ordered PC for one species and the j^{th} PC for the other: black indicates perfect similarity, $|R^*_{ij}| = 1$; white indicates no similarity, $|R^*_{ij}| = 0$. The overall degree of similarity between the basis identified for each species within a dyad is summarised by the maximal similarity metric $\tilde{S}^*$, where $\tilde{S}^* = 1$ would denote perfect similarity implying diagonality of $\boldsymbol{R}^*$. Note (A) the presence of strong block diagonal structure between Eristalis tenax and E. pertinax; (B,C) the clear block diagonal structure present between Eristalis spp. and Calliphora; and (D-F) the presence of some block diagonal structure revealed by the reordering when comparing any of these three species to Drosophila. Any such diagonal structure indicates similarity in the basis describing the kinematic couplings of the species within a dyad, but need not imply that the two species prioritise these couplings similarly in their flight control. This is better assessed by the weighted mean similarity metric $\tilde{S}^*_w$, which uses the singular values describing the importance of each of the PCs as weights.*

2.2 *Flight dynamics modelling of the blowfly Calliphora*

Having defined a natural vector basis in which to define the input vector $\boldsymbol{u}$, it remains to use this to specify the control matrix $\mathbf{B}$, and separately to specify the system matrix $\mathbf{A}$. The elements of the $\mathbf{A}$ and $\mathbf{B}$ matrices involve the partial derivatives of the aerodynamic forces and moments with respect to the system state $\mathbf{x}$ and input vector $\boldsymbol{u}$. These are called stability and control derivatives, and their aerodynamic modelling using computational fluid dynamics (CFD) techniques is elaborated in Section 3 below. The effect of changes in the aerodynamic forces and moments on the system state $\mathbf{x}$ depends also on the inertial properties of the insect, so constructing the $\mathbf{A}$ and $\mathbf{B}$ matrices requires knowledge of the inertia tensor. This is not straightforward to obtain for the heterogeneous body of an insect weighing on the order of 100 mg, but we describe below the results of a method doing so using synchrotron-based micro-computed tomography (μCT). We begin by describing the formulation of the flight dynamics model; note that some of the notation used in this section and hereafter has a different meaning to that used in the previous section.

2.2.1 Linear Time Invariant (LTI) flight dynamics modelling

As outlined above, we aim to generate a linear time-invariant flight dynamics model of the form:

$$\dot{\boldsymbol{x}}(t) = \mathbf{A}\boldsymbol{x}(t) + \mathbf{B}\boldsymbol{u}(t) + \mathbf{G}\boldsymbol{d}(t)$$

where the state vector $\boldsymbol{x} = [\delta u, \delta w, \delta q, \delta \theta, \delta v, \delta p, \delta \phi, \delta r]^{\mathrm{T}}$ is sufficient to describe the 6-DoF rigid body motions of the insect insofar as these motions either influence the wingbeat-averaged aerodynamic forces $\{X, Y, Z\}$ and moments $\{L, M, N\}$ resolved in the principal axes of the body $\{x, y, z\}$, or influence the components of the insect's body weight resolved in these same principal axes. Here, δ denotes a small perturbation from equilibrium, where $\{u, v, w\}$ are the components of translational velocity along the principal axes of the body, where $\{p, q, r\}$ are the components of angular velocity about these body axes, and where $\{\theta, \phi\}$ are the pitch and bank of the insect. These Euler angles are defined as the second and third rotations in an intrinsic *z*-*y*-*x* rotation sequence bringing the body axes to their final orientation, starting from an initial configuration in which the *z*-axis is vertical. Note that the azimuth angle ψ about the *z*-axis is not included in the system state, because it has no influence on the flight physics. The linearization of the equations of motion for a rigid flying body using small perturbation theory is dealt with in most flight dynamics texts, so is not repeated here. In brief, we model the insect as a symmetric rigid body that is subject to wingbeat-averaged aerodynamic forces and moments that are modelled as linear functions of the motion state variables $\{u, v, w, p, q, r\}$ and control input variables $\boldsymbol{u}$ for small perturbations from a symmetric rectilinear equilibrium flight condition. See Taylor & Thomas (2003) for discussion of this approach in the context of insect flight dynamics, including the wingbeat-averaging of the aerodynamic forces and moments, which is an approach borrowed from simplified helicopter flight dynamics modelling.

With these definitions and assumptions, we model the longitudinal flight dynamics $\dot{\boldsymbol{x}}_{\mathbf{long}}(t) = \mathbf{A}_{\mathbf{long}}\boldsymbol{x}_{\mathbf{long}}(t) + \mathbf{B}_{\mathbf{long}}\boldsymbol{u}_{\mathbf{long}}(t)$ as:

$$\begin{bmatrix} \delta\dot{u} \\ \delta\dot{w} \\ \delta\dot{q} \\ \delta\dot{\theta} \end{bmatrix} = \begin{bmatrix} \dfrac{X_u}{m} & \dfrac{X_w}{m} & \dfrac{X_q}{m} - w_e & -g\cos\theta_e \\ \dfrac{Z_u}{m} & \dfrac{Z_w}{m} & \dfrac{Z_q}{m} + u_e & -g\sin\theta_e \\ \dfrac{M_u}{I_y} & \dfrac{M_w}{I_y} & \dfrac{M_q}{I_y} & 0 \\ 0 & 0 & 1 & 0 \end{bmatrix} \begin{bmatrix} \delta u \\ \delta w \\ \delta q \\ \delta\theta \end{bmatrix} + \begin{bmatrix} \dfrac{X_{\mathrm{u}_0}}{m} & \dfrac{X_{\mathrm{u}_1}}{m} & \dots & \dfrac{X_{\mathrm{u}_4}}{m} \\ \dfrac{Z_{\mathrm{u}_0}}{m} & \dfrac{Z_{\mathrm{u}_1}}{m} & \dots & \dfrac{Z_{\mathrm{u}_4}}{m} \\ \dfrac{M_{\mathrm{u}_0}}{I_y} & \dfrac{M_{\mathrm{u}_1}}{I_y} & \dots & \dfrac{M_{\mathrm{u}_4}}{I_y} \\ 0 & 0 & \dots & 0 \end{bmatrix} \begin{bmatrix} \mathrm{u}_0 \\ \mathrm{u}_1 \\ \vdots \\ \mathrm{u}_4 \end{bmatrix}$$

where $\{u_e, w_e, \theta_e\}$ are the values of $\{u, w, \theta\}$ at equilibrium, where g is gravitational acceleration, m is body mass, and I_y is the moment of inertia about the y-axis. Here the control input u_0 denotes a change of wingbeat frequency with respect to equilibrium, whilst the remaining control inputs

$\{u_1, \ldots, u_4\}$ denote mirror-symmetric application of the time-periodic kinematic couplings in the directions defined by PC1 through to PC4 (see Section 2.1 above). Quantities of the form X_u, Z_w, M_q, etc. are stability derivatives, denoting the partial derivatives $\partial X/\partial u$, $\partial Z/\partial w$, $\partial M/\partial q$, etc. Likewise, quantities of the form X_{u_0}, Z_{u_1}, M_{u_4}, etc. are control derivatives, denoting the partial derivatives $\partial X/\partial \mathrm{u}_0$, $\partial Z/\partial \mathrm{u}_1$, $\partial M/\partial \mathrm{u}_4$, etc. Section 3 describes our method of estimating these derivatives by regressing the wingbeat-averaged forces and moments predicted using CFD on the relevant state variables and control input variables. Note that for the purposes of the flight dynamics modelling described here, we regress the perturbed forces and moments on the perturbed state variables and control input variables, and therefore force the regressions through the origin.

If we assume gusts $\boldsymbol{d}(t) = \{u_d, v_d, w_d, p_d, q_d, r_d\}$ are present in the atmosphere, we replace the motion state variables $\{u, v, w, p, q, r\}$ in the perturbation forces and moments (ΔX, ΔM, etc.) with revised versions $\{u_a, v_a, w_a, p_a, q_a, r_a\}$ where we include the original inertial component and a disturbance (gust) component:

$$u_a = u - u_d,\ v_a = v - v_d,\ w_a = w - w_d$$
$$p_a = p - p_d,\ q_a = q - q_d,\ r_a = r - r_d$$

Under this assumption, the perturbation forces and moments on the vehicle now are a function of both the inertial and gust components. Without writing the full equations out for brevity, we can understand how the entries of the **G** matrix are derived from the entries of the **A** matrix by examining the first component of ΔX. In a quiescent atmosphere, $\Delta X = {}^{\partial X}\!/_{\partial u}\, u$. If we replace u with u_a, we have $\Delta X = {}^{\partial X}\!/_{\partial u}\,(u - u_d)$. Hence, the way the gust u_d enters the model is through $-{}^{\partial X}\!/_{\partial u}\, u_d$, which are the negative of the aerodynamic portions of the **A** matrix when solved for $\dot{\boldsymbol{x}}$.

The longitudinal flight dynamics model with gusts are modelled as $\dot{\boldsymbol{x}}_{\mathbf{long}}(t) = \mathbf{A}_{\mathbf{long}}\boldsymbol{x}_{\mathbf{long}}(t) + \mathbf{G}_{\mathbf{long}}\boldsymbol{d}_{\mathbf{long}}(t)$,

$$\begin{bmatrix} \delta\dot{u} \\ \delta\dot{w} \\ \delta\dot{q} \\ \delta\dot{\theta} \end{bmatrix} = \begin{bmatrix} \frac{X_u}{m} & \frac{X_w}{m} & \frac{X_q}{m} - w_e & -g\cos\theta_e \\ \frac{Z_u}{m} & \frac{Z_w}{m} & \frac{Z_q}{m} + u_e & -g\sin\theta_e \\ \frac{M_u}{I_y} & \frac{M_w}{I_y} & \frac{M_q}{I_y} & 0 \\ 0 & 0 & 1 & 0 \end{bmatrix} \begin{bmatrix} \delta u \\ \delta w \\ \delta q \\ \delta\theta \end{bmatrix} + \begin{bmatrix} -\frac{X_u}{m} & -\frac{X_w}{m} & -\frac{X_q}{m} \\ -\frac{Z_u}{m} & -\frac{Z_w}{m} & -\frac{Z_q}{m} \\ -\frac{M_u}{I_y} & -\frac{M_w}{I_y} & -\frac{M_q}{I_y} \\ 0 & 0 & 0 \end{bmatrix} \begin{bmatrix} u_d \\ w_d \\ q_d \end{bmatrix}$$

The lateral flight dynamics $\dot{\boldsymbol{x}}_{\mathbf{lat}}(t) = \mathbf{A}_{\mathbf{lat}}\boldsymbol{x}_{\mathbf{lat}}(t) + \mathbf{B}_{\mathbf{lat}}\boldsymbol{u}_{\mathbf{lat}}(t)$ are modelled as:

$$\begin{bmatrix} \delta\dot{v} \\ \delta\dot{p} \\ \delta\dot{\phi} \\ \delta\dot{r} \end{bmatrix} = \begin{bmatrix} \frac{Y_v}{m} & \frac{Y_p}{m} + w_e & g\cos\theta_e & \frac{Y_r}{m} - u_e \\ \frac{L_v}{I_x} & \frac{L_p}{I_x} & 0 & \frac{L_r}{I_x} \\ 0 & 1 & 0 & \tan\theta_e \\ \frac{N_v}{I_z} & \frac{N_p}{I_z} & 0 & \frac{N_r}{I_z} \end{bmatrix} \begin{bmatrix} \delta v \\ \delta p \\ \delta\phi \\ \delta r \end{bmatrix} + \begin{bmatrix} \frac{Y_{\mathrm{u}_1'}}{m} & \frac{Y_{\mathrm{u}_2'}}{m} & \frac{Y_{\mathrm{u}_3'}}{m} & \frac{Y_{\mathrm{u}_4'}}{m} \\ \frac{L_{\mathrm{u}_1'}}{I_x} & \frac{L_{\mathrm{u}_2'}}{I_x} & \frac{L_{\mathrm{u}_3'}}{I_x} & \frac{L_{\mathrm{u}_4'}}{I_x} \\ 0 & 0 & 0 & 0 \\ \frac{N_{\mathrm{u}_1'}}{I_z} & \frac{N_{\mathrm{u}_2'}}{I_z} & \frac{N_{\mathrm{u}_3'}}{I_z} & \frac{N_{\mathrm{u}_4'}}{I_z} \end{bmatrix} \begin{bmatrix} \mathrm{u}_1' \\ \mathrm{u}_2' \\ \mathrm{u}_3' \\ \mathrm{u}_4' \end{bmatrix}$$

where the notation is similar, save that the control inputs $\{\mathrm{u}_1', \dots, \mathrm{u}_4'\}$ denote anti-symmetric application of the time-periodic kinematic couplings in the directions defined by PC1 through to PC4 (see Section 2.1 above). Note that these equations of motion are linearized about a symmetric rectilinear equilibrium flight condition with $v_e = p_e = q_e = r_e = \phi_e = 0$, and neglect any gyroscopic forces on the beating wings. They further assume that the fastest natural modes of the system have a characteristic timescale much longer than the period of the wingbeat, such that there is no significant coupling between the time-periodic oscillations of the aerodynamic forces and the body's motion. Finally, note that their simplified form reflects the fact that all of the forces and moments are resolved with respect to the principal axes of the insect.

The lateral flight dynamics model with gusts $\dot{\boldsymbol{x}}_{\mathbf{lat}}(t) = \mathbf{A}_{\mathbf{lat}}\boldsymbol{x}_{\mathbf{lat}}(t) + \mathbf{G}_{\mathbf{lat}}\boldsymbol{d}_{\mathbf{lat}}(t)$ is derived exactly the same as its longitudinal counterpart, and are modelled as:

$$\begin{bmatrix} \delta\dot{v} \\ \delta\dot{p} \\ \delta\dot{\phi} \\ \delta\dot{r} \end{bmatrix} = \begin{bmatrix} \frac{Y_v}{m} & \frac{Y_p}{m} + w_e & g\cos\theta_e & \frac{Y_r}{m} - u_e \\ \frac{L_v}{I_x} & \frac{L_p}{I_x} & 0 & \frac{L_r}{I_x} \\ 0 & 1 & 0 & \tan\theta_e \\ \frac{N_v}{I_z} & \frac{N_p}{I_z} & 0 & \frac{N_r}{I_z} \end{bmatrix} \begin{bmatrix} \delta v \\ \delta p \\ \delta\phi \\ \delta r \end{bmatrix} + \begin{bmatrix} -\frac{Y_v}{m} & -\frac{Y_p}{m} & -\frac{Y_r}{m} \\ -\frac{L_v}{I_x} & -\frac{L_p}{I_x} & -\frac{L_r}{I_x} \\ 0 & 0 & 0 \\ -\frac{N_v}{I_z} & -\frac{N_p}{I_z} & -\frac{N_r}{I_z} \end{bmatrix} \begin{bmatrix} v_d \\ p_d \\ r_d \end{bmatrix}$$

2.2.2 Parameterisation of the stability and control derivatives for the blowfly Calliphora

Parameter estimates for the stability and control derivatives of *Calliphora* are obtained using a CFD model of an isolated flapping wing (see Section 3) and are computed with respect to the reference flight condition associated with the mean wingbeat identified in the FPCA (Section 2.1). This aerodynamic modelling of a single wing results in non-zero partial derivatives of the longitudinal (lateral) forces and moments with respect to the lateral (longitudinal) states (Section 3.4), which cancel when the anti-symmetric contributions of the left and right wings are summed. On the other hand, and for the same reason, the magnitude of the pure-lateral and pure-longitudinal stability and control derivatives appearing in the **A** and **B** matrices is twice that shown in Section 3.4.

2.2.3 *Enforcement of equilibrium in the model of* Calliphora *flight dynamics*

Although we do not derive the LTI model of the flight dynamics explicitly above, a key feature of this model is that it is linearized about a state of equilibrium, which is a necessary condition for time-invariant equations of motion to result from the linearization. Whilst it is reasonable to assume that the reference flight condition associated with the mean wingbeat in the FPCA will be close to equilibrium, there is no reason to expect that it will be exactly so. To guarantee the internal consistency of the model, we therefore enforce equilibrium, subject to the assumption: (i) that $v_e = p_e = q_e = r_e = \phi_e = 0$ on grounds of symmetry; and (ii) that $\{u_e, w_e, \theta_e\}$ are each equal to the reference conditions assumed in the CFD modelling. We achieve this by making three assumptions. First, we assume that the magnitude of the vertical aerodynamic force predicted by the CFD under the reference flight conditions is exactly balanced by the insect's body weight. We therefore solve for the value of body mass at which this assumption holds and set m equal to this value in the flight dynamics model. Second, we assume that the net thrust predicted by the CFD under the reference flight conditions is exactly balanced by body drag in forward flight. This body drag does not feature explicitly in the flight dynamics model, because it is implicit in the treatment of the reference flight conditions from the CFD as an equilibrium condition. Third, noting that the aerodynamic moments predicted by the CFD are resolved at the root of the wing, we assume that the any non-zero pitching moment about the wing root is balanced at the centre of mass by the vertical aerodynamic force. We therefore solve for the horizontal lever arm in the *xz*-plane for which this assumption holds and assume that the wing root is located on a known transverse lever arm along the y-axis that we obtain from the μCT below. We then resolve all of the aerodynamic moments at the centre of mass prior to taking the stability and control derivatives above.

2.2.4 *Parameterisation of the inertia tensor for* Calliphora

We estimate the mass moments of inertia $\{I_x, I_y, I_z,\}$ about the principal axes of the insect from new μCT images of freshly killed individuals. Two male and one female *C. vicina* from the Imperial colony were sealed in 0.5mL Eppendorf tubes having been fed and watered to satiation and weighed. The tubes were placed individually in the TOMCAT beamline of the Swiss Light Source synchrotron facility and were irradiated at 12 keV beam energy until the flies were dead and there were no further motion artefacts occurring. A 100 μm thick, Ce-doped LuAG scintillator was placed at a distance of 272mm behind the sample to convert the transmitted X-rays into visible light. The resulting image was magnified 2-fold using an Edge 5.5 Microscope, and 1501 projection images at 60 ms exposure time whilst the sample was rotated through 180°. To image the entirety of each fly, it was necessary to image three overlapping volumes in this way. Phase retrieval was performed using the Paganin algorithm, setting the real and imaginary parts of the deviation from one of the complex refractive index of the material to $\delta = 1 \times 10^{-7}$ and $\beta = 1 \times 10^{-9}$ respectively. Tomographic reconstruction was performed using a Fourier transform-based algorithm, resulting in voxels with an isotropic spacing of 3.25 μm.

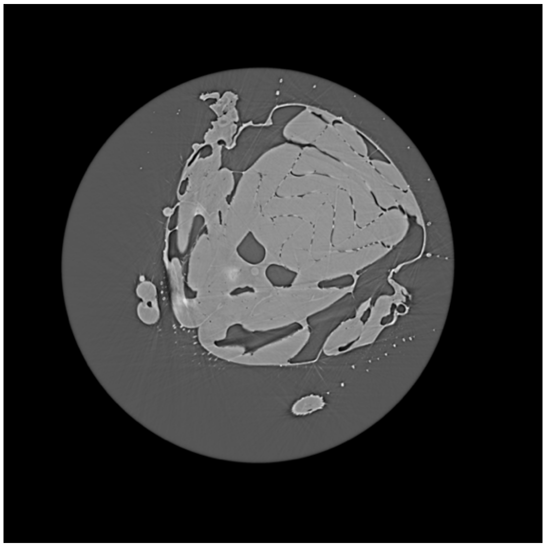

***Figure 11**. Segmented μCT image, comprising a transverse slice of a female Calliphora vicina mid-thorax; this is one of >4500 slices in the stack used to estimate the mass moments of inertia.*

The tomograms were segmented automatically, using thresholding and morphological operations to mask voxels corresponding to the cross-section of the Eppendorf tube and any exterior voxels. The tomograms were then combined into one continuous stack across the three samples for each specimen, using obvious cross-sectional features such as hairs to align the image stacks manually along their common longitudinal axis. The complete image stack was loaded into Fiji, and the BoneJ plugin was used to calculate the mass moments of inertia about the principal axes of the specimen, assuming a uniform density of 1.1 g cm^{-3} appropriate to insect cuticle and muscle. The mass estimates arrived at using this method (Table 3) were identical to the weights taken at the start of the experiment to within the 0.01g readability of the balance. Because the moments of inertia about the first and second principal axes were identical to within ±1% (Table 3), we set $I_y = I_z$ for the purposes of the flight dynamics modelling, and set I_x equal to the moment of inertia about the third principal axis. Assuming isometry, we non-dimensionalized the moments of inertia by dividing through by $m^{5/3}$, then rescaled these using the value of m that we had assumed in the flight dynamics model (Section 2.2.3) before entering them into the flight dynamics model.

***Table 3**. Moments of inertia about the principal axes of Calliphora vicina estimated from μCT images.*

insect	m (10^{-5} kg)	I_1 (10^{-10} kg m^2)	I_2 (10^{-10} kg m^2)	I_3 (10^{-10} kg m^2)
Male 1	6.792	5.802	5.730	1.457
Male 2	7.543	6.410	6.368	1.594
Female 1	7.953	6.924	6.883	1.822

2.2.5 *Parameterised flight dynamics model for* Calliphora

With these assumptions and parameterizations, the longitudinal and lateral **A**, **B** and **G** matrices for *Calliphora* are as follows, in S.I. units:

$$\mathbf{A}_{\text{long}} = \begin{bmatrix} -1.4471 & 2.1998 & -0.4351 & -8.4614 \\ -2.4284 & -2.3400 & 0.7282 & -4.9573 \\ 547.09 & 345.54 & -4.8501 & 0 \\ 0 & 0 & 1 & 0 \end{bmatrix}$$

$$\mathbf{A}_{\text{lat}} = \begin{bmatrix} -1.9492 & 0.4250 & 8.4614 & -0.7314 \\ 697.24 & -83.067 & 0 & 90.875 \\ 0 & 1 & 0 & 0.5859 \\ 751.82 & -12.546 & 0 & -3.1760 \end{bmatrix}$$

$$\mathbf{B}_{\text{long}} = \begin{bmatrix} 0.0837 & -0.1600 & 0.3249 & -0.2789 & -0.7515 \\ -0.0768 & 0.0380 & 0.1615 & 0.4448 & -0.0946 \\ -5.1932 & 413.65 & 74.900 & 159.80 & -233.11 \\ 0 & 0 & 0 & 0 & 0 \end{bmatrix}$$

$$\mathbf{B}_{\text{lat}} = \begin{bmatrix} -0.4536 & -0.1212 & -0.0403 & -0.6952 \\ 36.391 & 777.94 & 900.06 & 556.56 \\ 404.05 & -526.60 & 260.11 & 602.64 \\ 0 & 0 & 0 & 0 \end{bmatrix}$$

$$\mathbf{G}_{\mathbf{long}} = \begin{bmatrix} 1.4471 & -2.1998 & 0.0050 \\ 2.4284 & 2.3400 & 0.0060 \\ -547.09 & -345.54 & 4.8501 \\ 0 & 0 & 0 \end{bmatrix}$$

$$\mathbf{G}_{\mathbf{lat}} = \begin{bmatrix} 1.9492 & 0.0051 & -0.0028 \\ -697.24 & 83.067 & -90.875 \\ 0 & 0 & 0 \\ -751.82 & 12.546 & 3.1760 \end{bmatrix}$$

where the **B** matrices are scaled such that a unit perturbation to u_0 corresponds to a 1Hz perturbation in wingbeat frequency, and such that a unit perturbation to $\{\mathrm{u}_1, \dots, \mathrm{u}_4\}$ and $\{\mathrm{u}'_1, \dots, \mathrm{u}'_4\}$ correspond to a ±1 standard deviation perturbation (as measured from the kinematic dataset) in the directions specified by PCs 1-4 on each wing.

Both **A** matrices are described by systems that are asymptotically unstable in open-loop. Specifically, the longitudinal **A** matrix describes two damped monotonic modes ($\lambda_1 = -19.89$; $\lambda_2 = -2.28$) and one divergent oscillatory mode ($\lambda_{3,4} = 6.77 \pm 14.92i$) involving mainly pitching motion. The lateral **A** matrix describes one heavily-damped monotonic mode reflecting the damping provided by the so-called "flapping counter torque" ($\lambda_1 = -63.38$), one stable oscillatory mode ($\lambda_{2,3} = -20.16 \pm 21.72i$), and one divergent monotonic mode involving a rotationally-dominated combination of roll, yaw, and sideslip ($\lambda_4 = 15.51$). The unstable dynamics of the open-loop system are therefore rotationally dominated, which is relevant to the fuller dynamical analysis in Section 5 and to the accompanying tests of the tuning of various optical flow sensitive interneurons.

3 Computational Fluid Dynamics of *Calliphora* in Free Forward Flight (Yong Su Jung and Jim Baeder, University of Maryland; Sean Humbert, University of Colorado)

In this effort, a CFD solver (OVERTURNS) is used to calculate the forces and moments of a model *Calliphora* wing with prescribed flapping and deformation. OVERTURNS is a three-dimensional, high-fidelity Reynolds-Averaged Navier-Stokes equation solver developed at the University of Maryland, College Park (UMD). This solver has previously successfully used to simulate the flight of *Drosophila melanogaster* and other similarly-scaled flapping wing systems (MacFarlane *et al.*, 2011, Badrya et. al., 2017).

In this report, *Calliphora* kinematics that were extracted in free flight from previous experiments (Nagesh et al., 2019) were simulated and the effect of small changes in both states and control inputs on the produced forces and moments are investigated in order to derive estimates for the associated stability and control derivatives described previously in Section 2. Using small perturbation analysis, the nonlinear system is reduced to the following form,

$$\dot{\boldsymbol{x}}(t) = \mathbf{A}\boldsymbol{x}(t) + \mathbf{B}\boldsymbol{u}(t),$$

where **A** is the stability matrix, **B** is the control matrix, and $\boldsymbol{x}(t)$ and $\boldsymbol{u}(t)$ are the vectors of animal states and control inputs, respectively. Insect x, y, and z direction forces and moments in the insect body frame are given by X, Y, Z and L, M, N, respectively.

Using *Calliphora* wing CFD simulations, the following stability derivatives were computed using multiple results from small perturbations in vehicle states for the **A**-matrix:

- $(X_u, X_v, X_w, X_p, X_q, X_r)$, $(Z_u, Z_v, Z_w, Z_p, Z_q, Z_r)$ for longitudinal forces
- $(M_u, M_v, M_w, M_p, M_q, M_r)$ for longitudinal moments
- $(Y_u, Y_v, Y_w, Y_p, Y_q, Y_r)$ for lateral forces
- $(L_u, L_v, L_w, L_p, L_q, L_r)$, $(N_u, N_v, N_w, N_p, N_q, N_r)$ for lateral moments

For the **B**-matrix, the following stability derivatives were computed from perturbations in the asscociated control input vector. Here, the first 4 principal components (PCs) were used (Section 2), which were defined for the three-dimensional positions of the wing kinematics in the previous study (Nagesh et al., 2019). The other control input state is the wing beat frequency (wbf).

- (X_{PC}, X_{wbf}), (Z_{PC}, Z_{wbf}) for longitudinal forces
- (M_{PC}, M_{wbf}) for longitudinal direction moments
- (Y_{PC}, Y_{wbf}) for lateral forces
- (L_{PC}, L_{wbf}), (N_{PC}, N_{wbf}) for lateral moments

3.1 *Axis Systems*

In the inertial (or laboratory) coordinate system, the Z-axis is pointing vertically down, the X-axis is pointing forward, and the Y-axis is pointing to the right-side wing tip. The body frame is defined at the center of gravity of the insect. The wing coordinate system is located at the wing hinge, and it is aligned with the body coordinates when the wing is flat and level out the side, but as the wing moves, the wing coordinates will rotate with the wing. Therefore, the Y-axis will always remain along the span of the wing and X-axis will always pointing away from the leading edge of the wing and aligned with the chord.

A set of three wing angles determines the position of the wing any instant in time. The wing Euler angles are stroke angle (ϕ), deviation angle (θ), and pitch/twist angle (ω). The stroke and deviation angles are defined with respect to the body axes. Figure 12 shows the inertial, body and the wing axis systems with the stroke (ϕ) and deviation (θ) angle definitions. For clarity, the stroke angle defines the azimuth of the y_{wing} axis and the deviation angle defines the elevation of the y_{wing} axis. The wing pitch/twist angle is defined as rotation about the y_{wing} axis.

The positive stroke angle and deviation angle correspond to backward sweep and downward flap motion, respectively. Following sequence of rotation is used to give the current wing position from the body axis; the wing is twisted at each spanwise station first, then the wing is rotated by deviation angle and stroke angle in consecutive order, and finally the wing is rotated by body pitch angle.

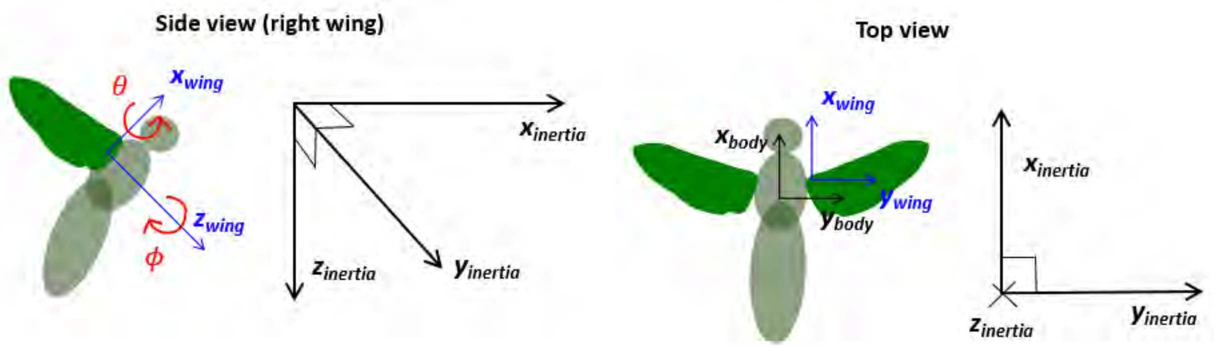

***Figure 12**. Inertial, body and wing axis systems.*

3.2 *Wing Kinematics*

The baseline wingbeat kinematic for free flight was obtained by averaging the data over 2708 wingbeats recorded in the previous study (Nagesh et al., 2019). The changes of the wing stroke and deviation angles and two wing twist parameters were shown in Figures 13 and 14. For clarity, the wing deflects upward and swept back at the start of the downstroke ($\psi = 0°$). The wing twist angle is defined as below at each spanwise station.

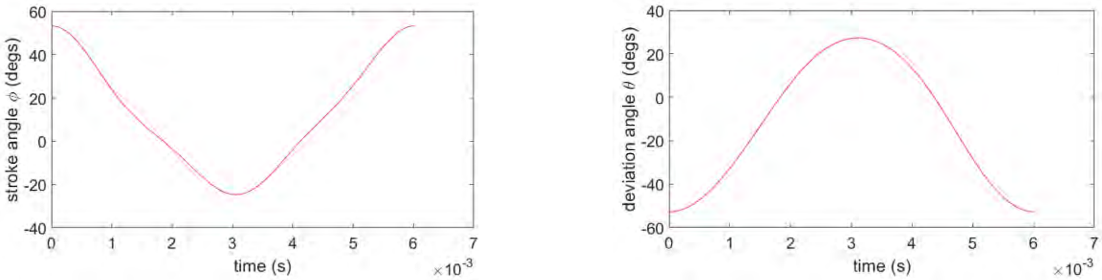

(a) Wing stroke angle (ϕ)

(b) Wing deviation angle (θ)

Figure 13. *Time history of wing kinematic history during a wingbeat cycle*

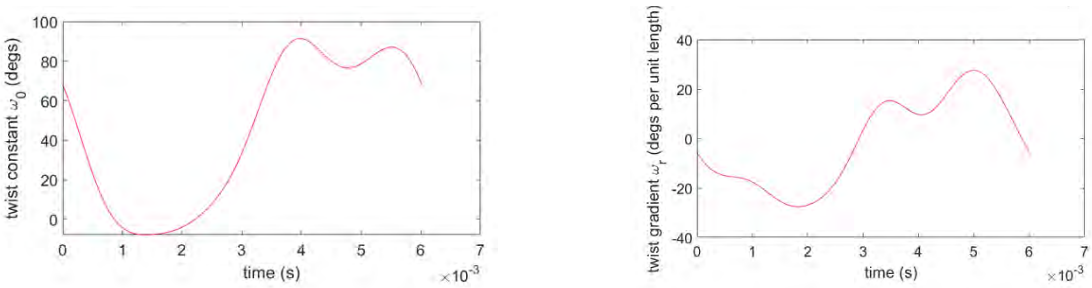

(a) Wing twist angle at the root (ω_0)

(b) Wing twist gradient (ω_r)

Figure 14. *Time history of wing twist history during a wingbeat cycle*

Figure 15 shows the snapshot of the motion of *Calliphora* wing by looking at right side (a) and top (b) of the insects. Here, the axis is the inertial coordinate system. The wing motion is captured at every 20° azimuth angle during a wing beat cycle. First, the stroke plane tilted in the forward after applying the body pitch angle, which provides thrust in both forward and upward directions.

3.3 *Simulation Setup*

For the forward flight simulations, freestream Mach number was set as 0.00249 which corresponds to 0.8509 m/s. Reynolds number of 1,746 was used, which was calculated based on the maximum resultant velocity at mid-stroke and mean chord length. Note that the wing beat frequency is 166.188 Hz. For the low Reynolds numbers ($10^2 \sim 10^3$), the boundary layer is assumed as pure laminar. 720 time steps per wing beat cycle was used ($\Delta t = 0.5°$), which allows reasonable computational time to simulate the deformed flapping wing. All simulations were conducted on the University of Maryland Deepthought 2 HPC cluster. Tables 4 and 5 summarize the current simulation inputs.

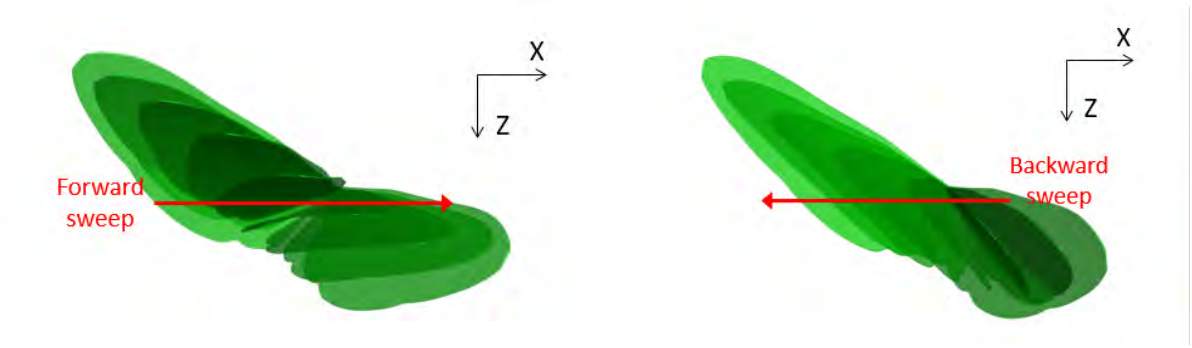

(a) Forward sweep (side)

(b) Backward sweep (side)

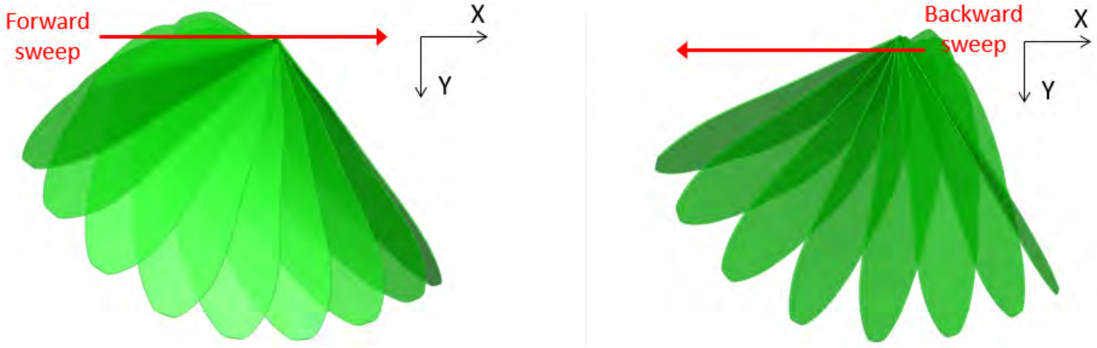

(c) Forward sweep (top)

(d) Backward sweep (top)

***Figure 15**. Snapshots of flapping wing for the CFD simulation in the inertia coordinates system.*

***Table 4**. Calliphora wing simulation parameters*

Freestream velocity	0.8509 m/s
Flight path elevation angle	-4.01° (ascending)
Body pitch angle	34.375°
Resultant body pitch angle	30.365°
Wing beat frequency	166.188 Hz
Wing span	10.1781 mm
Mean chord	2.714 mm
Wing Aspect ratio	3.75
Reynolds number	1,746

Table 5*. OVERTURNS simulation inputs*

Number of grid domains	2
Total time steps	2,880 (720 steps per cycle)
Flow condition	Laminar
Newton sub-iterations	12
Spatial reconstruction	5th order WENO scheme
Temporal scheme	2nd order backward difference (BDF2)
Low-Mach precondition	Yes
Number of processors	16 (4: wing and 12: background)

In the current simulation, a single wing was simulated without the insect body. An overset grid system was used for a body-fitted wing mesh and a Cartesian background mesh as shown in Figure 16. The initial wall normal spacing of the wing mesh was 1×10^{-5} chord. The detailed grid system used in the simulation is shown in Table 6.

Table 6*. Overset grid system, total mesh point 11.1 Million points*

	Type	Dimensions	Total node points
Wing	O-O structured	195x201x76	2.98 million
Background	Cartesian	226x233x156	8.21 million

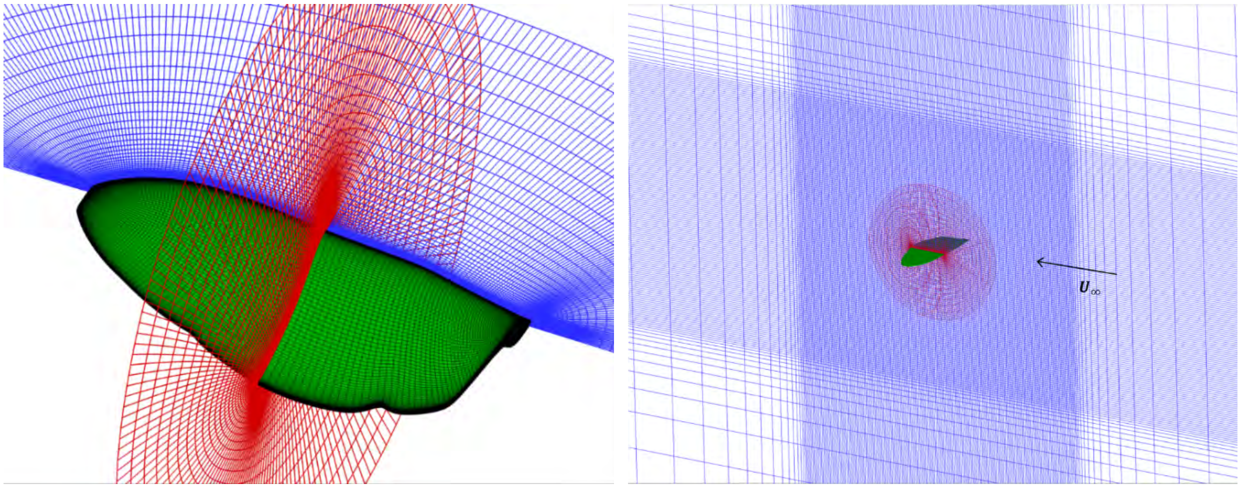

Figure 16*. Overset grid system used in OVERTURNS (Left: near-body, right: off-body)*

3.4 *Simulation Results*

3.4.1 Baseline motion for the wings-level equilibrium flight condition

Figures 17 and 18 show the X and Z forces and L and M moments histories during a wing beat cycle in the body axis system. The time-averaged forces and moments are reasonably converged after the 3rd wing beat cycle. Thus, for the stability analysis, the mean wing forces and moments were computed using data during 3rd and 4th wing beat cycles. As a result, the lift and thrust forces from the two wings are 0.567 mN and 0.0362 mN, respectively. Considering the Insect mass of 61.44 mg ± 14.11 (~0.6 mN), the insect's net body acceleration was 0.8 m/s^2. With the small acceleration, the current assumption of level equilibrium flight condition is reasonable.

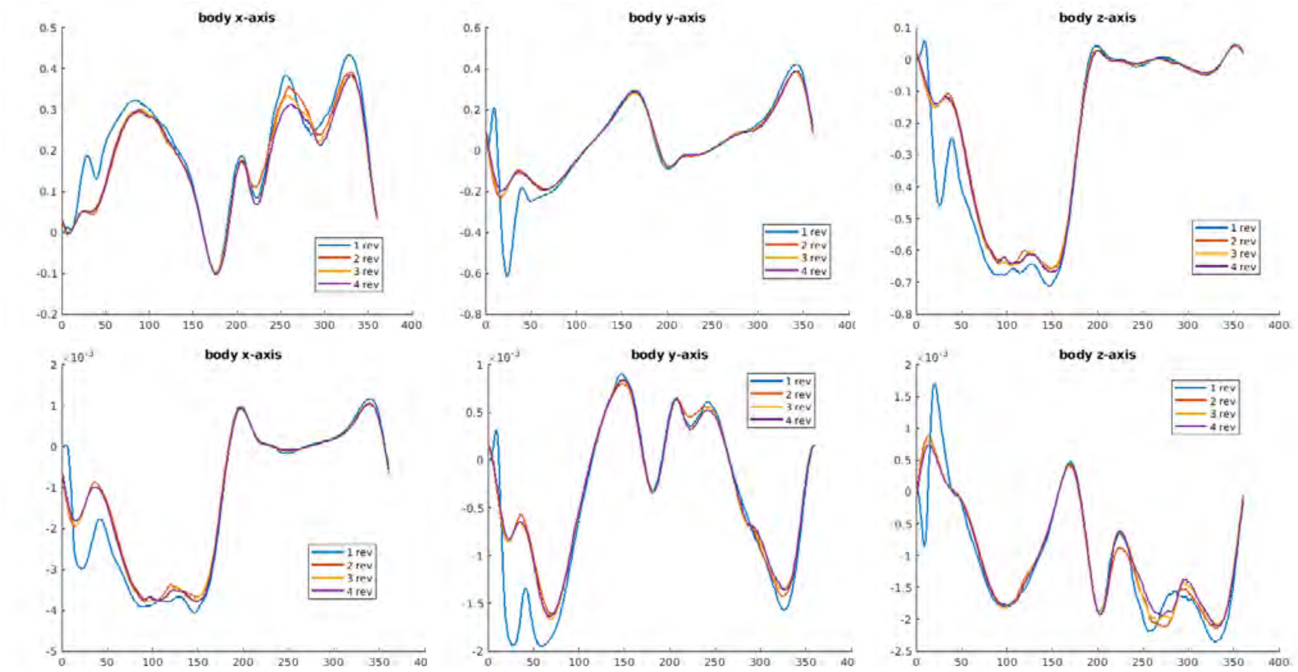

***Figure 18**. $L, M,$ and N body axis moments history (units: N-m×1000)*

Figure 19 shows the instantaneous wing wake structures using iso-Q Criterion surfaces at two different phases of the stroke; start of downstroke and upstroke. Current simulation was able to capture the root and tip vortices behind the wing.

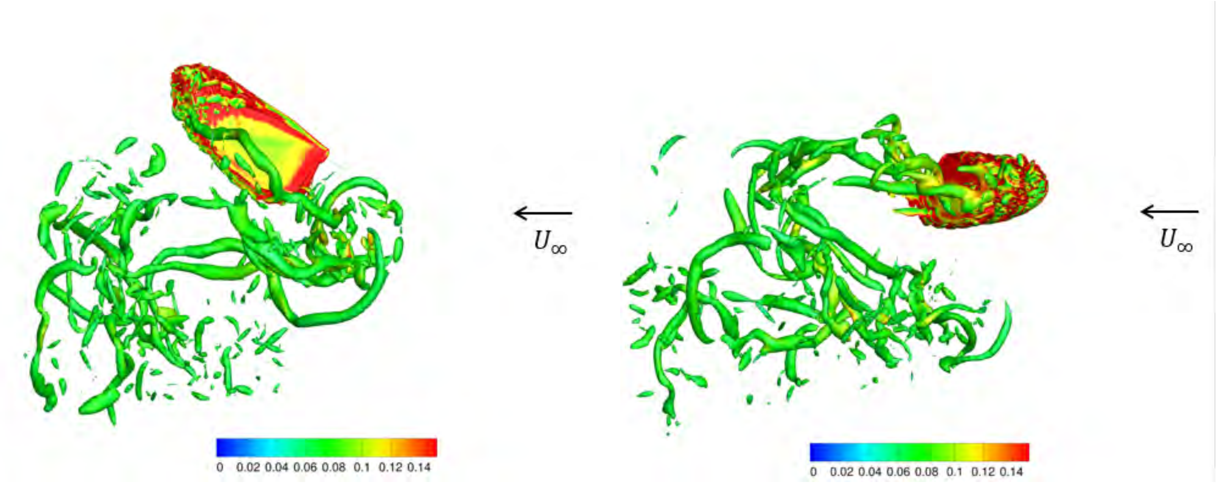

(a) Start of down-stroke (b) Start of up-stroke

Figure 19. *Wing wake visualization using iso-Q Criterion surfaces (0.001) and colored by vorticity*

3.4.2 **A**-*matrix results for longitudinal perturbations*

The derivation of longitudinal forces (X_u, X_w, X_q and Z_u, Z_w, Z_q) and moments (M_u, M_w, M_q) and lateral forces (Y_u, Y_w, Y_q), moments (L_u, L_w, L_q and N_u, N_w, N_q) will be presented in this section. The unit of the forces are [N] and the moments are [N-m]×1000. It should be noted that the resultant forces and moments were computed from a single right wing at the body axis. Results along with linear approximations (stability derivatives) are shown in Figures 20-25.

The perturbations are applied according to

- **Sweep of forward velocity (u) and vertical velocity (ω)** with increase/decrease of -20 %, -10 %, 10 %, and 20 % of freestream velocity
- **Sweep of pitch rate (q)** with increase/decrease of -5 %, -2.5 %, 2.5 %, and 5 % of wing beat frequency

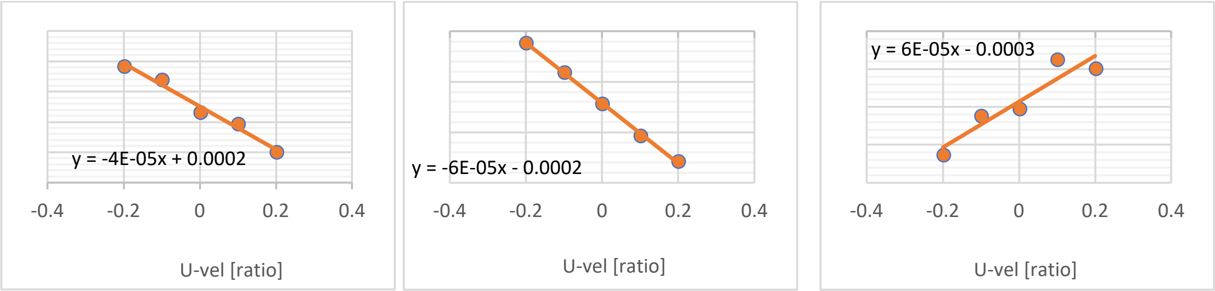

Figure 20. *Sweep of forward velocity, u (from left to right: X, Z, and M)*

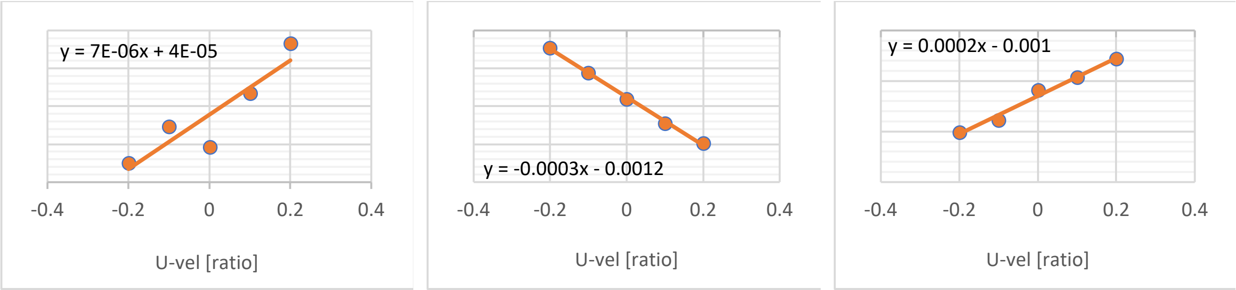

Figure 21. *Sweep of forward velocity, u (from left to right: Y, L, and N)*

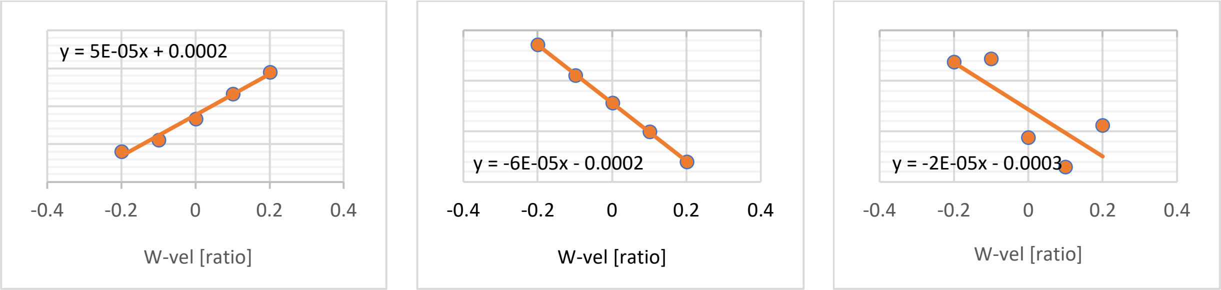

Figure 22. *Sweep of vertical velocity, w, (from left to right: X, Z, and M)*

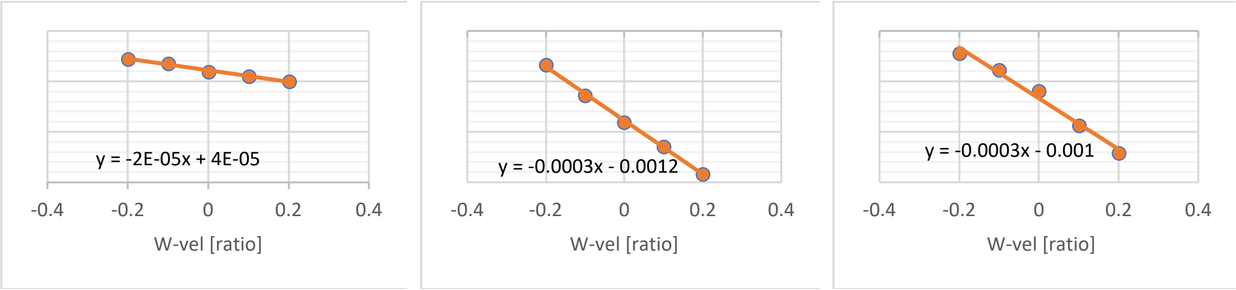

Figure 23. *Sweep of vertical velocity, w, (from left to right: Y, L, and N)*

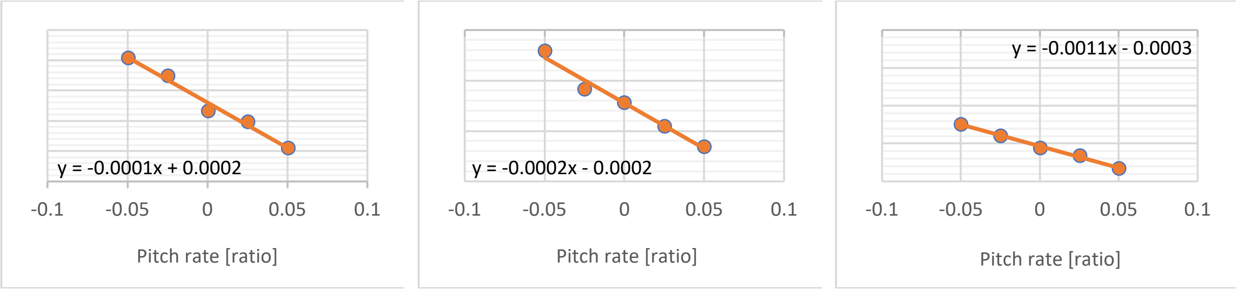

Figure 24. *Sweep of pitch rate, q (from left to right: X, Z, and M)*

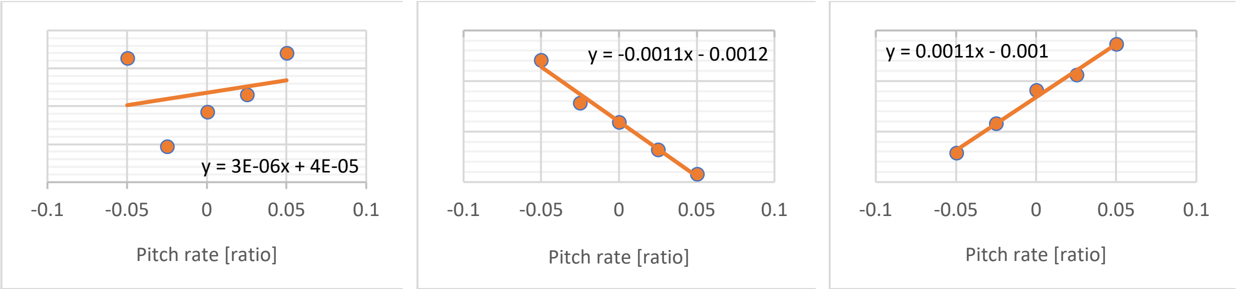

Figure 25. *Sweep of pitch rate, q (from left to right: Y, L, and N)*

3.4.3 **A**-*matrix results for lateral perturbations*

The derivation of longitudinal forces (X_v, X_p, X_r and Z_v, Z_p, Z_r), moments (M_v, M_p, M_r) and lateral forces (Y_v, Y_p, Y_r), moments (L_v, L_p, L_r and N_v, N_p, N_r) will be discussed in this section. Results along with linear approximations (stability derivatives) are shown in Figures 26-31.

The perturbations are applied according to

- **Sweep of sideslip velocity (v)** with increase/decrease of -20 %, -10 %, 10 %, and 20 % of freestream velocity
- **Sweep of roll rate (p)** with increase/decrease of -5 %, -2.5 %, 2.5 %, and 5 % of wing beat frequency
- **Sweep of yaw rate (r)** with increase/decrease of -5 %, -2.5 %, 2.5 %, and 4 % of wing beat frequency

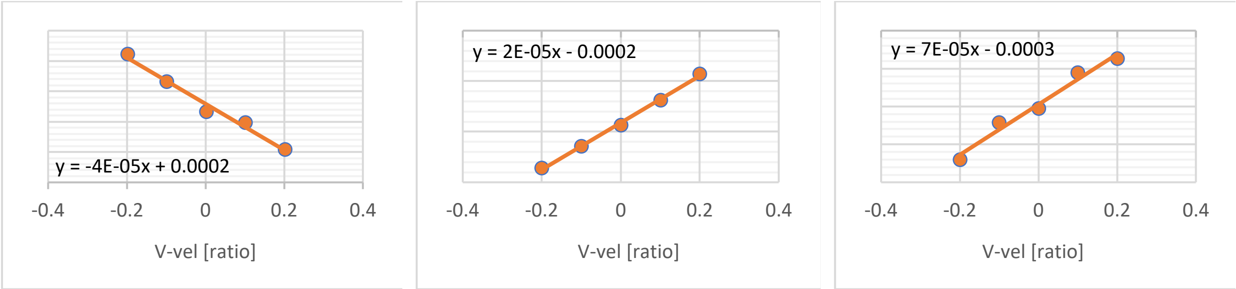

Figure 26. *Sweep of sideslip velocity, v, (from left to right: X, Z, and M)*

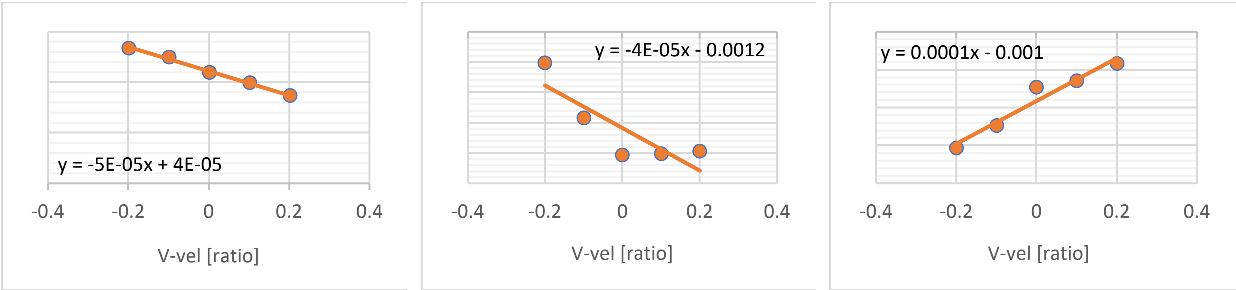

Figure 27. *Sweep of sideslip velocity, v, (from left to right: Y, L, and N)*

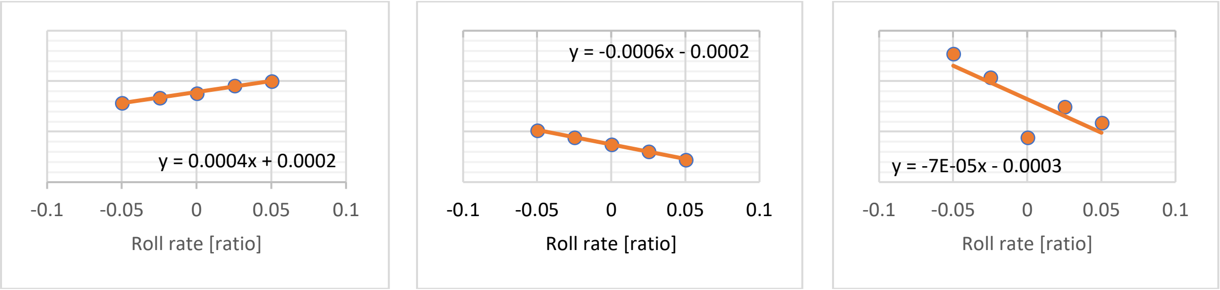

Figure 28. *Sweep of roll rate, p, (from left to right: X, Z, and M)*

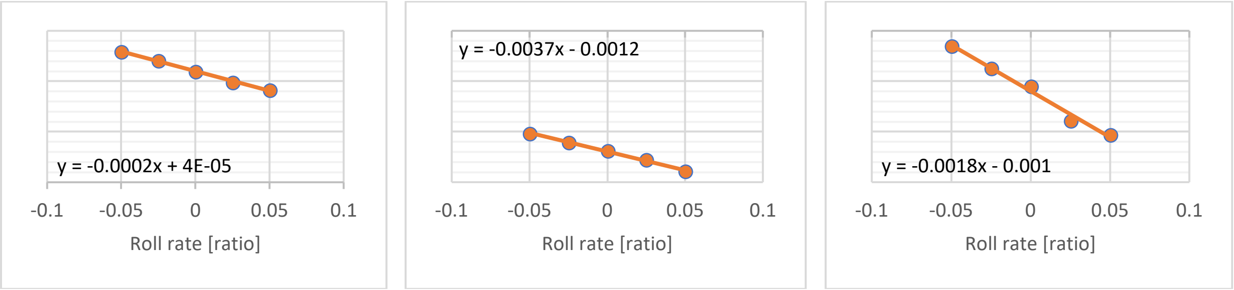

Figure 29. *Sweep of roll rate, p, (from left to right: Y, L, and N)*

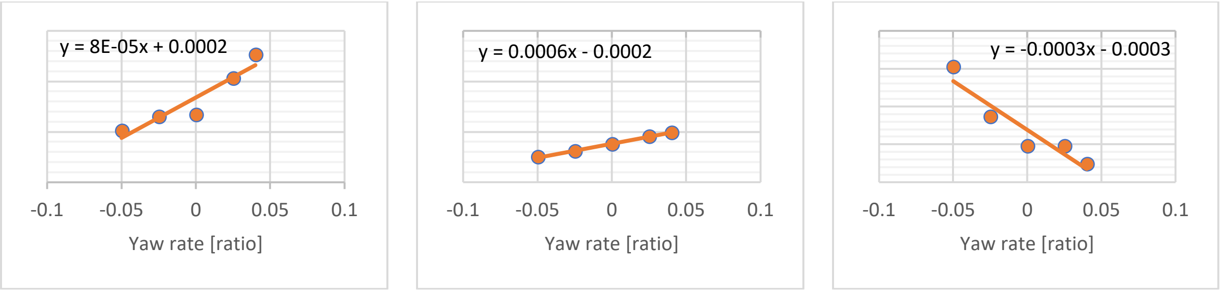

Figure 30. *Sweep of yaw rate, r, (from left to right: X, Z, and M)*

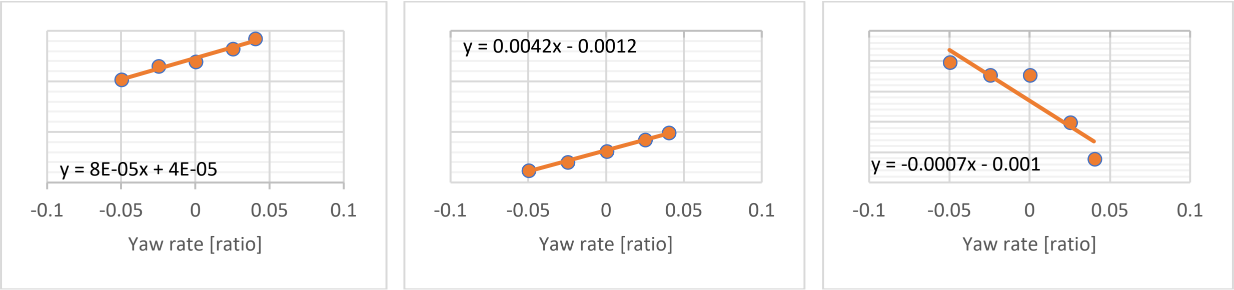

Figure 31. *Sweep of yaw rate, r, (from left to right: Y, L, and N)*

3.4.4 **B**-*matrix results – longitudinal and lateral cases*

The derivation of longitudinal forces (X_{PC}, X_{wbf} and Z_{PC}, Z_{wbf}), moments (M_{PC}, M_{wbf}) and lateral forces (Y_{PC}, Y_{wbf}), moments (L_{PC}, L_{wbf} and N_{PC}, N_{wbf}) will be discussed in this section. Results along with linear approximations (control derivatives) are shown in Figures 32-41.

The perturbations are applied according to

- **Sweep of principal components (*PCs*),** with increase/decrease of -1, -0.5, 0.5, and 1 of the standard deviation
- **Sweep of wing beat frequency (*wbf*),** with increase/decrease of -5 Hz, -2.5 Hz, 2.5 Hz, and 5 Hz from the base wing beat frequency

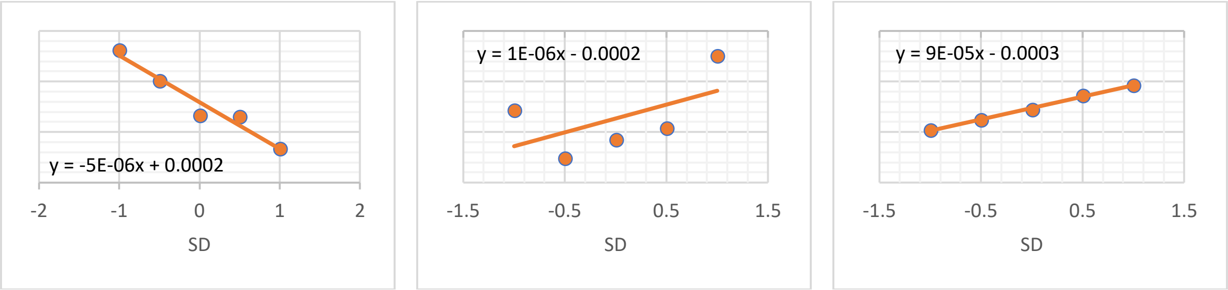

Figure 32. *Sweep of principal component 1, $PC1$ (from left to right: X, Z, and M)*

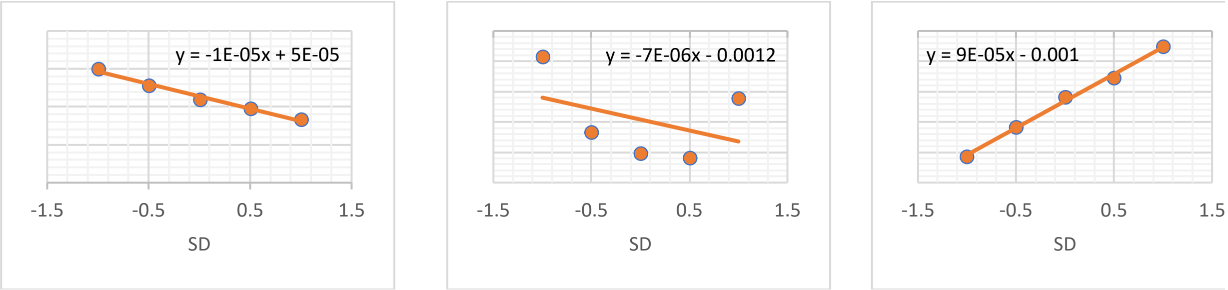

Figure 33. *Sweep of principal component 1, $PC1$ (from left to right: Y, L, and N)*

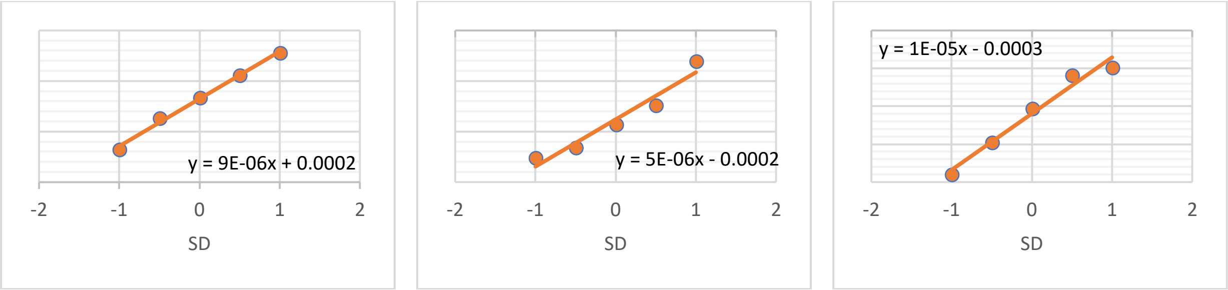

Figure 34. *Sweep of principal component 2, PC2 (from left to right: X, Z, and M)*

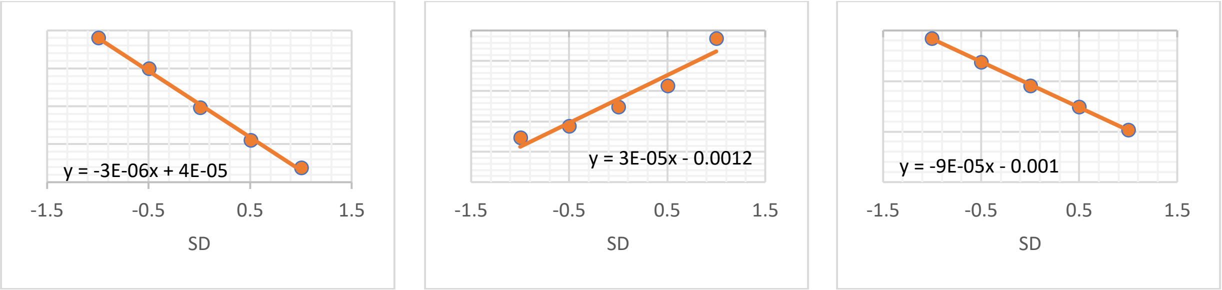

Figure 35. *Sweep of principal component 2, PC2 (from left to right: Y, L, and N)*

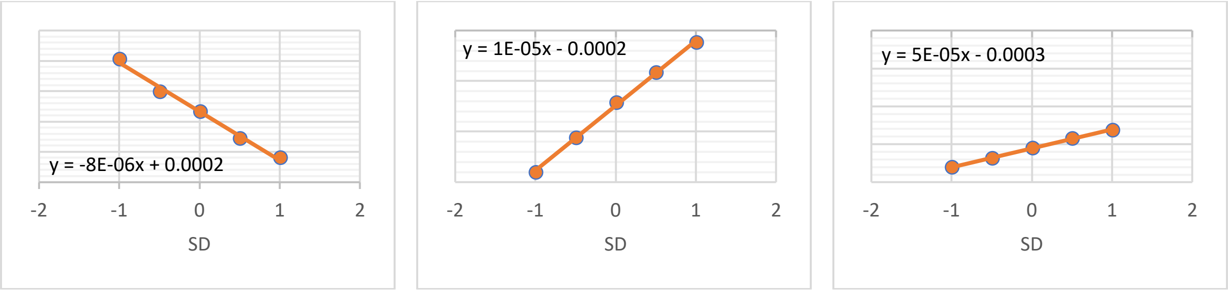

Figure 36. *Sweep of principal component 3, PC3 (from left to right: X, Z, and M)*

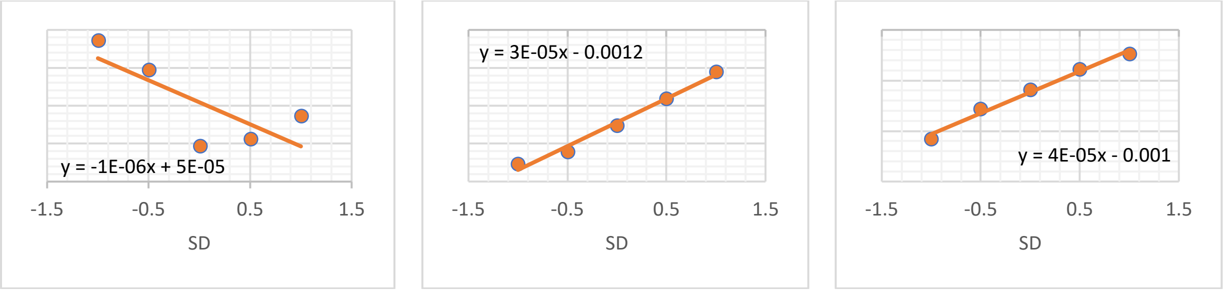

Figure 37. *Sweep of principal component 3, PC3 (from left to right: Y, L, and N)*

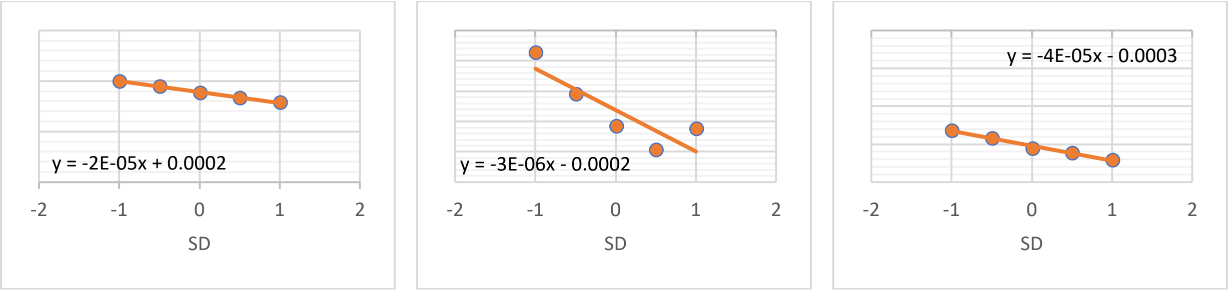

Figure 38. *Sweep of principal component 4, PC4 (from left to right: X, Z, and M)*

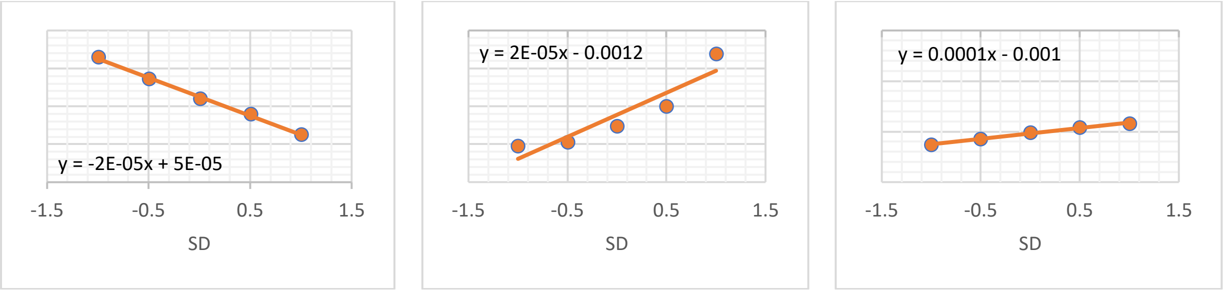

Figure 39. *Sweep of principal component 4, PC4 (from left to right: Y, L, and N)*

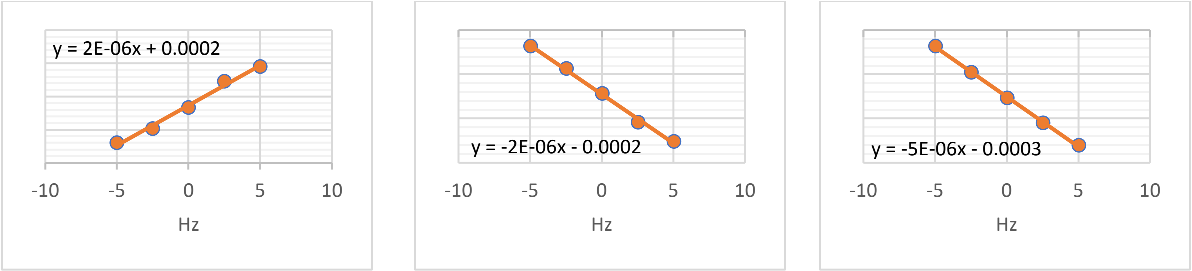

Figure 40. *Sweep of wing beat frequency (from left to right: X, Z, and M)*

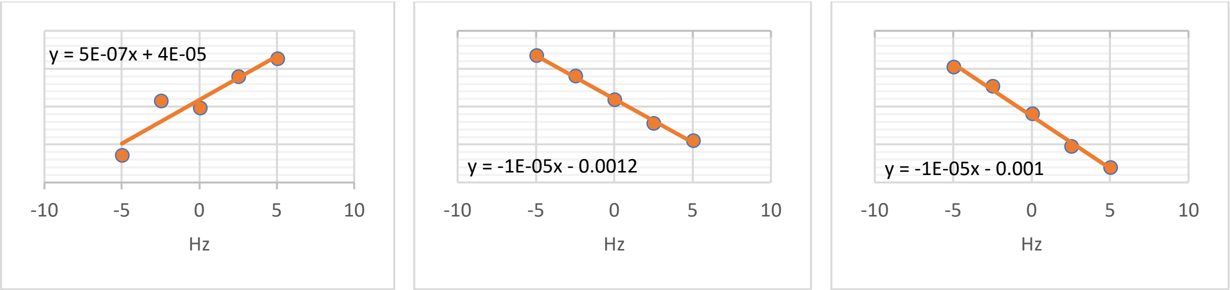

Figure 41. *Sweep of wing beat frequency (from left to right: Y, L, and N)*

4 Neuronal Basis of Visual State Estimate Across Dipteran Species (Jiaqi Huang and Holger Krapp, Imperial College London)

During the last reporting period we have further increased the experimental data base on the receptive field organization of spiking heterolateral Lobula Plate Tangential Cells (LPTCs) and developed refinements of (a) the experimental setup, (b) the spike sorting to extract the activity of individual cell-types even if the Signal-To-Noise ratio (SNR) during the recordings was low and (c) circular/spherical statistical tests to quantify potential differences in the preferred self-motion components for a given species, sex and cell-type.

4.1 Background

As outlined in our previous reports we have started over the last 2 years to accumulate a substantial data base on the local response properties of spiking heterolateral LPTCs in several different species. The reason for this departure from our original plan to characterize the output LPTCs in larger hoverflies such as *Eristalis tenax* or *Eristalis pertinax* – species for which the flight dynamics are available (e.g. Sun et al. 2007; Zhu et al. 2020) – was the poor availability of these seasonal species.

4.1.1 Visual state estimation based on optic flow

Reiterating the significance of spiking LPTCs, these cells pay a cardinal role in the unambiguous distinction between specific translation- and rotation-induced optic flow fields. The principle limits of methods that retrieve self-motion components from optic flow fields are well explained by the formal treatment provided by Koenderink and van Doorn (1987). Their iterative algorithm, now known as *KvD*, enables to obtain the translation direction, $\boldsymbol{T}$, rotation axis, $\boldsymbol{R}$, and reduced distances, μ_i, of a modelled optic flow field that comes closest to a measured optic flow field in the least square sense. Figure 42 provides the receptive field organization of a spiking V1-cell recorded in the Lobula Plate of the blowfly *Calliphora*, and the major iteration equations proposed by Koenderink and van Doorn in a slightly modified version, to illustrate the fundamental importance of spiking LPTCs.

The receptive field of the V1-cell in *Calliphora* is one of the few examples where a single LPTC has a receptive field that comprises both visual hemisphere and is thus ideally suited to estimate a specific self-rotation component. Most other heterolateral LPTCs have only monocular receptive fields, which are complemented by the receptive field of their contralateral target cells. There is some experimental evidence that the connectivity scheme heterolateral LPTCs establish with outputs cells of the lobula plate such as the HS- and VS-cells, is specifically chosen to improve rotation-specificity (Krapp 1995). Indirect support comes from studies on the neck motor system in *Calliphora,* indeed showing a higher degree of rotation specificity reflected by binocular receptive fields of neck motor neurons (Huston and Krapp 2008).

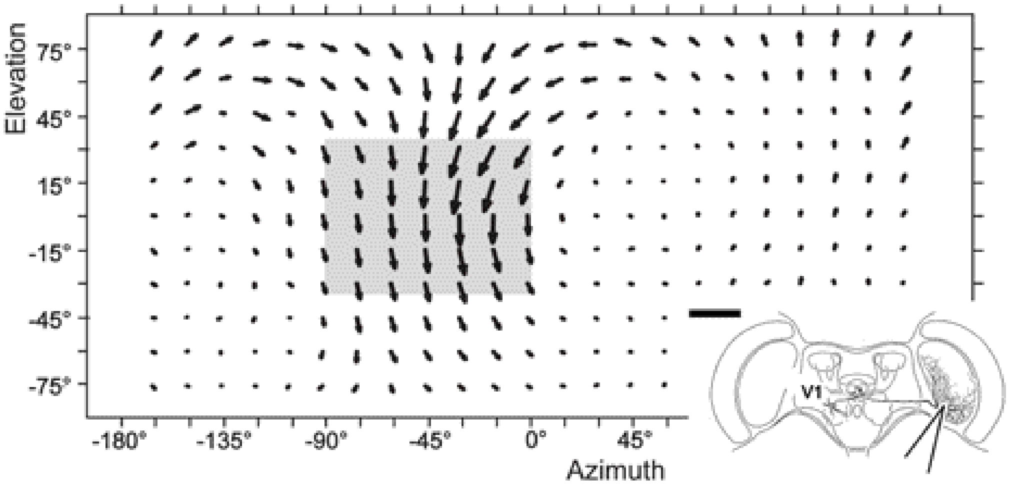

$$\boldsymbol{R} = (\boldsymbol{I}-\boldsymbol{M})^{-1} [(\boldsymbol{T} \times \langle \boldsymbol{d}_i \rangle) + \langle \boldsymbol{p}_i \times \boldsymbol{d}_i \rangle]; \qquad \boldsymbol{T} = -(\boldsymbol{I}-\boldsymbol{M})^{-1} [(\boldsymbol{R} \times \langle \boldsymbol{d}_i \rangle) + \langle \boldsymbol{p}_i \rangle]$$

Figure 42: *Receptive field organization of the heterolateral V1-cell in the* Calliphora *lobula plate. Local preferred directions (LPD) and motion sensitivities (LMS) are given by the orientation and length of individual vectors plotted again azimuth and elevation of the 4π visual field of the insect. (Figure taken from Krapp et al. 2001; reconstruction: K Hausen). To determine the preferred translation, **T**, and rotation, **R**, parameters, i.e. the fly's self-motion components the V1-cell would respond best to, LPDs and LMSs define local parallax vectors* $\boldsymbol{p}_i$ *at directions* $\boldsymbol{d}_i$ *within the visual field. To simplify the iteration procedure, the distance distribution in the visual world has been assumed to be uniform – which is unrealistic, but reflects the situation during the experiment where visual stimuli to obtain local motion responses were presented at the same distance at all stimulus positions. **I** and **M** are the 3 x 3 Identity- and weight-Matrix, respectively, and pointed brackets indicate averages over all values. As can be seen from the middle terms on the right hand side of both iteration equations, the translation estimate, **T**, also depends on rotation, **R**, and vice versa. The resulting 'apparent' terms limit the accuracy at which the preferred self-motion components can be estimated. There are two solutions to the problem: (i) the apparent terms are cancelled by subtracting the signals of other LPTCs estimating rotation and translation independently, or (ii) the cells have a receptive field that included nearly the entire visual field. In the latter case the sum of the direction vectors* $\langle \boldsymbol{d}_i \rangle$ *would become zero and the apparent terms vanish, enabling an unambiguous retrieval of the self-motion components. Figure from Krapp et al. 2001.*

4.1.2 Connectivity scheme between matched filters for optic flow in the left and right lobula plate

A couple of questions have not yet been addressed in the past: what is the connectivity scheme between heterolateral LPTCs and their target cells? About 50-60 LPTCs have been anatomically described (Hausen 1993) and many were studied in terms of their response properties to visual motion. In the context of the mode sensing hypothesis, we can limit our consideration to a specific subpopulation of 10 VS-cells (Hengstenberg 1982), the receptive fields of which have been characterized in great detail in the blowfly *Calliphora* (e.g. Krapp et al. 1998). These cells were proposed to establish a non-linear high-dimensional coordinate system for the detection of horizontal body rotations resulting in deviations from the animals default attitude (Taylor and Krapp 2007). Based on the distribution of the cells' local preferred directions and motion sensitivities, there are different ways in which the signals of the 10 VS cells in left and right lobula plate of the fly's brain could be combined to increase their specificity to indicate attitude change. To sense nose up pitch rotations, for instance, the output signal of the left VS1-cell could be combined with the inverted output of the right VS10-cell ($VS1_l - VS10_r$). Combining cells with reciprocal numbering this way, i.e. $VS1_l - VS10_r$, $VS2_l - VS9_r$, … , $VS10_l - VS1_r$, would automatically create sensors for rotations around body axes that are gradually changing their azimuthal positions to cover an overall range that includes nose up pitch, an intermediate between pitch and roll, pure roll, again an intermediate rotation in the opposite direction and finally nose down pitch.

Another way to combine the signals of VS-cells either side in the fly brain would be to either add the output for cells with equal numbering or to use the difference. Depending on the sign of the output signals that are combined, the pairs of cells would display different self-motion preferences (see legend Figure 43).

The former connectivity scheme would certainly retain the fine-grained resolution of horizontal body rotations, but implies that for each of the 10 VS-cell there should be a heterolateral LPTC that conveys its signals to the corresponding neuron in the contralateral lobula plate. The latter way, i.e. to use sums and differences between corresponding cells in either side of the brain is a probably a simplification, but is partially supported by experimental findings. The question still remains what is known about cells sending directional motion information across the midline and how do they connect to the VS-cells in the opposite lobula plate?

Electrophysiological studies in *Calliphora* of another group (Haag and Borst 2004; Haag and Borst 2007; Borst and Weber 2011) and our recent work on heterolateral LPTCs across species suggests, however, that there are only 3 major types of spiking neurons that are sensitive to vertical motion and connect the left with the right lobula plate: V1-cells, V2-cells and Vx, cells (see below. Note that the Borst Lab has reintroduced the Vx-cell as Vi-cell). Apparently, for an unambiguous estimate of the rotations around horizontal body axes the fine-grained resolution represented by the preferred rotation axes of the VS-cells requires only a much cruder spatial resolution at the level of the heterolateral LPTCs to increase the cells' specificity. Interestingly, axes represented by the spiking LPTCs include the roll axis (V2-cell), the intermediate axis between roll and pitch at roughly 120 deg azimuth (V1-cell) and a complementary rotation axis at about 60 deg azimuth (Vx-cell).

Surprisingly, the actual connectivity of the spiking LPTCs has not yet been established by means of intracellular double recordings where current injections into one cell has a clear cut effect of its postsynaptic target. However, the Borst lab successfully establish ipsilateral connections for the Vx-cell (Vi-cell): the Vx-cell is electrically coupled to a group of distal VS-cells (VS7-VS10) and inhibits the ipsilateral VS1-cell (Haag and Borst 2007). This combination sets up a nose down pitch sensor purely based on ipsilateral visual input. Although circumstantial evidence suggest the Vx-cell to connect to contralateral VS-cell, those projections have not been established in electrophysiological double recordings. A similar situation applies to the V2-cell, which is an exception in the sense that it responds most strongly to vertical upward – as opposed to downward – motion in the lateral visual field. Recordings from this cell clearly suggest that it is projecting to the contralateral VS-cells, but again an electrophysiological proof is still missing. From the know receptive field organization of the V2-cell (see below) however, it is obvious that together with the contralateral VS6-cell it would form a perfect roll sensor, even without inverting its output signal: (VS6 + V2 = roll). Finally, the input organization of the V1-cell has been known for a while – it is electrically coupled to VS1-3 – but it is less well established which contralateral VS-cells the V1 cell connects to. From its output arborisations the V1-cell is likely to target proximal VS-cells such as VS8-10 which would set up a sensor for a slightly off axis nose up pitch rotation.

A summary of the likely connectivity based on, electrophysiological and anatomical evidence is shown in Figure 43. It summarizes results from the Borst lab (Haag and Borst 2007; Borst and Weber 2011) as well as results from our own lab.

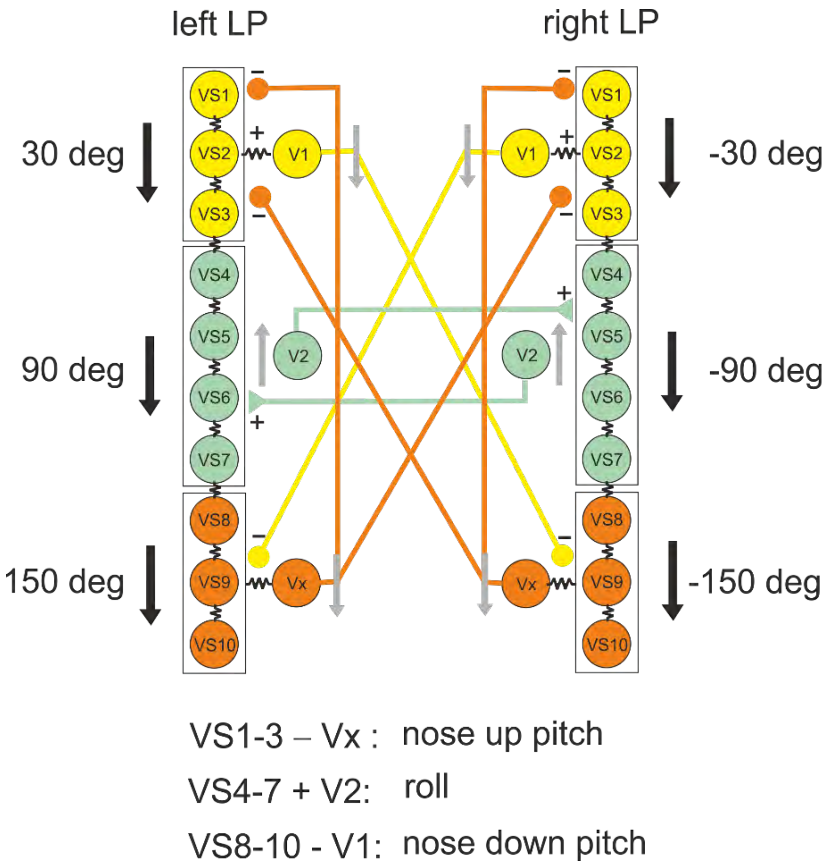

***Figure 43**: Hypothetical connectivity scheme between VS-cells and spiking LPTCs based on physiological and anatomical evidence. Contralateral connections have not yet been established in terms of electrophysiological double recordings. Ipsilateral connections are mediated by gap junctions (electrical synapses = resistance symbols) and inhibitory chemical synapses (round symbol). Excitatory synapses are given as triangles. VS-cells can be clustered roughly into three groups: VS1-3 (yellow) with average maximum sensitivity to downward motion at ~ 30 deg azimuth. VS4-7 (green) with average maximum sensitivity to downward motion at ~ 90 deg azimuth. VS8-10 (orange) with average maximum sensitivity to downward motion at ~ 150 deg azimuth. Note that the sensitivity to downward motion of individual cells may differ from these average values. Sums and differences of VS-cell outputs from either brain hemisphere would result in the following selectivities: VS1-3(l) + VS1-3(r) => nose up pitch; VS1-3(l) – VS1-3(r) => mostly cancel ; VS4-7(l) + VS4-7(r) => + lift; VS4-7(l) – VS4-7(r) => roll; VS8-10(l) + VS8-10(r) => nose down pitch; VS8-10(l) – VS8-10(r) => mostly cancel.*

4.1.3 Distribution of preferred self-motion parameters in species other than Calliphora

Over the last couple of decades, in *Calliphora* a number of heterolateral LPTCs have been characterized with respect to their matched filter properties to sense specific self-motion components (Krapp et al. 2001; Longden et al. 2017). We have reported the results of more recent studies on commonly recorded spiking LPTCs in our last year's report, which included data from male and female flies. Altogether, *Calliphora* still is the species where the highest number of

LPTCs, both spiking and output neurons, has been investigated and is therefore considered the ‘gold standard’ in terms optic flow specificity.

A relevant question in connection with the Mode Sensing Hypothesis is: Are the preferred rotation axes of the most common spiking LPTCs in *Calliphora* the result of a species-specific adaptation? Or do they reflect a general functional principle that applies across dipteran species?

To address these questions we have started a broad comparative study that investigates spiking LPTCs in several species and both male and female animals. During our studies we were also able to address another important question: does the sexual dimorphism – an increased extent and higher spatial resolution in the frontodorsal compound eye of males – present in some dipteran fly species (Land and Eckert 1985) differentially affect the receptive field organization of LPTCs in males and females?

By streamlining or methodologies and building highly efficient experimental rigs we were able to collect a significant amount of electrophysiological data from nine dipteran species and a hymenopteran wasp which we can compare to the results in our gold standard *Calliphora*.

In the following our methods are outlined in addition to changes of our data analysis and statistical test procedures.

4.2 Methods

In previous reports we already introduced a novel experimental setup for the effective characterization of receptive fields in spiking LPTCs. Until recently, common practice in our lab was to present a motion stimulus at different position within the animal’s visual field using a meridian frame apparatus while recording the neuronal activity of a given cell (Krapp and Hengstenberg 1997). When using the novel Goniometric Recording Platform (GRP) the stimulus screen is kept stationary and the fly is positioned in front of it, so that different parts of the animal’s eyes face the motion stimulus. This arrangement is perfect for extracellular recordings which are inherently more stable, but would not work for delicate intracellular recordings which easily become unstable when the slightest relative motion between the electrode tip and the recorded cell occurs. The required miniaturization of the AC-amplifier, fly holders and the use of particularly small micro-manipulators was informed by a hybrid Fly(brain)-Robotic Interface (Huang et al. 2019).

4.2.1 New Mini-GRP

Compared to the 1st generation GRP introduced in previous reports we now developed a new version that is smaller, portable, controlled by a laptop computer and can be powered from the mains or by a 24 Volt car battery (Figure 44). The latter power supply cuts out 50 Hz electrical noise from the mains. In combination with a laptop-connected electronic microscope (Figure 45), the system is fit for field work. Its operational dimensions are 21 (width) x 46 (depth) x 58 (height) cm. By separating the base stand, they may be reduced to 21 x 10 x 58 cm for transportation in a carry-on luggage item to any location abroad where species of interest can be observed and captured in the wild. The total weight of the mini-GRP is less than 3 kg. The system can be used at home which, during Covid-19 pandemic, is another advantage.

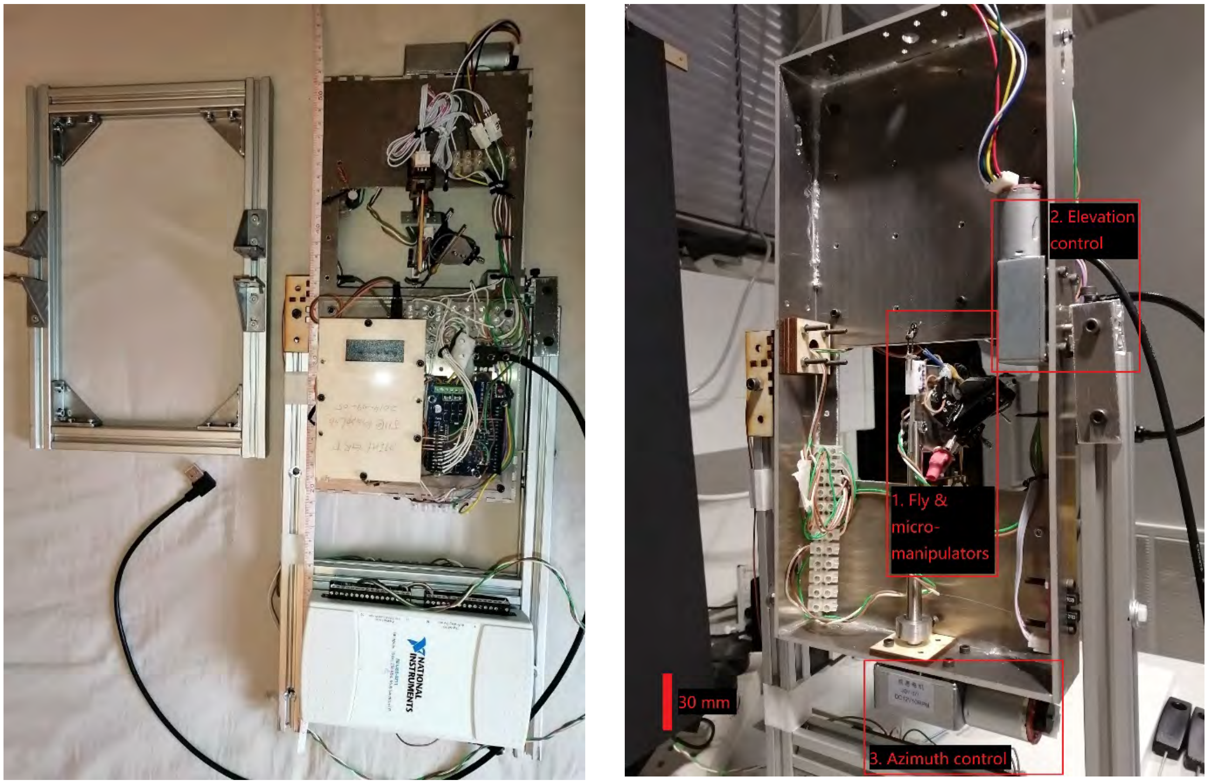

Figure 44: *New generation mini-Goniometric Recording Platform (GRP). Left: dissembled – aluminium frames are used to fix the electronics, motors and motor controls. Compared to the 1st generation, the new mini GRP has further reduced the recording time for measurement at 84 stimulus positions within the receptive field of a spiking LPTC by 20% from 30 down to 24 minutes thanks to PID-controlled motorization. Metal parts around the fly increase the electrical shielding. Right: assembled GRP.*

Recorded and amplified data are acquired using a USB NIDAQ run at 20 kHz sampling frequency. Flexible visual stimulation can be provided by either a Digital Light Projector (DLP) or an LCD monitor driven at a 240Hz framerate.

The firmware of the new mini GRP was designed to be compatible with the 1st version GRP, although the resolution of the angular position feedback was increased from 500 pulses/revolution to 6300 pulses/revolution. The experimental protocol in terms of the sequence of the stimulated positions was kept identical to the previous one. The same is true for scripts programmed in Python for data collection, data processing (spike sorting) and data presentation.

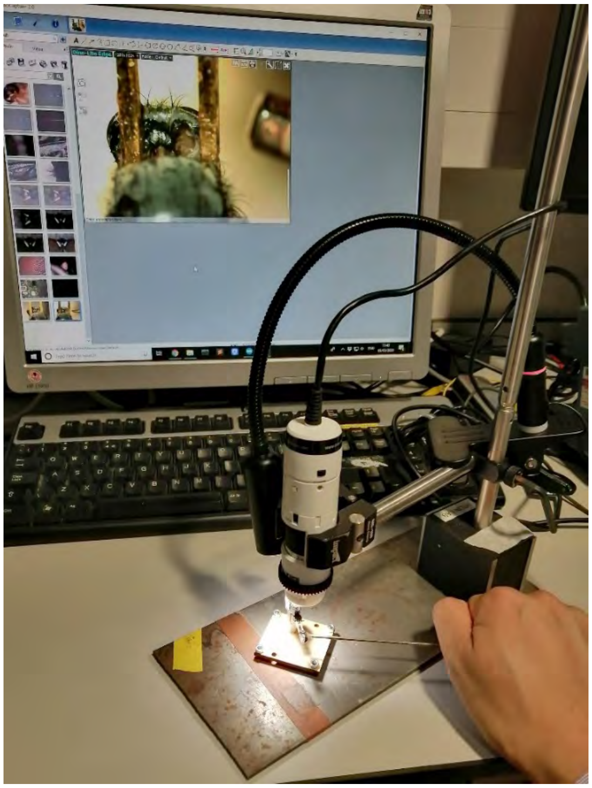

Figure 45: *Laptop-based electronic microscope. As the mini-GRP, the microscope is suitable for work in the field as it can be connected to a laptop PC. It provides sufficient optical magnification to perform a minimal dissection required to fix the animal to a dedicated holder and gain access to the rear head capsule for placing the recording electrodes.*

4.2.2 Animals, experimental protocol and primary data analysis

Experimental results presented in this report were obtained for two dipteran fly species, *Calliphora vicina* and *Hermetia illucens*. Earlier experiments were mostly performed on different hoverfly species, horseflies and blowflies. Blowflies were bred under standard conditions in our insect facility and Soldier flies were purchased from an animal supplier and kept in cages in the lab.

The dissections and electrode placements were mostly performed using a stereo microscope (Stemi 2000, Zeiss) or, in some cases, a portable 200 x USB microscope (DinoLite, Dunwell Tech, Inc., CA, USA) (Figure 45). Flies were waxed onto a 2-pin fly holder, where the symmetrical pseudo pupils (frontal eye equator) was used for aligning the head orientation with the spherical coordinate frame of the stimulus set up. Legs and proboscis were removed to reduce tissue movements caused by the muscle contractions. The open wounds were sealed with beeswax. The back of the head capsule was cut open and cuticle, muscles and fat tissues were removed to expose the lobula plate. A 3 Mohm tungsten electrode (UEWSHGSE3N1M, FHC Inc., Bowdoin, ME, USA) was inserted into the head capsule and positioned close to individual LPTCs, so that the SNR of the recorded voltage was > 2:1. Fly ringer solution was added from time to time to prevent desiccation.

A 240 Hz LED monitor was used as a visual stimulus device for the experiments. The screen was placed 30 cm in front of the insect. A black mask with a 125 mm diameter hole was covered on the screen, to reduce the angular size of the stimulus to less than 30 degrees, viewed from the insect.

As its predecessor, the mini-GRP rotated the fly through 84 sampling stimulus positions, where the local response properties, (preferred direction and motion sensitivities), of the LPTCs were studied. At each coordinate, 8 visual motion stimuli were displayed in 16 seconds, while the neural responses were recorded. Each stimulus took 1 second, with a stationary grey screen being presented for 0.25 seconds before and after the motion stimulus. The sequence motion stimuli consisted of square-wave visual gratings moving at constant speed in 8 different directions (0, 90, 180, 270, 45, 135, 225, 315 degrees). The temporal frequency of the stimulus was set to 3 Hz, at a Michelson contrast of near 100%, with lowest and highest light intensities of 0.36 and 360 cd/m^2, respectively. After sorting/detecting the spike of individual LPTCs (see below) the instantaneous spike rate was calculated and used to compute the local preferred direction (LPD) and local motion sensitivity (LMS). This was based on projecting the responses to the different directions of motion into local X- and Y- components and computing the mean angle (LPD) and its magnitude (LMS). The results were plotted as vectors into a cylindrical projection of the spherical visual field against azimuth and elevation of the respective stimulus position (Figure 49).

We tested the mini-GRP in an experiment where we recorded the activity of a directional-selective H1-cell in the lobula plate of the blowfly, *Calliphora vicina*. The quality of the recording in terms of stability and SNR was comparable with the 1st generation GRP. Figure 46 shows the original voltage trace of the recording as well as the time-continuous spike rate based on the interspike intervals.

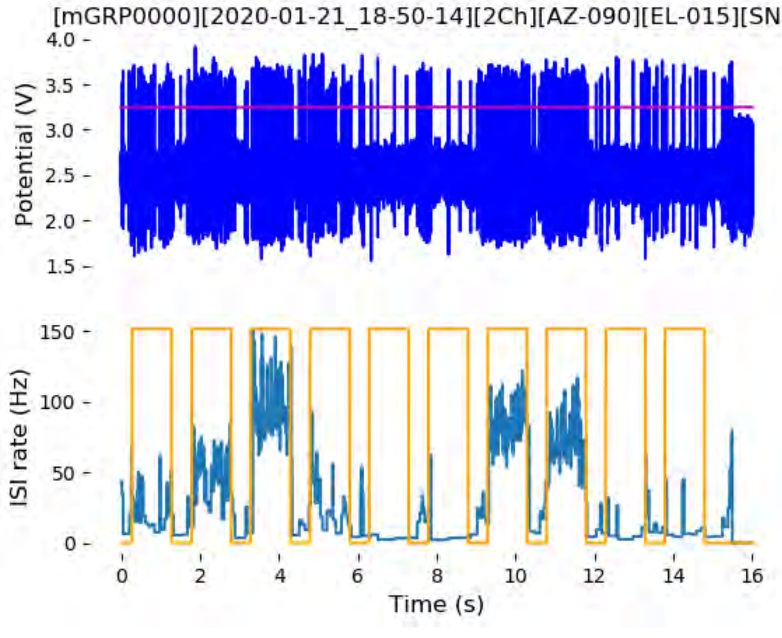

Figure 46: *Extracellular recording from a directional-selective H1-cell in the lobula plate of* Calliphora*. The SNR of the recording was high enough for the application of a simple threshold criterion to detect the cell's spikes (magenta line in upper plot). The bottom plot shows the instantaneous spike rate based on the inter spike intervals (ISI) as a function of time. Yellow square pulses indicate stimulus phases where a square wave grating was moving perpendicular to its orientation in different directions.*

4.2.3 Improved spike sorting

In most of our recordings the SNR was stable throughout the duration of the experiments. However, in some cases the insect started to pump its hemolymph and the recording quality started to degrade. This was probably the result of changes in the capacitive coupling between the hemolymph and the electrode which affected the SNR of the recordings and precluded the application of a simple threshold method for spike detection. To accommodate changes of the recording quality within a reasonable range, we developed an advanced spike sorting algorithm.

Instead of comparing peak spike amplitude to a fixed threshold value, we fitted a triangle to the rising and falling slopes of individual spikes to estimate its peak value. The reconstructed features of the spikes were combined into two parameters: (i) area of the fitted triangle and (ii) the mean of the slopes. A Gaussian Mixture Models (GMM) was then applied to extract the spike from the background noise (Figure 47).

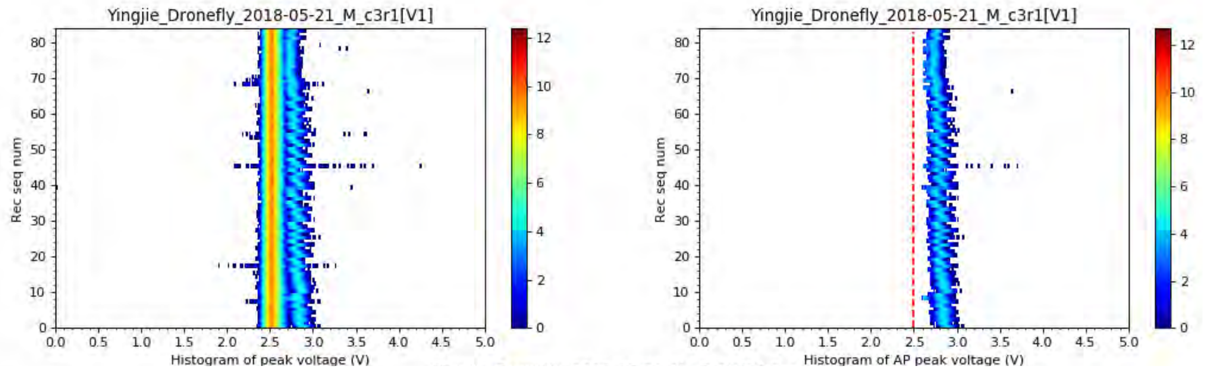

Figure 47: *Spike sorting with peak reconstruction and 2D Gaussian Mixture Models (GMM) classification. Left: the voltage peak distribution of the 84 raw recordings – sequence from bottom to top. Right: Voltage peak distribution of the sorted spikes. Note that the algorithm has background noise distribution which has been successfully removed.*

4.2.4 Analysing the preferred self-motion components using the KvD algorithm

We have described the iterative least square algorithm introduced by Koenderink and van Doorn (1987) in our previous report. In brief, the algorithm minimizes the squared error between a measured optic flow field (here the LPTC receptive field) and a modelled optic flow field that depends on the translation vector, ***T***, the rotation vector, ***R***, and the local reduced distance (nearness), μ_i (Figure 42). In case the distance distribution is isotropic and set to 1, the procedure allows us to retrieve the preferred translation and rotation vectors as well as the ratio at which they contribute to the observed optic flow field.

4.2.5 Statistical analysis

We have looked into spherical statistics as a tool for a quantitative comparison of local preferred rotation axes across, species, sexes and cell-types. The reason why this was necessary is explained below.

An isotropic (round) Fisher distribution in 3D is characterised similarly to a normal distribution in a 2D plane: it has a mean direction (analog to the mean, μ) and a concentration parameter (analog to the variance, σ). Figure 48 depicts a Fisher distribution on a sphere with concentration parameter of 50. At this value of concentration parameter, tests for equal means on a plane (Using angular values as arguments) give similar or even better results than tests on a sphere. Linear tests give better results as long as the true means are sufficiently far apart (> 10 degrees), but do worse when concentration parameters are relatively small < 15.

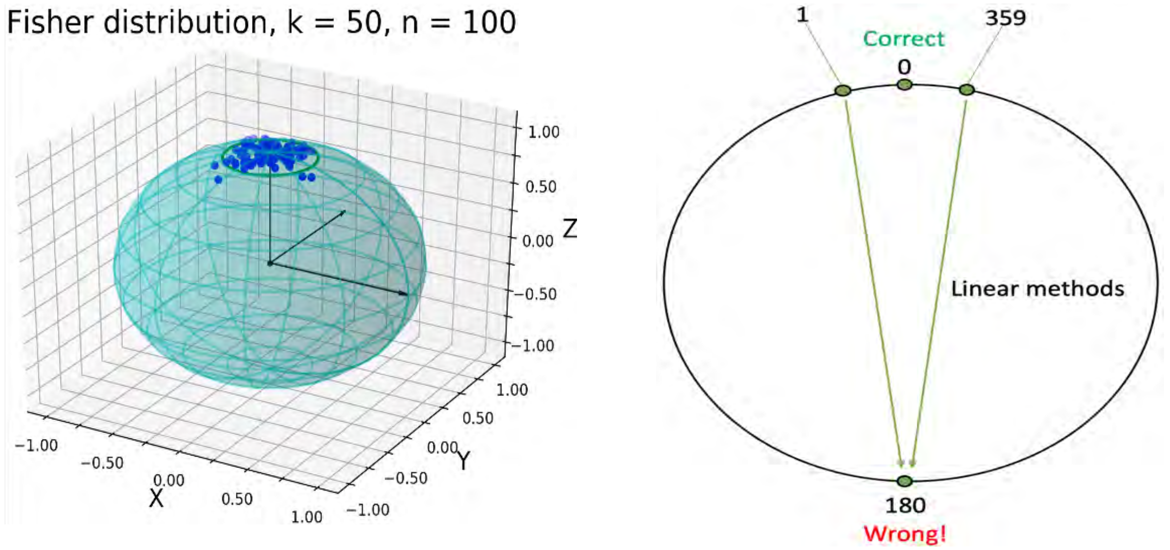

Figure 48*: Left: isotropic Fisher distribution with concentration parameter 50. Right: an example depicting how a naïve implementation of linear methods on a sphere fails. If there are two points with angular values of 359 and 1 degrees, we will compute their mean to be 180, although the correct value would be 0.*

When data are distributed on a sphere statistical methods have to take into account that spheres have inherently different topology than flat surfaces (Fisher 1953, Watson 1966). Thus, the methods for statistical inference on flat surfaces must be modified to remain meaningful. This is what motivates the study of spherical statistics initiated by Ronald Fisher in 1950s. Spherical statistics operates with vectors that are not suffering from the problems of a discontinuous (periodic) angular range. If two vectors have azimuths of 359 and 1 degrees, we may naively compute their mean to be 180 instead of 0 degrees. This is taken care of in spherical statistics, by operating with vectors and by using quantities that are independent of polar coordinates.

Methods for spherical statistics can be derived theoretically by considering exponential distributions centered on a pole of a sphere. Analyses applied to distributions on a sphere are similar to those on the plane, since fundamentally their origins are the same. Statistical moments are present in spherical and linear statistics and their formulations are similar. The main test statistics for inference on spheres come from representing data points as vectors. Important quantities are the mean vector of the sampled points, the mean resultant direction, and its magnitude, the mean resultant length. Many statistical tests are derived from manipulations with those quantities.

Mentioned above, for highly concentrated distributions on a sphere, linear methods provide results that approximate spherical results. This is due to the fact that the local properties on a sphere become increasingly more similar to those of a plane the closer we zoom in. Hence, in such cases it can be safe to apply appropriate linear methods and get the same results. However, this should be validated via simulations, which we did in the past to make sure the results from spherical and linear methods are consistent.

4.3 Results

4.3.1 Database

Since the last report we have increased the number of successful recordings from dipteran fly species from ***158*** to ***205*** and characterized the receptive field of a directional-selective cell in the lobula complex of the common wasp, *Vespula vulgaris*.

Given the shortage of large hoverfly species, we focused on studies of the black soldier fly, *Hermetia illucens*, a common stratiomyid which is phylogenetically almost as old as tabanids. The animals have an elongated body and are less compact than *Calliphora*. They are fairly manoeuvrable, nonetheless, and males engage on chasing flights in the tight confines of a 50x50x50cm insect cage to catch females on the wing as part of their mating behaviour, while avoiding collisions with other males. Soldier flies have almost spherical head shapes, except for a flat rear head capsule, and feature a regular hexagonal eye lattice that is dark, with conspicuous coloured markings (Figure 50).

4.3.2 Directional-selective cells in the lobula plate of Hermetia

In *Hermetia* the LPTC most often encountered is a motion sensitive cell responding to back-to-front motion in the ipsilateral (with respect to the location of the recording electrode) visual field (Figure 49, top row). The general receptive field organization is very similar to the receptive field of the blowfly H1-cell. Action potentials can be recorded either dendritically or telodendritically in the ipsilateral or contralateral lobula plate, respectively, which suggests a similar arborisation pattern as found in *Calliphora*.

Another neuron that has a clear cut receptive field organization and input structure as a well-known blowfly LPTC is the V1-like cell (Figure 49, second row). Here the distribution of LPDs and LMSs is reminiscent of a *Calliphora* V1-cell with its slightly less conspicuous sensitivity to vertical upward motion in the caudodorsal visual field. The cell can only be recorded in the contralateral lobula plate where its telodendiric output branches arborize.

The third cell type that has strong resemblance to a spiking LPTC well-studied in *Calliphora* is the V2-like cell (Figure 49, bottom row). This is both in *Hermetia* and *Calliphora* one of the few cells sensitive to vertical upward rather than downward motion. Like in H1-cells, its spikes can be recorded in its dendritic or teleodendritic arborizations, the latter of which are – in *Calliphora* – found in the most posterior layer of the lobula plate.

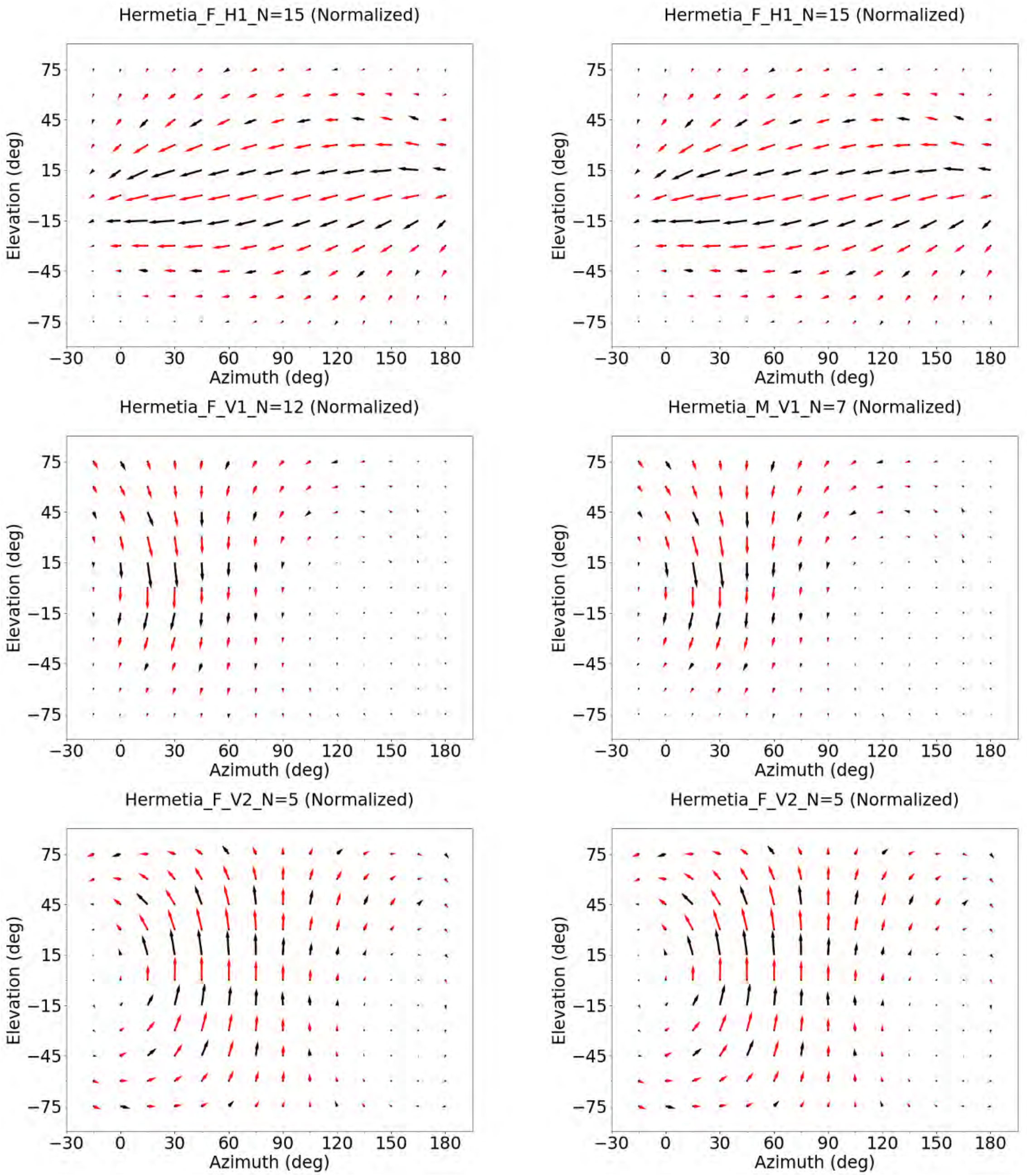

Figure 49: *Receptive field organization of H1-like-, V1-like- and V2-like-cells in* Hermetia*. Local preferred directions and motion sensitivities are plotted as vectors at different stimulus positons in terms of azimuth and elevation within the visual field. Black and red arrows give measured and interpolated data, respectively. Left column: data obtained in females. Right column: data obtained in males. In all cases the mean of at least 5 experiments is shown. Note the smoothness of the directional distributions and the large extent of the receptive fields – in particular that of the H1-like cell.*

Finally, we analysed the data based on recordings from *Calliphora* Vx-cells in males and females as well as from similar LPTCs in *Hermetia* females. Its input organization suggests the Vx-like cell in *Hermetia* to have similar response properties as the Vx-cell in *Calliphora*. Its main sensitivity is to vertical downward motion in the caudo-lateral visual field, but the cell also responds to slightly oblique upward motion and horizontal front-to-back motion in the frontal to frontolateral visual field (Figure 50, left).

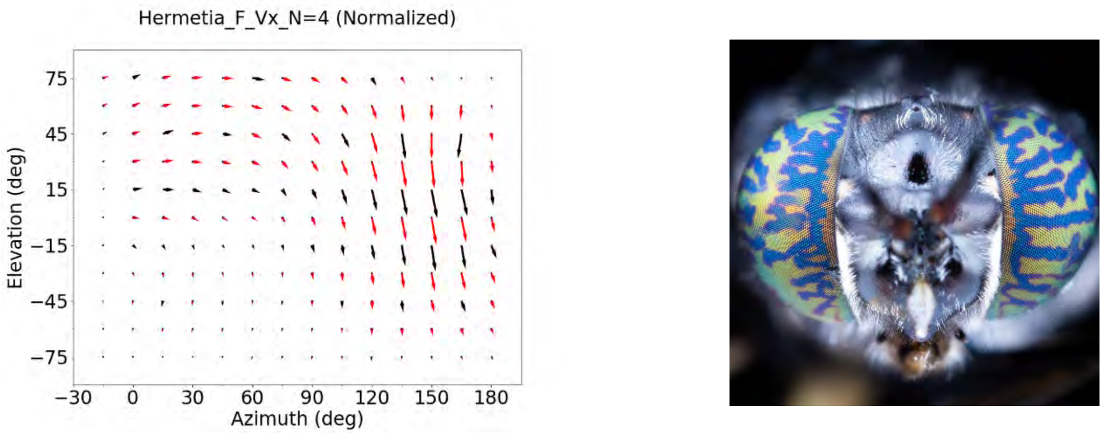

Figure 50: *Left: Mean receptive field organization of Vx-cell like LPTCs in female* Hermetia*. Right: Portrait of a female* Hermetia*. The compound eyes show a hemispherical appearance featuring a dense hexagonal eye lattice that has not yet been quantitatively characterized. The number of ommatidia per compound eye is likely to be greater than observed in female* Calliphora *(Petrowitz et al. 2000).*

A qualitative comparison of the H1-cell receptive field organization between *Hermetia* and *Calliphora* shows a marked difference in terms of the overall receptive field size. Motion sensitivities in *Hermetia* extend way further into the dorsal and ventral visual field and show hardly any anisotropic reduction along the eye equator in the frontal to cauda direction, which is clearly seen in *Calliphora* (Figure 54). V1-like and Vx-like LPTC receptive fields in *Hermetia* show similar sizes as their counterparts in *Calliphora*, while the gradients of the LPDs between vertical downward-horizontal-vertical upward are more pronounced in the blowfly. The V2-cell and V2-like cell, on the other hand show essentially the same overall organization in both species, but the cells' preferred rotation axes are different in *Calliphora* and *Hermetia* as revealed by the KvD analysis.

4.3.3 Preferred rotation axes of spiking LPTCs in Calliphora and Hermetia

We used the KvD under the assumption of an isotropic distance distribution (see Methods section) to retrieve the preferred self-motion parameters of our entire data set. Here, we only give the preferred rotation axes of the different cell-types in male and female *Calliphora* and *Hermetia*. They are described in terms of their azimuth and elevation components, $\boldsymbol{PR}_{\varphi}$ and $\boldsymbol{PR}_{\theta}$, respectively. We first tested whether, for the different cell types in a given species data obtained from males and females did show any significant differences (Table 7). In case we did not find differences, we pooled the data for each species and cell type across sexes. The results are shown in Table 8.

Table 7: *Results of the KvD analysis of spiking LPTCs in Calliphora and Hermetia.* ***PR_{φ}*** *and* ***PR_{θ}*** *give the mean azimuth and elevation of the preferred rotating axes +/- standard deviation, respectively.*

	Calliphora♀	Calliphora♂	Hermetia♀	Hermetia♂
H1	**N** = 18 ***PR_{φ}*** = -23.95±4.51° ***PR_{θ}*** = -84.62±4.93°	**N** = 10 ***PR_{φ}*** = 12.17±6.62° ***PR_{θ}*** = -82.39±5.45°	**N** = 15 ***PR_{φ}*** = -21.98±3.21° ***PR_{θ}*** = -83.42±3.10°	**N** = 9 ***PR_{φ}*** = -26.45±3.56° ***PR_{θ}*** = -84.20±4.38°
V1	**N** = 14 ***PR_{φ}*** = -80.96±11.61° ***PR_{θ}*** = 4.22±7.32°	**N** = 4 ***PR_{φ}*** = -75.53±7.78° ***PR_{θ}*** = -7.08±10.64°	**N** = 12 ***PR_{φ}*** = -66.04±6.58° ***PR_{θ}*** = 6.56±6.10°	**N** = 7 ***PR_{φ}*** = -62.21±11.80° ***PR_{θ}*** = 5.03±4.75°
V2	**N** = 2 ***PR_{φ}*** = 6.24±0.33° ***PR_{θ}*** = -12.65±0.11°	**N** = 3 ***PR_{φ}*** = 11.97±4.23° ***PR_{θ}*** = -16.23±4.31°	**N** = 5 ***PR_{φ}*** = -21.34±5.77° ***PR_{θ}*** = 4.71±3.99°	**N** = 4 ***PR_{φ}*** = -22.46±5.76° ***PR_{θ}*** = 1.57±2.24°
Vx	**N** = 16 ***PR_{φ}*** = 63.76±9.19° ***PR_{θ}*** = 12.99±7.03°	**N** = 2 ***PR_{φ}*** = 50.67±5.10° ***PR_{θ}*** = 14.19±3.52°	**N** = 4 ***PR_{φ}*** = 69.70±8.53° ***PR_{θ}*** = 16.93±6.52°	**N = 0**

Table 8: *Preferred rotation axes pooled across sexes.*

	Calliphora	Hermetia
H1	**N** = 28 ***PR_{φ}*** = -8.2±5.9° ***PR_{θ}*** = -84.1±5.0°	**N** = 24 ***PR_{φ}*** = -23.5±3.4° ***PR_{θ}*** = -83.7±3.6°
V1	**N** = 18 ***PR_{φ}*** = -79.8±11.0° ***PR_{θ}*** = 1.7±9.4°	**N** = 19 ***PR_{φ}*** = -64.6±9.1° ***PR_{θ}*** = 6.0±5.7°
V2	**N** = 5 ***PR_{φ}*** = 9.7±4.3° ***PR_{θ}*** = -14.8±3.7°	**N** = 9 ***PR_{φ}*** = -21.8±5.8° ***PR_{θ}*** = 3.3±3.7°
Vx	**N** = 18 ***PR_{φ}*** = 62.3±10.0° ***PR_{θ}*** = 13.2±6.7°	**N** = 4 ***PR_{φ}*** = 69.7±8.5° ***PR_{θ}*** = 16.9±6.5°

The (spherical) statistical analysis of the preferred rotations axes did not indicate any differences between LPTCs properties obtained in male and female flies – except for (i) data on *Hermetia* Vx-like cells where we did not achieve any recordings from male flies. We therefore took only the data gathered from female flies for the overall preferred rotation axis of the Vx-like cell in *Hermetia*.

4.3.4 Distribution of preferred rotation axes in Calliphora *and* Hermetia *spiking LPTCs*

To compare the results obtained from the most encountered spiking LPTCs in blowflies and soldier, we plotted the preferred rotation axes of the H1-, V1-, V2, and Vx-cells in spherical coordinates (Figure 51).

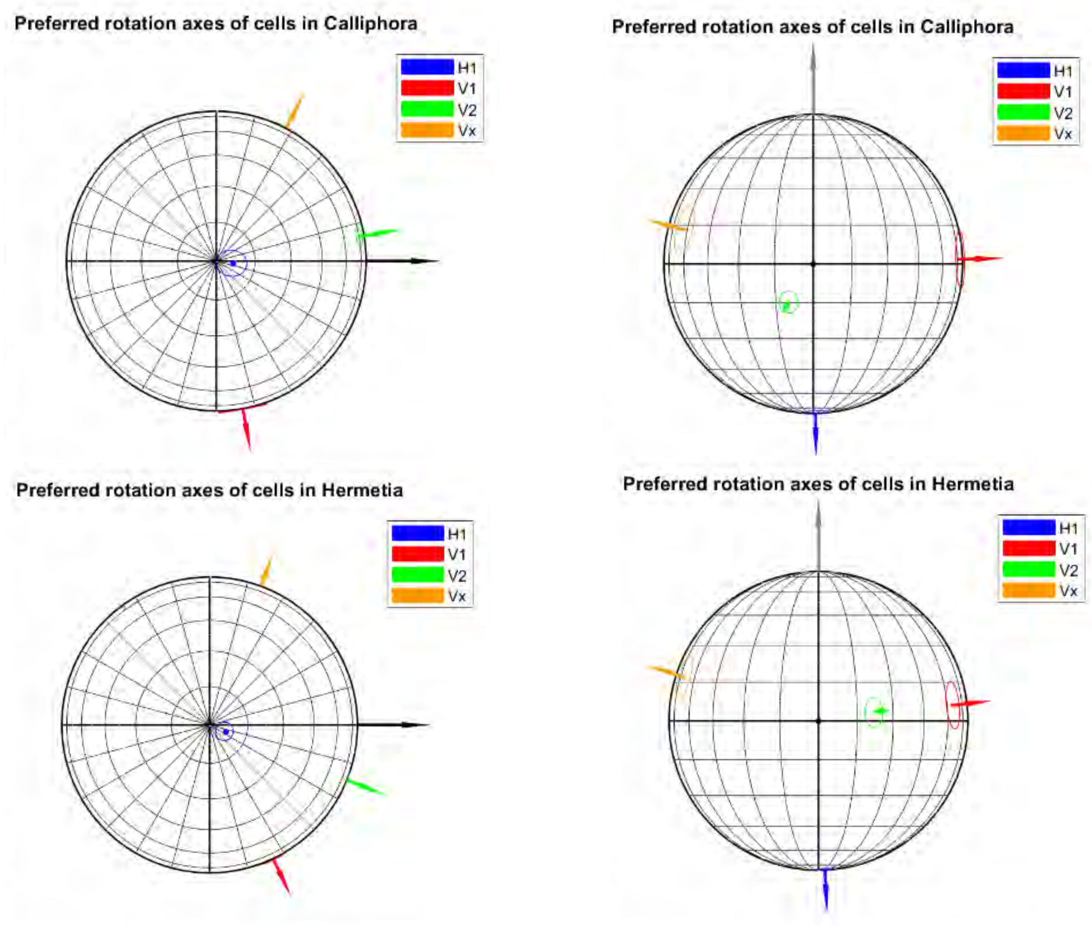

Figure 51*: Mean preferred rotation axes of spiking LPTCs in* Calliphora *(top row) and* Hermetia *(bottom row) +/- angular deviation. Left plots show a view of the sphere from below (along –z), the right plot shows a view along + thrust axis (+x). The black arrow in the left plots gives the orientation of the +x-axis, the grey arrow in the right plots gives the +z-axis. While the H1-cell and the H-like cell show nearly identical axes orientations in* Calliphora *and* Hermetia*, the V1-like cell and V1-cell prefer similar body rotations. The same is true for the Vx-like cells and the Vx-cells. The only conspicuous difference between* Calliphora *and* Hermetia *can be noted for the V2-like- and the V2-cell. In* Hermetia *it points into the contralateral visual field (green arrow, left hand plots) while the preferred rotation axis of the Vx-cell remains in the ipsilateral visual field.*

It is important to keep in mind when inspecting the orientation of the preferred rotation axes shown in Figure 51 that only the results obtained from cells studied in one lobula plate are presented. Each cell has got a contralateral counterpart which means that a total of 6 heterolateral LPTCs are analysing optic flow induced by rotations around horizontal body rotations.

Spherical statistical tests confirm that only the mean preferred rotation axis of the V2-like cell in

Hermetia and the V2-cell in *Calliphora* are significantly different. For all other spiking LPTCs of these two species the null hypothesis could not be rejected.

4.4 Discussion

4.4.1 Summary

The results presented here show a remarkable similarity between the preferred rotation axes measured in two different species which have emerged at different times during the evolution of dipteran flies, the modern blowfly *Calliphora* and the more ancient soldier fly *Hermetia*. The only difference of about 30 degrees we found is the orientation of the preferred rotation axis in a cell that has been suggested to sense roll body rotations – the V2-cell or V2-like cell. All other preferred rotation axes are essentially the same.

4.4.2 Heterolateral LPTCs in Calliphora

The two dipteran fly species where the cellular equipment in the lobula plate has been most extensively studied are blowflies (*Calliphora*) and fruit flies (*Drosophila*). The estimate by Hausen (1984) that there are about 50-60 wide field tangential cells in the lobula plate has been corrected to greater numbers in *Drosophila* due to studies at HHMI Janelia Farm over the past couple of years. Still, both fruit flies and blowflies are equipped with HS- and VS-cells which allows for some educated guesses regarding the connectivity and directional selectivity of homologous cells in both species. This is because of extensive electrophysiological work on LPTCs in *Calliphora*, the receptive field organization of about 40 cells have been characterized, many of them in combination with a morphological identification. It is therefore reasonable to assume that the connectivity scheme between the lobula plates in both parts of the brain established by heterolateral cells are similar, if not identical.

For the V1-cell it was shown that it does not receive its own retinotopic input, but that it inherits its sensitivity to vertical downward motion in the frontolateral visual field from inputting cells VS1-3 (rev. Krapp and Wicklein 2008). The mean preferred rotation axis across this group of VS-cells according to a previous blowfly study (Krapp et al. 1998) would be at an azimuth of about -75 degree (in the coordinate system used here), which well corresponds to the mean preferred rotation axis of the V1-cell in *Calliphora* of -80 degrees reported here. Similarly, the mean preferred axis of the Vx-cells at an azimuth of 62 degrees we found also corresponds with the mean of 60 degrees in the same previous study as a result of averaging across the data retrieved from VS8-10. However, in this case there is no evidence that the latter VS-cells provide the input to the Vx-cell. But we can only conclude that the same local direction input elements feeding into VS8-10 may also provide for the Vx-cell. The remaining group of VS-cells, VS4-VS7, have a mean preferred rotation axis of about 22 degrees azimuth which is close enough to the value of 10 degrees obtained in our current study. But again, no electrophysiological experiments have been reported so far which support any synaptic connections.

Evidence that potentially support the grouping that would explain the preferred rotation axes we found come from past behavioural studies on the roll sensitivity of blowflies as a function of stimulus elevation (Hengstenberg and Krapp 1996). Back then the behavioural roll responses were best explained by the combined input from VS4-VS7, which leaves VS1-3 and VS8-10 as two further potential functional sup-groups reflecting the preferred rotation axes of the V1- and Vx-cells as suggested above. Further electrophysiological experiments will be needed to clarify the connectivity between VS- and V-cells in *Calliphora* using simultaneous double recordings. Our data allow us to make predictions about the potential connectivity base on the receptive field organization of the cells we have investigated – which has been a successful strategy in the past (Krapp et al. 2001).

As far as the H1-cell is concerned, previous studies in *Calliphora* suggest this neuron to be part of a heterolateral network of LPTCs that establishes yaw rotation specificity and includes the HS-cells, HSN and HSE (rev. Krapp and Wicklein 2008) and other horizontal cells. Double recordings have shown the H1-cell to provide rotation-specific input to the HSE-cell.

4.4.3 Heterolateral LPTCs in different dipteran families

As mentioned above, there is not much information available about LPTC physiology and morphology in species other than *Calliphora* and *Drosophila*. The only comparative morphological account on LPTCs in different dipteran species by Buschbeck and Strausfeld (1997) points out that different families clearly use different cellular equipment, both in terms of numbers and morphologies.

Our extended data base including recordings from 9 dipteran species allows us to make a strong point about the existence of LPTCs with VS-cell like properties based on the fact that we were able to record from V1-like cells in basically all flies we investigated so far. Should the input organization of the V1-cell be conserved in dipteran flies, it is highly likely that in older families such as Tabanids and Stratiomyids cells exist that are at least functionally homologous to VS-cells. Along a similar line of arguments, we would also assume that networks of HS-like cells are present in the species studied so far as they all had H1-like LPTCs. The H1-cell, or equivalent, was meanwhile also recorded from in locusts, robberflies and wasps – which indicates the universal need to sense wide-field optic flow generated during yaw rotations.

The other heterolateral LPTCs including the V2- and Vx cells were also recorded from most of the species we studied over the last 2 years. We are now in a position to make predictions on the properties of the HS- and VS-cells based on the data we have accumulated by now, including potential connectivity schemes, which would guide further electrophysiological studies.

4.4.4 Heterolateral LPTCs in different dipteran families

We are still analysing our database with respect to the arrangement of preferred rotation axes in heterolateral LPTCs characterized in other dipteran flies including different hoverfly species. This will allow us to identify whether the equipment of heterolateral LPTCs is to be interpreted as a general functional principle to disambiguate optic flow-based state estimation, or whether subtle differences between different species suggest specific adaptations. In parallel, we are currently working on a comprehensive publication of our comparative data and a publication on the relationship of visual sensory and the motor coordinate systems controlling the flight dynamics in *Calliphora*.

5 Evaluation of LPTC Directional Templates in the Context of Dynamically Significant Directions in *Calliphora* (Sean Humbert, University of Colorado)

In the following we discuss the encoding properties of various LPTC directional templates in the context of dynamically significant directions of *Calliphora* now that we have a complete characterization of the matrices $\mathbf{A}$, $\mathbf{B}$, $\mathbf{G}$ and $\mathbf{C}$ (Table 1). First, we describe the framework used to process the data described in Section 4 to generate the $\mathbf{C}$ matrix, corresponding to directions in state space that are encoded by each LPTC. These are subsequently compared to the natural modes, the independent columns of the controllability matrix, and the observability, controllability joint controllability/observability and disturbance sensitivity directions based on the respective gramians. In this analysis, we make use of the newly developed flight dynamics model ($\mathbf{A}$, $\mathbf{B}$ and $\mathbf{G}$ matrices based on CFD simulations (Section 3) and the proper parameterization of the control input vector ($\mathbf{B}$ matrix) based on the principal components (Section 2).

5.1 Control-theoretic LPTC modeling

LPTCs are large, motion-sensitive neurons that reside in the visuomotor systems of most flying insects. They are believed to pool the outputs of large numbers of local optic flow estimates and respond with graded membrane potentials whose magnitude is both spatially and directionally selective (Krapp & Hengstenberg, 1996; Krapp *et al*., 1998). The matched filter hypothesis proposed in Franz & Krapp, 2000 suggests the cell's output can be considered as a comparison between the cell's directional template with the pattern of the visual stimulus. Mathematically, this comparison can be modeled as an inner product on a discrete spatial domain (Franz & Krapp, 2000; Dahmen *et al*., 2001; Franz *et al*., 2004) or a continuous spatial domain (Humbert *et al*., 2005; Humbert & Hyslop, 2010; Hyslop and Humbert 2010). LPTC outputs $y_i(\boldsymbol{x})$ are then defined as the inner product between the instantaneous pattern of optic flow $\dot{\boldsymbol{Q}}$ and the tangential cell's directional template $\boldsymbol{F}_i$,

$$y_i(x) \;=\; \langle \dot{\mathbf{Q}}, \mathbf{F}_i \rangle \;=\; \int_{S^2} \dot{\mathbf{Q}} \cdot \mathbf{F}_i \, d\Omega, \quad i = 1, \ldots, m$$

Considered as a set, a collection of tangential cell outputs form a nonlinear output equation $\boldsymbol{y} = \boldsymbol{h}(\boldsymbol{x})$. To characterize the small signal content encoded by each measured directional template, each output $y_i(\boldsymbol{x})$ needs to be linearized about the reference flight equilibrium $\bar{\boldsymbol{x}}$. The resulting linearized matrix in the output equation $\boldsymbol{y}(t) = \mathbf{C}\boldsymbol{x}(t)$ is given by

$$\mathbf{C}_{ij} \;=\; \left.\frac{\partial \mathbf{h}_i}{\partial x_j}\right|_{\bar{x}} \;=\; \left.\frac{\partial \langle \dot{\mathbf{Q}}, \mathbf{F}_i \rangle}{\partial x_j}\right|_{\bar{x}} \;=\; \left.\left\langle \frac{\partial \dot{\mathbf{Q}}}{\partial x_j}, \mathbf{F}_i \right\rangle\right|_{\bar{x}}$$

In this form, each row of the associated $\mathbf{C}$ matrix represents the rigid body state content present in the signal from a specific LPTC directional template, that is, the direction it encodes in state space.

5.1.1 Optic flow and 3D environment model

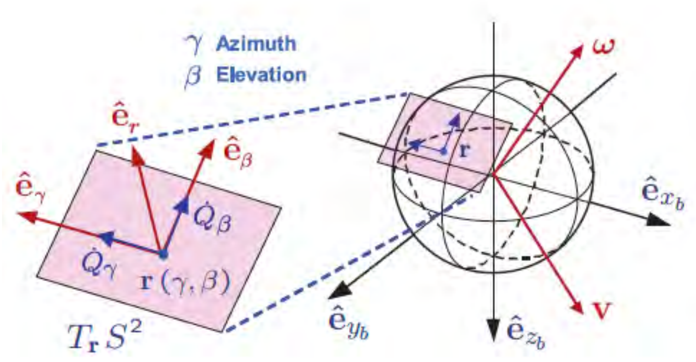

Figure 52: *Geometry for spherical optic flow (Hyslop and Humbert, 2010).*

The (true) optic flow is the vector field of relative velocities of material points in the environment projected into the tangent space of the imaging surface (Figure 52). It is the combination of the observer's rotational and translational motion, with the translational portion being inversely scaled by the proximity to surrounding objects. For a given angular velocity $\boldsymbol{\omega}$ and translational velocity $\boldsymbol{v}$, along with the nearness function μ which represents the inverse of the distance to objects in the environment, the instantaneous optic flow pattern $\dot{\boldsymbol{Q}}$ on a spherical imaging surface S^2 for an arbitrary distribution of obstacles can be expressed as

$$\dot{\mathbf{Q}} = -\boldsymbol{\omega} \times \mathbf{r} - \mu[\mathbf{v} - \langle \mathbf{v}, \mathbf{r} \rangle \mathbf{r}]$$

The quantity $\dot{\boldsymbol{Q}} = \dot{Q}_\gamma \hat{\boldsymbol{e}}_\gamma + \dot{Q}_\beta \hat{\boldsymbol{e}}_\beta$ has components in the azimuth γ and elevation β directions (Figure 52). If one expresses the body velocity $\boldsymbol{v} = (u, v, w)$ and the angular velocity $\boldsymbol{\omega} = (p, q, r)$ in the coordinates of the body frame $(\hat{\boldsymbol{e}}_{x_b}, \hat{\boldsymbol{e}}_{y_b}, \hat{\boldsymbol{e}}_{z_b})$, the expressions for the azimuthal and elevation components are

$$\begin{aligned}
\dot{Q}_\gamma &= p\cos\beta\cos\gamma + q\cos\beta\sin\gamma - r\sin\beta + \mu(u\sin\gamma - v\cos\gamma) \\
\dot{Q}_\beta &= p\sin\gamma - q\cos\gamma + \mu(-u\cos\beta\cos\gamma - v\cos\beta\sin\gamma + w\sin\beta).
\end{aligned}$$

In order to completely specify the optic flow pattern in closed form, simplifying assumptions are required on the shape of the nearness function $\mu(\gamma, \beta, \boldsymbol{q}) = 1/d(\gamma, \beta, \boldsymbol{q})$, where $d(\gamma, \beta, \boldsymbol{q})$ is the distance from the imaging surface to the nearest object in the environment along the direction $\hat{\boldsymbol{e}}_r$ (Figure 52) through a point on the imaging surface $\boldsymbol{r} = (\gamma, \beta)$. This function encodes the relative pose $\boldsymbol{q} = (x, y, z, \phi, \theta, \psi)$ where (x, y, z) are the coordinates of the vantage point with respect to the inertial frame and (ϕ, θ, ψ) are the 3-2-1 Euler angles of the body frame relative to the inertial frame. For an enclosed rectangular prism (Figure 53A), the nearness $\mu(\gamma, \beta, \boldsymbol{q})$ is a piecewise-continuous function given by

$$\mu(\gamma,\beta,\mathbf{q}) \;=\; \begin{cases} \dfrac{s\beta(c\psi c\theta c\gamma + s\gamma(s\phi s\theta - c\phi s\psi c\theta)) + c\beta(s\phi s\psi c\theta + c\phi s\theta)}{g_N - x} & \text{front wall} \\ -\dfrac{s\beta(c\psi c\theta c\gamma + s\gamma(s\phi s\theta - c\phi s\psi c\theta)) + c\beta(s\phi s\psi c\theta + c\phi s\theta)}{g_S + x} & \text{rear wall} \\ \dfrac{s\beta(c\gamma c\theta s\psi + s\gamma(s\phi s\theta s\psi + c\phi c\psi)) + c\beta(c\phi s\theta s\psi - s\phi c\psi)}{a_E - y} & \text{right wall} \\ -\dfrac{s\beta(c\gamma c\theta s\psi + s\gamma(s\phi s\theta s\psi + c\phi c\psi)) + c\beta(c\phi s\theta s\psi - s\phi c\psi)}{a_W + y} & \text{left wall} \\ \dfrac{s\beta(s\phi c\theta s\gamma - s\theta c\gamma) + c\beta c\phi c\theta}{h_D - z} & \text{ground} \\ -\dfrac{s\beta(s\phi c\theta s\gamma - s\theta c\gamma) + c\beta c\phi c\theta}{h_U + z} & \text{ceiling} \end{cases}$$

Parameters $(g_N, g_S, a_E, a_W, h_D, h_U)$ represent the desired distance from the walls at the equilibrium position. The bounds for the validity ranges of each μ sub-function specify where the surfaces intersect, but due to their complexity they can only be computed numerically.

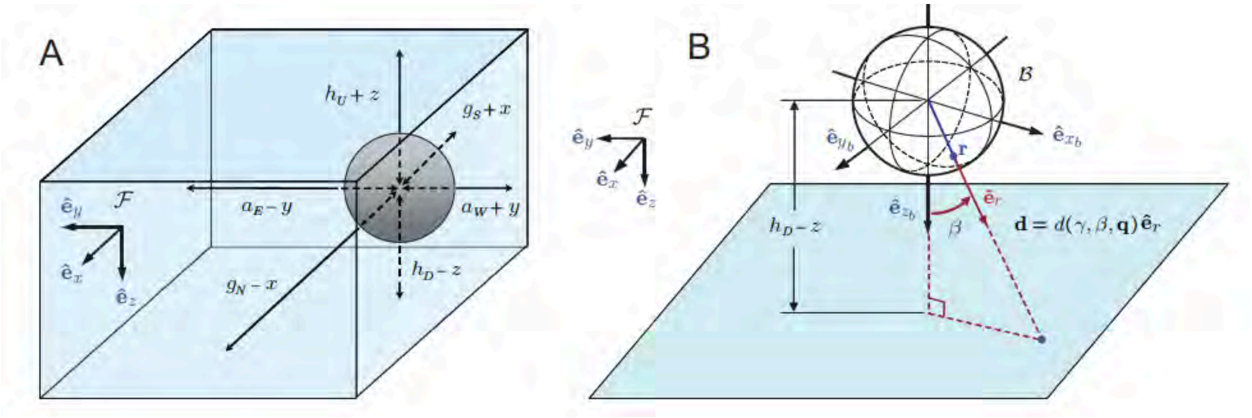

***Figure 53**: 6-wall environment models for the nearness function approximation (A) enclosed room with translational perturbations, (B) Flat terrain and definition of the distance function $d(\gamma, \beta, \boldsymbol{q})$, (Hyslop and Humbert, 2010).*

5.1.2 Estimation of the output matrix **C** *for LPTC directional templates*

To develop the **C** matrix for a set of directional templates, the raw receptive field data provided by Prof. Holger Krapp was first converted into body frame coordinates according to the geometry of Figure 53. Note that $\boldsymbol{r} = (\gamma, \beta) = (0, 90°)$ is the ray along the $\hat{\boldsymbol{e}}_{x_b}$ axis in Figure 52. Figures 54-58 are the corresponding directional templates. Note that the raw data include the ‘ipsi’ and ‘both’ configurations, which correspond to data taken over a left or right hemisphere or the entire visual field, respectively.

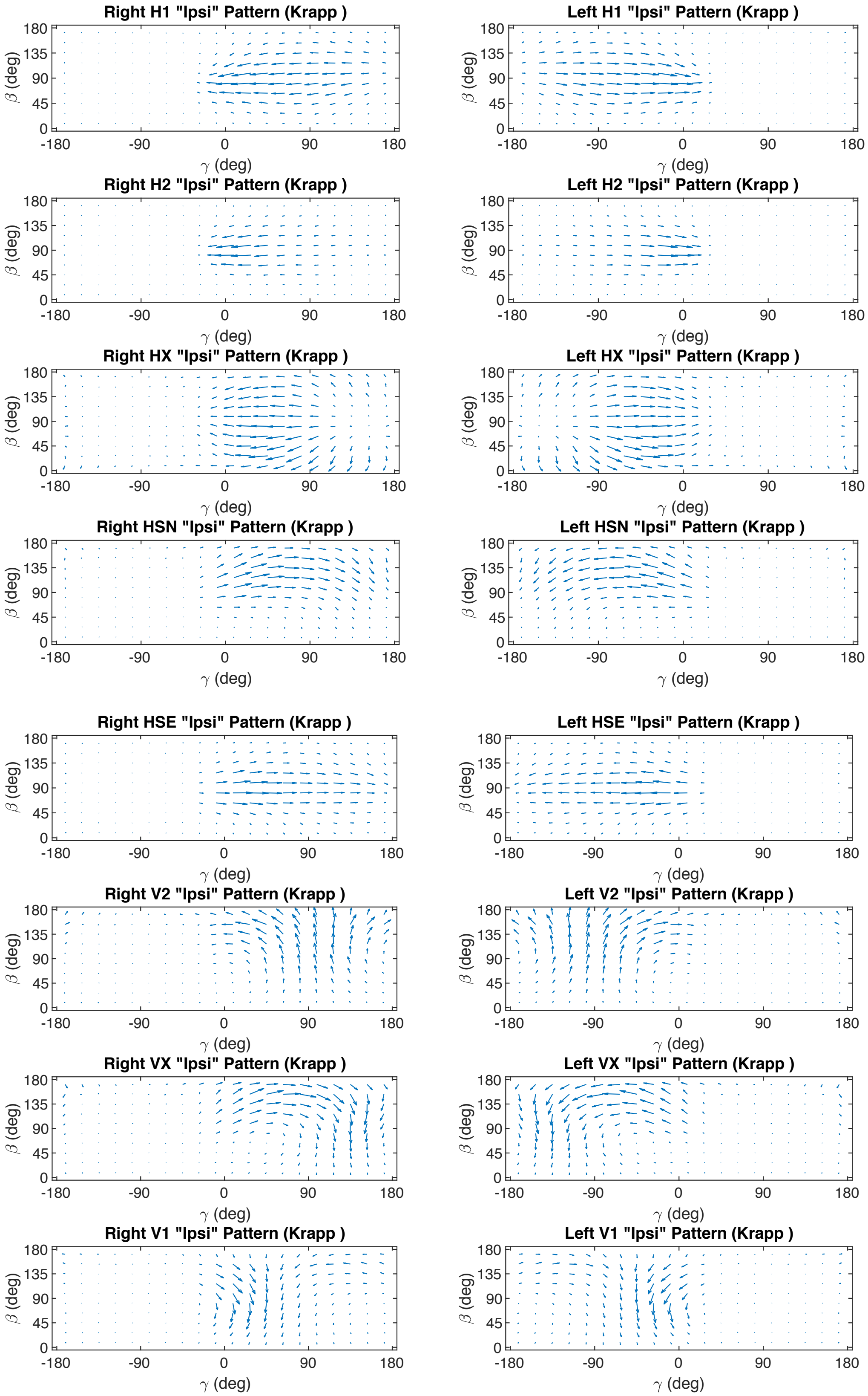

***Figure 54**: LPTC directional template raw data*

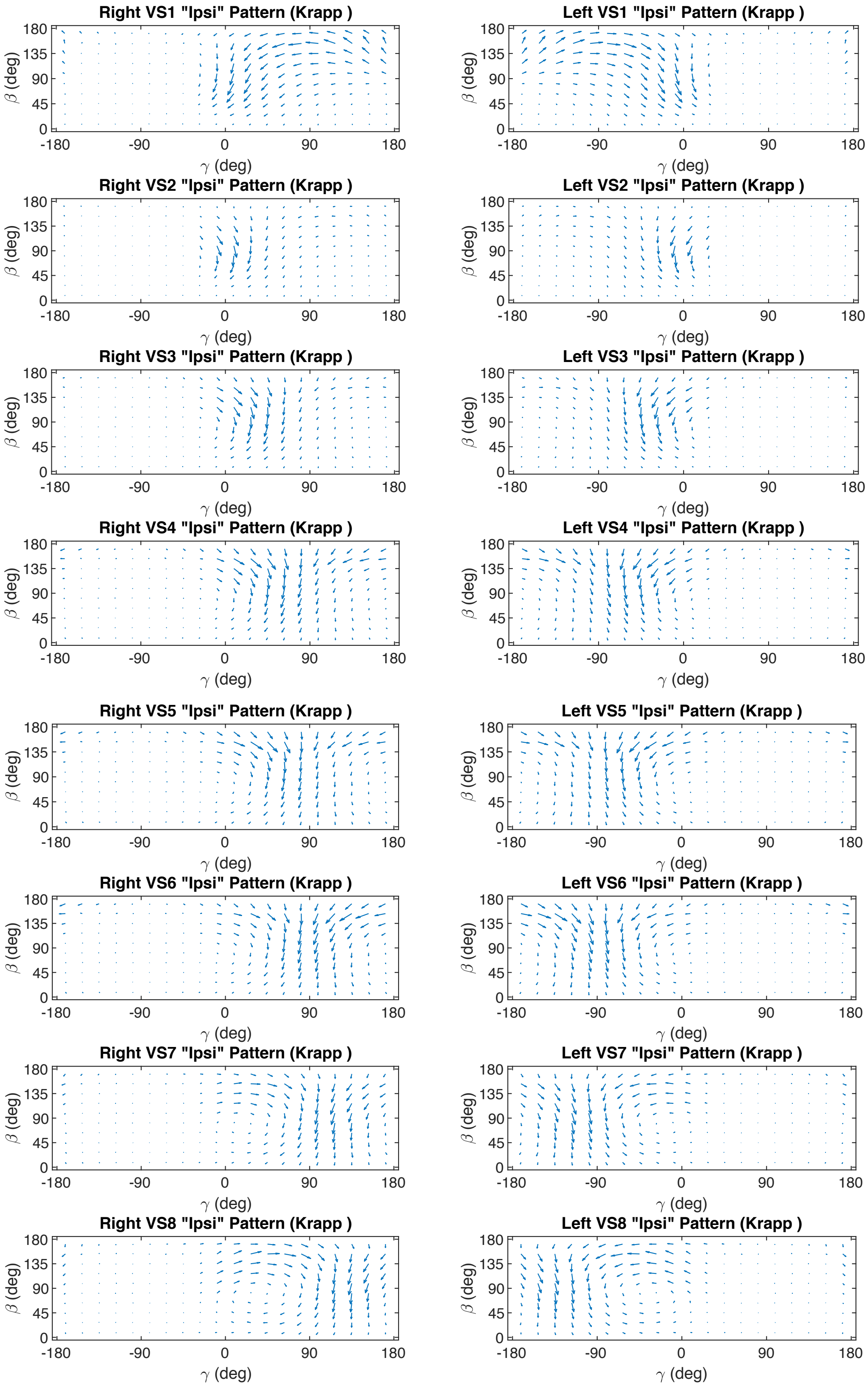
Right VS1 "Ipsi" Pattern (Krapp)
Left VS1 "Ipsi" Pattern (Krapp)
Right VS2 "Ipsi" Pattern (Krapp)
Left VS2 "Ipsi" Pattern (Krapp)
Right VS3 "Ipsi" Pattern (Krapp)
Left VS3 "Ipsi" Pattern (Krapp)
Right VS4 "Ipsi" Pattern (Krapp)
Left VS4 "Ipsi" Pattern (Krapp)
Right VS5 "Ipsi" Pattern (Krapp)
Left VS5 "Ipsi" Pattern (Krapp)
Right VS6 "Ipsi" Pattern (Krapp)
Left VS6 "Ipsi" Pattern (Krapp)
Right VS7 "Ipsi" Pattern (Krapp)
Left VS7 "Ipsi" Pattern (Krapp)
Right VS8 "Ipsi" Pattern (Krapp)
Left VS8 "Ipsi" Pattern (Krapp)

***Figure 55**: LPTC directional template raw data*

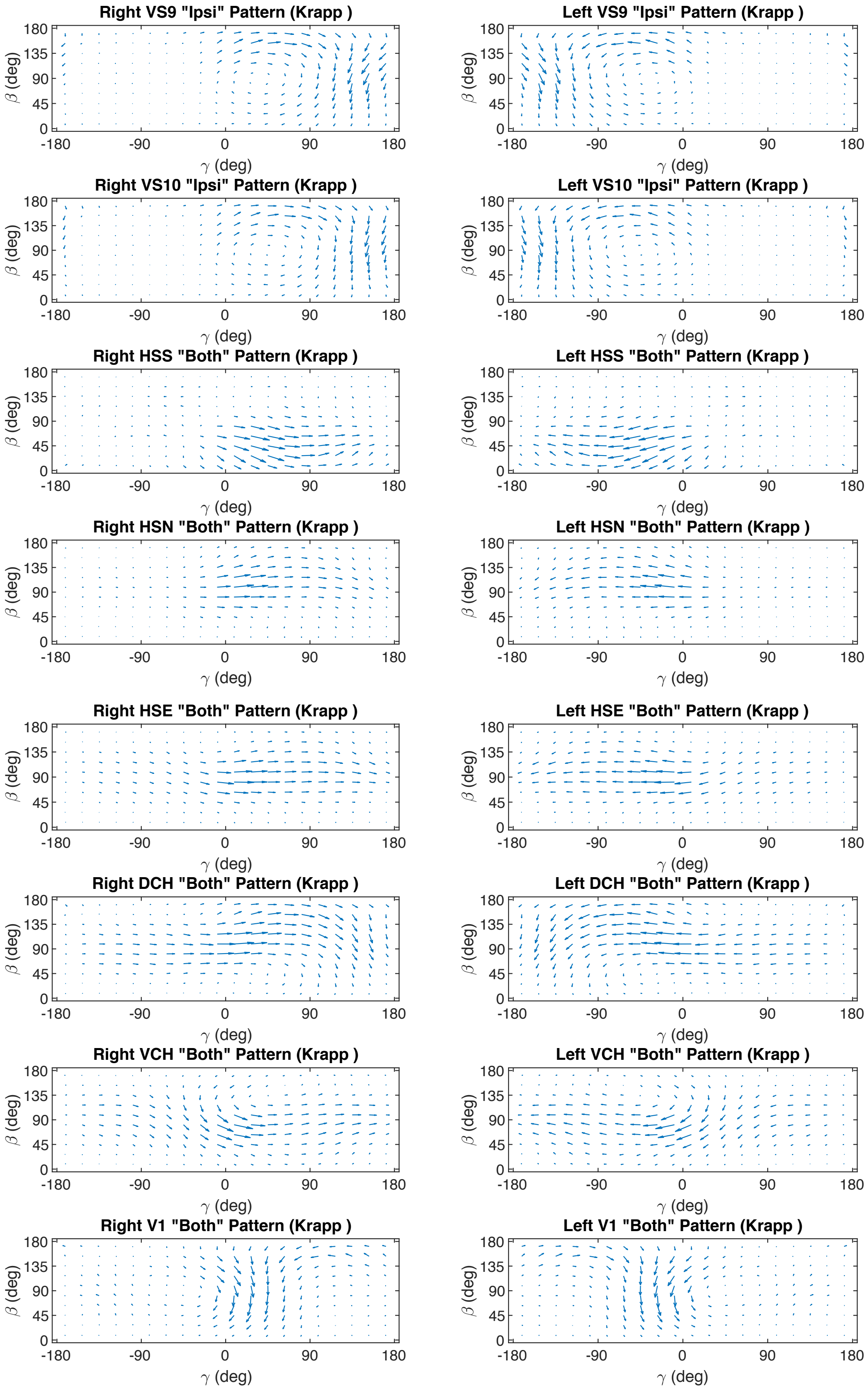

***Figure 56**: LPTC directional template raw data*

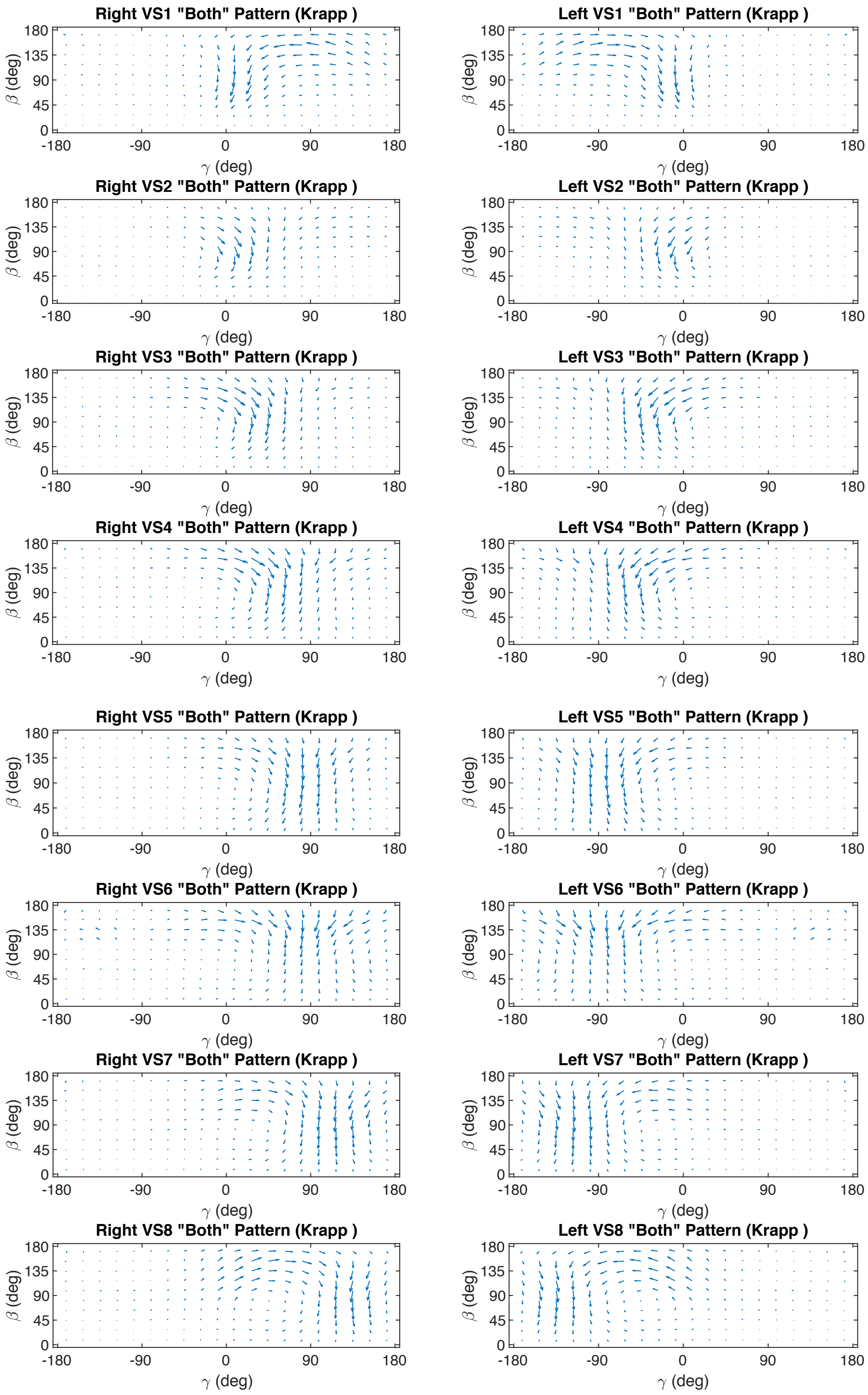
Right VS1 "Both" Pattern (Krapp)

Left VS1 "Both" Pattern (Krapp)

Right VS2 "Both" Pattern (Krapp)

Left VS2 "Both" Pattern (Krapp)

Right VS3 "Both" Pattern (Krapp)

Left VS3 "Both" Pattern (Krapp)

Right VS4 "Both" Pattern (Krapp)

Left VS4 "Both" Pattern (Krapp)

Right VS5 "Both" Pattern (Krapp)

Left VS5 "Both" Pattern (Krapp)

Right VS6 "Both" Pattern (Krapp)

Left VS6 "Both" Pattern (Krapp)

Right VS7 "Both" Pattern (Krapp)

Left VS7 "Both" Pattern (Krapp)

Right VS8 "Both" Pattern (Krapp)

Left VS8 "Both" Pattern (Krapp)

***Figure 57**: LPTC directional template raw data*

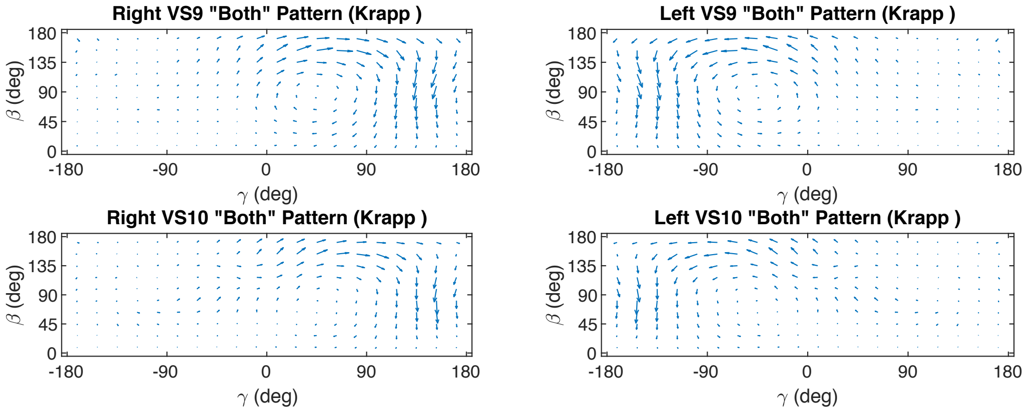

***Figure 58**: LPTC directional template raw data*

The recorded raw data were smoothed with a 2D Gaussian filter and then approximated with up to 10th degree spherical harmonics in the azimuth and elevation directions. The resulting approximated directional templates $\mathbf{F}_i$ were then normalized so that

$$\langle \mathbf{F}_i, \mathbf{F}_i \rangle \;=\; \int_0^{2\pi} \int_0^{\pi} \mathbf{F}_i \cdot \mathbf{F}_i \;\sin\beta \; d\beta \; d\gamma \;=\; 1$$

such that a perfect match of the optic flow field with the tangential cell receptive field will result in a unity output.

A 6-wall tunnel environment was assumed with scaling parameters $(g_N, g_S, a_E, a_W, h_D, h_U)$ set to a distance of 1 meter (Figure 53A), and the reference flight (equilibrium) condition was set to a forward flight speed of $u = 0.8509$ m/s, or $(u, w, q, \theta, v, p, \phi, r) = (0.8509\,,0\,,0\,,0\,,0\,,0\,,0\,,0)$ in the stability axes. Note that $\hat{\boldsymbol{e}}_{x_b}$ in Figures 52 and 53 for this specification of equilibrium condition corresponds to the $\boldsymbol{x}_s$ direction (stability axes) in Figure 59.

The corresponding partial derivatives of the optic flow $\partial\dot{\boldsymbol{Q}}/\partial x_i$ were computed by perturbing each of the rigid body states and taking finite differences. The results were then used to compute the inner products numerically, resulting in the estimated directional template state encoding, or the output $\mathbf{C}$ matrix shown in Tables 7 and 8. We note that the $\mathbf{C}$ matrix in this form is a function of the augmented state $\{x, y, z, \phi, \theta, \psi, u, v, w, p, q, r\}$. To perform the analysis, we extract the entries according to the state vector from the flight dynamics model formulation, $\boldsymbol{x} = \{u, w, q, \theta, v, p, \phi, r\}$. The states $\{x, y, z, \psi\}$ typically are not included in the linearized dynamics formulation since a homogeneous atmosphere assumption in employed.

***Table** 7: Estimated directional template state encoding (output* **C** *matrix) for the 'ipsi' versions of LPTC directional templates provided by Holger Krapp*

		x	y	z	phi	theta	psi	u	v	w	p	q	r
Right H1	Ipsi	-0.1008247	-0.6387772	0.03414972	0.00626597	0.0090764	0.0059878	-1.2827256	0.51165466	-0.2297892	-0.2709338	0.11574259	1.96023239
Left H1	Ipsi	-0.1008247	0.62235633	0.03414972	-0.0132286	0.0090764	-0.0384896	-1.2827256	-0.5116547	-0.2297892	0.2709338	0.11574259	-1.9602324
Right H2	Ipsi	-0.1925263	-0.3677595	0.02366278	0.00586466	-0.0022098	0.03247081	-0.8307153	0.81353552	-0.1703896	-0.1361669	0.15749468	1.67652929
Left H2	Ipsi	-0.1925263	0.3553396	0.02366278	-0.0108358	-0.0022098	-0.0571067	-0.8307153	-0.8135355	-0.1703896	0.13616692	0.15749468	-1.6765293
Right Hx	Ipsi	-0.1144251	-0.4908727	-0.0474674	0.00601566	-0.0196409	-0.0385158	-1.2659841	1.11012469	-0.0774741	-0.2645925	-0.1093035	1.49314915
Left Hx	Ipsi	-0.1144251	0.4808262	-0.0474674	-0.0107045	-0.0196409	0.01868307	-1.2659841	-1.1101247	-0.0774741	0.26459254	-0.1093035	-1.4931491
Right HSN	Ipsi	0.08508053	0.395772	-0.3012734	-0.0282217	-0.0090314	-0.0090939	1.08095384	-0.6088261	-0.258476	-0.6068024	-1.0442417	-1.5361196
Left HSN	Ipsi	0.08508053	-0.3852988	-0.3012734	0.03309086	-0.0090314	0.02982373	1.08095384	0.60882609	-0.258476	0.60680236	-1.0442417	1.53611963
Right HSE	Ipsi	0.0723408	0.57267	-0.0221777	-0.0043847	0.00131313	-0.0115109	1.18539981	-0.5834033	-0.095218	-0.1258509	-0.1389409	-1.9791519
Left HSE	Ipsi	0.0723408	-0.5571364	-0.0221777	0.01074077	0.00131313	0.0422706	1.18539981	0.58340334	-0.095218	0.12585092	-0.1389409	1.97915192
Right V2	Ipsi	-0.0076699	-0.1126582	0.11013645	0.0195636	0.00542139	0.00324791	-0.3405316	0.51569482	1.33535192	1.81809544	0.31589427	0.42591475
Left V2	Ipsi	-0.0076699	0.10976988	0.11013645	-0.0209347	0.00542139	-0.008963	-0.3405316	-0.5156948	1.33535192	-1.8180954	0.31589427	-0.4259148
Right Vx	Ipsi	0.05532082	0.14970415	-0.3876258	-0.0653231	-0.0057318	-0.0110253	0.64000764	-0.4263541	-0.7993854	-1.2029771	-1.463397	-0.5820587
Left Vx	Ipsi	0.05532082	-0.1458968	-0.3876258	0.06740263	-0.0057318	0.01855492	0.64000764	0.42635412	-0.7993854	1.2029771	-1.463397	0.58205867
Right V1	Ipsi	0.02340479	-0.1041365	0.21212184	0.0348809	0.02473871	-0.0169465	-0.3188059	-0.2606506	-1.3244473	-1.2274433	1.30578868	0.08473977
Left V1	Ipsi	0.02340479	0.10228619	0.21212184	-0.0359368	0.02473871	0.01330077	-0.3188059	0.26065063	-1.3244473	1.22744331	1.30578868	-0.0847398
Right VS1	Ipsi	0.00360424	-0.2905159	0.33327371	0.0614723	0.03629827	-0.012283	-0.9071747	0.21645512	-0.8989437	-0.5693114	1.55522107	1.01703832
Left VS1	Ipsi	0.00360424	0.28335173	0.33327371	-0.0649922	0.03629827	-0.0018864	-0.9071747	-0.2164551	-0.8989437	0.56931139	1.55522107	-1.0170383
Right VS2	Ipsi	-0.0419791	-0.1251194	0.15467983	0.01939454	0.05089783	-0.0162922	-0.4122989	-0.072093	-1.2885493	-0.7609748	1.38226375	0.26646143
Left VS2	Ipsi	-0.0419791	0.12192721	0.15467983	-0.0209362	0.05089783	0.00997908	-0.4122989	0.07209298	-1.2885493	0.76097482	1.38226375	-0.2664614
Right VS3	Ipsi	-0.0528235	-0.097766	0.14400236	0.02223465	0.0108911	-0.0096431	-0.3497992	-0.2108151	-1.3340569	-1.3618965	1.0645994	0.13472214
Left VS3	Ipsi	-0.0528235	0.09532496	0.14400236	-0.0235185	0.0108911	0.00481666	-0.3497992	0.21081509	-1.3340569	1.3618965	1.0645994	-0.1347221
Right VS4	Ipsi	-0.0220647	-0.1160547	0.09717665	0.01573267	-0.0063958	-0.0152222	-0.3132241	-0.377766	-1.4328731	-1.7488927	0.61388757	0.1737272
Left VS4	Ipsi	-0.0220647	0.11407278	0.09717665	-0.0167726	-0.0063958	0.01132063	-0.3132241	0.37776603	-1.4328731	1.74889269	0.61388757	-0.1737272
Right VS5	Ipsi	-0.0152998	-0.0734426	0.04950957	0.01280955	-0.0101274	-0.0094314	-0.1959347	-0.3875498	-1.385076	-1.8757939	0.31767014	0.06754309
Left VS5	Ipsi	-0.0152998	0.07234067	0.04950957	-0.0134732	-0.0101274	0.00726588	-0.1959347	0.38754983	-1.385076	1.87579395	0.31767014	-0.0675431
Right VS6	Ipsi	-0.0058373	-0.1076537	0.00659499	-0.0045877	-0.0038653	-0.0026921	-0.207367	-0.4017748	-1.4019796	-1.9089742	0.06718652	0.18736051
Left VS6	Ipsi	-0.0058373	0.1063635	0.00659499	0.00389919	-0.0038653	0.00016655	-0.207367	0.40177483	-1.4019796	1.9089742	0.06718652	-0.1873605
Right VS7	Ipsi	0.01249992	-0.0771263	-0.1544921	-0.0256496	-0.0040131	0.00373615	-0.0716578	-0.3722382	-1.3038369	-1.8315743	-0.6962343	0.06658027
Left VS7	Ipsi	0.01249992	0.07632315	-0.1544921	0.02524655	-0.0040131	-0.0053042	-0.0716578	0.37223819	-1.3038369	1.83157431	-0.6962343	-0.0665803
Right VS8	Ipsi	0.01505832	-0.0176987	-0.2970213	-0.04707	-0.0016574	-0.0008983	0.13583912	-0.4589695	-1.0575163	-1.5301519	-1.2797739	-0.0724751
Left VS8	Ipsi	0.01505832	0.01739919	-0.2970213	0.04706609	-0.0016574	0.00030509	0.13583912	0.45896946	-1.0575163	1.5301519	-1.2797739	0.07247508
Right VS9	Ipsi	0.02402611	-0.0541858	-0.3387404	-0.0579321	0.00752465	-0.0070373	0.09086186	-0.4090541	-1.0338986	-1.4135953	-1.415122	0.13275064
Left VS9	Ipsi	0.02402611	0.0523691	-0.3387404	0.05726866	0.00752465	0.00342947	0.09086186	0.40905407	-1.0338986	1.41359531	-1.415122	-0.1327506
Right VS10	Ipsi	0.00094774	-0.0235793	-0.3668407	-0.0643395	0.0032785	-0.0053048	0.19810219	-0.2681761	-0.9964607	-1.2381653	-1.6187131	-0.0305348
Left VS10	Ipsi	0.00094774	0.02336926	-0.3668407	0.06434805	0.0032785	0.00489196	0.19810219	0.26817613	-0.9964607	1.23816534	-1.6187131	0.03053482

***Table 8**: Estimated directional template state encoding (output* **C** *matrix) for the 'both' versions of LPTC directional templates provided by Holger Krapp*

		x	y	z	phi	theta	psi	u	v	w	p	q	r
Right HSS	both	0.10727519	0.31723989	0.35136379	0.03903558	-0.0159802	-0.0069963	1.14658748	-0.5377429	-0.2360391	0.09902626	0.84393589	-1.2313329
Left HSS	both	0.10727519	-0.3068461	0.35136379	-0.0339326	-0.0159802	0.02755297	1.14658748	0.53774288	-0.2360391	-0.0990263	0.84393589	1.2313329
Right HSN	both	0.08048664	0.47654044	-0.1411857	0.00554858	0.00614413	-0.0464275	0.7717888	-0.7933156	-0.1877815	-0.2881116	-0.5531605	-1.9549535
Left HSN	both	0.08048664	-0.4685051	-0.1411857	-0.0020274	0.00614413	0.06232763	0.7717888	0.79331558	-0.1877815	0.28811156	-0.5531605	1.95495349
Right HSE	both	0.03926592	0.68934569	-0.0360586	-0.0087597	0.00042865	-0.0221765	0.61535119	-0.6841131	-0.3404321	0.22861651	-0.1016664	-2.3072683
Left HSE	both	0.03926592	-0.6816181	-0.0360586	0.01193452	0.00042865	0.03747595	0.61535119	0.68411306	-0.3404321	-0.2286165	-0.1016664	2.30726826
Right DCH	both	-0.0136771	0.5460975	-0.2488803	-0.0391887	0.00563073	-0.024658	0.24363325	-0.6912262	-0.6530931	-0.7242296	-0.882191	-1.9480589
Left DCH	both	-0.0136771	-0.5455952	-0.2488803	0.03971601	0.00563073	0.02565056	0.24363325	0.69122621	-0.6530931	0.72422965	-0.882191	1.94805894
Right VCH	both	-0.0174162	0.60737842	0.16570591	0.02243303	0.0137944	-0.0279301	0.24502126	-0.3954315	-0.6663839	0.91823139	0.91488015	-1.9612241
Left HCH	both	-0.0174162	-0.6029508	0.16570591	-0.0207571	0.0137944	0.03671418	0.24502126	0.39543152	-0.6663839	-0.9182314	0.91488015	1.96122406
Right V1	both	-0.0048383	-0.1198591	0.29551421	0.04847918	0.01164619	-0.0069358	-0.3314295	-0.1421689	-1.0728701	-1.187158	1.58181407	0.30776514
Left V1	both	-0.0048383	0.11954692	0.29551421	-0.0489526	0.01164619	0.00634215	-0.3314295	0.14216886	-1.0728701	1.18715805	1.58181407	-0.3077651
Right VS1	both	-0.0251345	-0.2495711	0.33238134	0.05431036	0.02242348	-0.0046598	-0.7848231	0.12345659	-0.8996012	-0.3362501	1.63258022	0.81892687
Left VS1	both	-0.0251345	0.24383362	0.33238134	-0.0574321	0.02242348	-0.006689	-0.7848231	-0.1234566	-0.8996012	0.33625014	1.63258022	-0.8189269
Right VS2	both	-0.0596318	-0.1051111	0.16266934	0.01160599	0.03754428	-0.0075457	-0.387995	-0.2616261	-1.2286628	-0.9253723	1.41250035	0.10283999
Left VS2	both	-0.0596318	0.10215989	0.16266934	-0.0130848	0.03754428	0.00170911	-0.387995	0.26162615	-1.2286628	0.9253723	1.41250035	-0.10284
Right VS3	both	-0.0613862	-0.0244695	0.17505656	0.00809706	-0.0033183	-0.0045709	-0.3735382	-0.3527447	-1.2167288	-1.4016161	1.13519408	-0.1127251
Left VS3	both	-0.0613862	0.02214939	0.17505656	-0.0094571	-0.0033183	-1.12E-05	-0.3735382	0.35274472	-1.2167288	1.40161607	1.13519408	0.1127251
Right VS4	both	-0.0199729	-0.0718254	0.09326217	-0.0093538	-0.0099188	-0.0156938	-0.3062141	-0.3740052	-1.2234597	-1.8193011	0.60801739	0.01111181
Left VS4	both	-0.0199729	0.06994325	0.09326217	0.00838561	-0.0099188	0.0119915	-0.3062141	0.37400517	-1.2234597	1.8193011	0.60801739	-0.0111118
Right VS5	both	-0.0056547	-0.0053186	0.03114549	0.00364037	-0.0127369	0.00048244	-0.0881238	-0.320868	-1.3009017	-1.9548759	0.19647536	-0.0868179
Left VS5	both	-0.0056547	0.00504047	0.03114549	-0.0038856	-0.0127369	-0.0010137	-0.0881238	0.32086799	-1.3009017	1.95487585	0.19647536	0.08681792
Right VS6	both	-0.0203336	-0.0195622	0.04340731	-0.0088365	-0.0052934	-0.0061496	-0.2216348	-0.5499852	-1.3214502	-1.9542041	0.15235153	-0.0238192
Left VS6	both	-0.0203336	0.01847955	0.04340731	0.00814329	-0.0052934	4.04E-03	-0.2216348	0.54998524	-1.3214502	1.95420407	0.15235153	0.02381924
Right VS7	both	-0.006876	0.01789767	-0.1546182	-0.0315573	-0.0015747	0.00118097	0.00680474	-0.3273769	-1.1973582	-1.8196382	-0.7840947	-0.1606036
Left VS7	both	-0.006876	-0.0188848	-0.1546182	0.03126844	-0.0015747	-0.003126	0.00680474	0.32737687	-1.1973582	1.81963816	-0.7840947	0.16060362
Right VS8	both	0.0368468	0.08057914	-0.2906181	-0.0411257	0.00896243	-0.0045346	0.22823221	-0.3683291	-0.7652795	-1.4842771	-1.4616868	-0.3861373
Left VS8	both	0.0368468	-0.0807539	-0.2906181	0.04140037	0.00896243	0.0041817	0.22823221	0.36832914	-0.7652795	1.48427713	-1.4616868	0.38613729
Right VS9	both	0.00033696	0.03813219	-0.3588999	-0.0634882	0.00435031	0.00321687	0.21186513	-0.3549164	-0.7687008	-1.4860639	-1.5149391	-0.2051768
Left VS9	both	0.00033696	-0.0383645	-0.3588999	0.06364249	0.00435031	-0.0036633	0.21186513	0.35491643	-0.7687008	1.48606388	-1.5149391	0.20517676
Right VS10	both	-0.0118834	0.14643647	-0.3287654	-0.083632	0.03619487	-0.0155851	0.18541592	-0.2918803	-0.813013	-1.1315272	-1.5904358	-0.4887111
Left VS10	both	-0.0118834	-0.1464579	-0.3287654	0.08368441	0.03619487	0.01555387	0.18541592	0.2918803	-0.813013	1.1315272	-1.5904358	0.48871107

5.2 Comparisons of LPTC directional encodings with dynamically significant directions in Calliphora

In this section, we compare the state directions associated with each LPTC receptive field with state directions that have dynamical significance for *Calliphora*. In particular, we examine correlations with (a) the natural modes of the identified dynamics and a basis for the reachable space composed of the independent columns of the controllability matrix, (b) controllability, observability and maximum joint controllability/observability directions, and disturbance sensitivity directions. The four sets of directions in (b) are generated from the geometry (singular values and vectors) of the respective gramians, hence have a natural ranking and method for comparison which is a weighted average of the correlations across their singular values. The two sets of directions in (a) do not have a corresponding ranking but can be uniformly averaged across all the correlations. We also restrict the analysis in the following sections to the ipsilateral VS cell templates and the spiking cell (V1, V2, Vx) templates.

5.2.1 Coordinate frames for the linearized flight dynamics and LPTC outputs

Using small perturbation analysis, the nonlinear periodically forced system can be reduced to a linear time invariant (LTI) set of equations as described in Section 2. Denoting coordinate frames, the resulting equations are of the form:

$$\begin{gathered}[\dot{\boldsymbol{x}}]_B(t) = \mathbf{A}[\boldsymbol{x}]_B(t) + \mathbf{B}\boldsymbol{u}(t) + \mathbf{G}\boldsymbol{d}(t) \\ \boldsymbol{y}(t) = \mathbf{C}[\boldsymbol{x}]_S(t)\end{gathered}$$

where $\mathbf{A}$ is the stability matrix, $\mathbf{B}$ is the control matrix, $\mathbf{G}$ is the disturbance matrix, $\mathbf{C}$ is the linearized output matrix. $\boldsymbol{x}$, $\boldsymbol{u}$, $\boldsymbol{d}$ and $\boldsymbol{y}$ are the vectors of vehicle states, control inputs, disturbances and outputs respectively, $[\boldsymbol{x}]_B$ is the state expressed in (principal) body 'B' coordinates, and $[\boldsymbol{x}]_S$ is the state expressed in stability 'S' coordinates (Figure 59). The matrices $\mathbf{A}$, $\mathbf{B}$ and $\mathbf{G}$ were derived previously in Section 2.2, where the linearization was performed about the animal's body (principal) 'B' axes. Therefore, these matrices are expressed relative to body coordinates. For the head (visual) axes 'H', the $\boldsymbol{x}_h$ coordinate, which points along the ray at the azimuth and elevation angle (γ, β) = (0 , 90°) in the plots in Figures 54-58, corresponds to the $\boldsymbol{x}_s$ coordinate of the stability axes 'S' (Figure 59), which is opposite the direction of the oncoming flow U_∞ (Section 3.3). Therefore, the output matrix $\mathbf{C}$ as derived in Section 5.1 is expressed relative to stability coordinates.

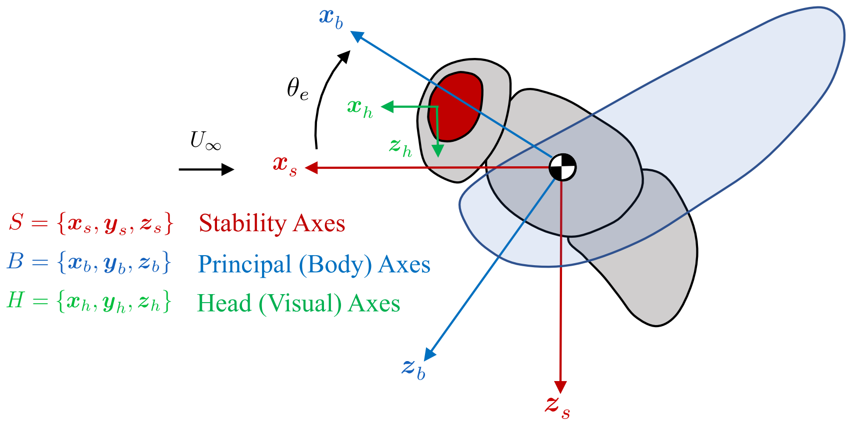

***Figure 59**: Flight dynamics and LPTC coordinate frames*

In order to compare the directions encoded by the LPTCs (rows of the $\mathbf{C}$ matrix) to dynamically significant directions from the flight dynamics ($\mathbf{A}$, $\mathbf{B}$ and $\mathbf{G}$ matrices), we need to either (i) express the $\mathbf{C}$ matrix in body 'B' coordinates, or (ii) express the $\mathbf{A}$, $\mathbf{B}$ and $\mathbf{G}$ matrices in stability 'S' coordinates. To derive these transformations, we consider the relationship between the velocity and angular velocity in these two coordinate frames, which differ by a rotation θ_e about the pitch axis (Figure 59):

$$R_{PS}(\theta_e) = \begin{pmatrix} \cos\theta_e & 0 & -\sin\theta_e \\ 0 & 1 & 0 \\ \sin\theta_e & 0 & \cos\theta_e \end{pmatrix}$$

Hence, the velocity of the animal in body coordinates $[\mathbf{v}]_B$ is related to its velocity in stability coordinates $[\mathbf{v}]_S$ via

$$[\mathbf{v}]_B = \begin{pmatrix} u_b \\ v_b \\ w_b \end{pmatrix} = R_{BS}(\theta_e)\ [\mathbf{v}]_S = \begin{pmatrix} \cos\theta_e & 0 & -\sin\theta_e \\ 0 & 1 & 0 \\ \sin\theta_e & 0 & \cos\theta_e \end{pmatrix} \begin{pmatrix} u_s \\ v_s \\ w_s \end{pmatrix}$$

Similarly, angular velocity of the animal in body coordinates $[\boldsymbol{\omega}]_B$ is related to its velocity in stability coordinates $[\boldsymbol{\omega}]_S$ via

$$[\boldsymbol{\omega}]_B = \begin{pmatrix} p_b \\ q_b \\ r_b \end{pmatrix} = R_{BS}(\theta_e)\ [\boldsymbol{\omega}]_S = \begin{pmatrix} \cos\theta_e & 0 & -\sin\theta_e \\ 0 & 1 & 0 \\ \sin\theta_e & 0 & \cos\theta_e \end{pmatrix} \begin{pmatrix} p_s \\ q_s \\ r_s \end{pmatrix}$$

The full 8-dimensional state vector also contains two attitude angles, θ and ϕ. In the linearized flight dynamics these are actually perturbation angles from equilibrium, hence $\theta_b = \theta_s$ since the $\boldsymbol{y}_b$ and $\boldsymbol{y}_s$ coordinate axes are colinear. To develop the relationship between ϕ_b and ϕ_s, we take the axis-angle form for a rotation ϕ_s about the $\boldsymbol{x}_s$ axis in the $B = \{\boldsymbol{x}_b, \boldsymbol{y}_b, \boldsymbol{z}_b\}$ corrdinate frame, convert this to its equivalent rotation matrix, then back out the equivalent 3-2-1 Euler angles $\{\phi_b, \theta_b, \psi_b\}$.

The axis-angle form is angle ϕ_s about axis $\hat{\boldsymbol{e}} = (\cos\theta_e, 0, \sin\theta_e)$, which corresponds to the rotation matrix

$$\begin{pmatrix} (1-\cos\phi_s)\cos^2\theta_e + \cos\phi_s & \sin\theta_e \sin\phi_s & (1-\cos\phi_s)\cos\theta_e\sin\theta_e \\ \sin\theta_e\sin\phi_s & \cos\phi_s & -\cos\theta_e\sin\phi_s \\ (1-\cos\phi_s)\cos\theta_e\sin\theta_e & \cos\theta_e\sin\phi_s & (1-\cos\phi_s)\sin^2\theta_e + \cos\phi_s \end{pmatrix}$$

If we parameterize this rotation using 3-2-1 Euler angles $\{\phi_b, \theta_b, \psi_b\}$, we have

$$\begin{pmatrix} \cos\psi_b\cos\theta_b & * & * \\ \sin\psi_b\cos\theta_b & * & * \\ -\sin\theta_b & \cos\theta_b\sin\phi_b & \cos\theta_b\cos\phi_b \end{pmatrix}$$

where the '$*$' entries are not needed. If we equate these representations, from the (3,1) entry, we have

$$-\sin\theta_b = (1-\cos\phi_s)\cos\theta_e\sin\theta_e$$

For small ϕ_s and small θ_b, this reduces to $\theta_b \approx 0$. Next, from the ratio of the (2,1) and (1,1) entries, we have

$$\tan\psi_b = \frac{\sin\theta_e\sin\phi_s}{(1-\cos\phi_s)\cos^2\theta_e + \cos\phi_s}$$

For small ϕ_s and small ψ_b, this reduces to $\psi_b \approx \sin\theta_e\ \phi_s$. Similarly, with the (3,2) and (3,3) entries, we have

$$\tan\phi_b = \frac{\cos\theta_e \sin\phi_s}{(1-\cos\phi_s)\sin^2\theta_e + \cos\phi_s}$$

Hence for small $\boldsymbol{\phi_s}$ and small $\boldsymbol{\phi_b}$, this reduces to $\boldsymbol{\phi_b \approx \cos\theta_e\, \phi_s}$.

Therefore, the longitudinal state transformation from stability to body axes $\left[\boldsymbol{x}_{\text{long}}\right]_B = R_{\text{long}} \left[\boldsymbol{x}_{\text{long}}\right]_S$ is given by

$$\begin{pmatrix} u_b \\ w_b \\ q_b \\ \theta_b \end{pmatrix} = \begin{pmatrix} \cos\theta_e & -\sin\theta_e & 0 & 0 \\ \sin\theta_e & \cos\theta_e & 0 & 0 \\ 0 & 0 & 1 & 0 \\ 0 & 0 & 0 & 1 \end{pmatrix} \begin{pmatrix} u_s \\ w_s \\ q_s \\ \theta_s \end{pmatrix}$$

And the lateral state transformation from stability to body axes $[\boldsymbol{x}_{\text{lat}}]_B = R_{\text{lat}}\, [\boldsymbol{x}_{\text{lat}}]_S$ is given by

$$\begin{pmatrix} v_b \\ p_b \\ \phi_b \\ r_b \end{pmatrix} = \begin{pmatrix} 1 & 0 & 0 & 0 \\ 0 & \cos\theta_e & 0 & -\sin\theta_e \\ 0 & 0 & \cos\theta_e & 0 \\ 0 & \sin\theta_e & 0 & \cos\theta_e \end{pmatrix} \begin{pmatrix} v_s \\ p_s \\ \phi_s \\ r_s \end{pmatrix}$$

The combined transformation for the full state $[\boldsymbol{x}]_B = R\, [\boldsymbol{x}]_S$ (longitudinal and lateral states combined) is

$$R = \begin{pmatrix} R_{\text{long}} & 0 \\ 0 & R_{\text{lat}} \end{pmatrix}$$

To express the $\mathbf{C}$ matrix relative to body 'B' coordinates, we consider the output equation in stability coordinates $\boldsymbol{y} = \mathbf{C}\, [\boldsymbol{x}]_S$ from Section 5.1 and substitute $[\boldsymbol{x}]_S = R^{-1}[\boldsymbol{x}]_B$,

$$\boldsymbol{y} = \mathbf{C}[\boldsymbol{x}]_S = \mathbf{C}R^{-1}[\boldsymbol{x}]_B$$

Hence, the $\mathbf{C}$ matrix expressed relative to body 'B' coordinates is given by $\tilde{\mathbf{C}} = \mathbf{C}R^{-1}$.

Similarly, to express the $\mathbf{A}$, $\mathbf{B}$ and $\mathbf{G}$ matrices relative to stability 'S' coordinates, we substitute $[\boldsymbol{x}]_B = R\, [\boldsymbol{x}]_S$ and $[\dot{\boldsymbol{x}}]_S = R^{-1}[\dot{\boldsymbol{x}}]_B$ into the dynamics $[\dot{\boldsymbol{x}}]_B = \mathbf{A}[\boldsymbol{x}]_B + \mathbf{B}\boldsymbol{u} + \mathbf{G}\boldsymbol{d}$ to arrive at

$$[\dot{\boldsymbol{x}}]_S = R^{-1}\mathbf{A}R[\boldsymbol{x}]_S + R^{-1}\mathbf{B}\boldsymbol{u} + R^{-1}\mathbf{G}\boldsymbol{d}$$

Hence, the $\mathbf{A}$, $\mathbf{B}$ and $\mathbf{G}$ matrices expressed relative to stability 'S' coordinates are given by $\widetilde{\mathbf{A}} = R^{-1}\mathbf{A}R$, $\widetilde{\mathbf{B}} = R^{-1}\mathbf{B}$ and $\widetilde{\mathbf{G}} = R^{-1}\mathbf{G}$.

5.2.2 Natural Modes and Columns of the Controllability Matrix

To quantify the degree of alignment of *Calliphora* LPTC templates to their natural modes, we compute the absolute value of the normalized inner product of the unit eigenvectors $\mathbf{v}_j$ the 8 modes

(4 longitudinal, 4 lateral) with the rows $\mathbf{c}_i$ of the $\mathbf{C}$ matrix (recall each row of $\mathbf{C}$ corresponds to a particular LPTC template).

$$\kappa_{ij} = \frac{1}{\|\mathbf{c}_i\|} |\langle \mathbf{c}_i, \mathbf{v}_j \rangle|$$

Hence, if mode $\mathbf{v}_j$ is unobservable with LPTC template $\mathbf{c}_i$, then $\kappa_{ij} = 0$ and if LPTC template $\mathbf{c}_i$ is perfectly tuned to mode $\mathbf{v}_j$, then $\kappa_{ij} = 1$. In Figures 63-66 (VS cells) and Figures 67-70 (spiking cells) we plot four cases: (i) each individual same-side (ipsilateral) LPTC template; (ii) the sum of same-type left and right hemisphere templates; and (iii) the difference of same-type left and right hemisphere templates, and (iv) the maximum correlations over the sum and difference of same-type left and right hemispheres for each direction $\mathbf{v}_j$. Note that in these figures, it is clear that the sum of same-type left and right hemisphere templates corresponds to the first four (longitudinal, symmetric) modes and the difference of same-type left and right hemisphere templates corresponds to the last four (lateral, asymmetric) modes.

The span (independent columns) of the controllability matrix

$$\mathcal{C} = [\,\mathbf{B}\ \ \mathbf{AB}\ \ \mathbf{A}^2\mathbf{B}\ \ \cdots\ \ \mathbf{A}^{n-1}\mathbf{B}\,]$$

or the range $R(\mathcal{C})$, provide a *basis for the set of reachable states*. Similarly, to quantify the degree of alignment of *Calliphora* LPTC templates with this basis, we compute the absolute value of the normalized inner product of the independent columns $\mathbf{w}_j$ the controllability matrix with the rows $\mathbf{c}_i$ of the $\mathbf{C}$ matrix (recall each row of $\mathbf{C}$ corresponds to a particular LPTC template):

$$\kappa_{ij} = \frac{1}{\|\mathbf{c}_i\|\|\mathbf{w}_j\|} |\langle \mathbf{c}_i, \mathbf{w}_j \rangle|$$

Hence, if basis vector $\mathbf{w}_j$ is unobservable with LPTC template $\mathbf{c}_i$, then $\kappa_{ij} = 0$ and if LPTC template $\mathbf{c}_i$ is perfectly tuned to basis vector $\mathbf{w}_j$, then $\kappa_{ij} = 1$. In Figures 63-66 (VS cells) and Figures 67-70 (spiking cells) we plot four cases: (i) each individual same-side (ipsilateral) LPTC template; (ii) the sum of same-type left and right hemisphere templates; and (iii) the difference of same-type left and right hemisphere templates, and (iv) the maximum correlations over the sum and difference of same-type left and right hemispheres for each direction $\mathbf{w}_j$.

5.2.3 Controllability, observability and disturbance sensitivity directions

In the following we consider the various gramians of the dynamics constructed from the matrices $\mathbf{A}$, $\mathbf{B}$, $\mathbf{G}$ and $\mathbf{C}$, whose geometric structure (singular values and vectors) provide additional insight into dynamically significant directions in state space for the animal. We note that the identified dynamics in the longitudinal and lateral directions (Section 2) are unstable, so in order to compute these we consider the generalization of the gramian presented in Zhou et al., 1999 for unstable systems.

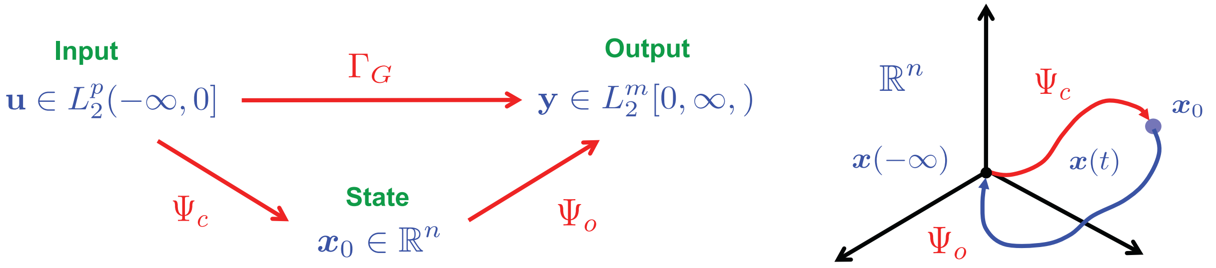

Figure 60: *Relationship between the controllability, observability and Hankel operators*

First, consider the 'input to state' map $\Psi_c: L_2^p(-\infty, 0] \longrightarrow \mathbb{R}^n$, whose action is

$$\Psi_c : \mathbf{u}(t) \rightarrow \int_{-\infty}^{0} e^{-\mathbf{A}\tau}\mathbf{B}\mathbf{u}(\tau)\, d\tau$$

This defines a map $\boldsymbol{x}_0 = \Psi_c\mathbf{u}$ from past inputs $\mathbf{u}(\mathrm{t}) \in L_2^p(-\infty, 0]$ to the state $\boldsymbol{x}_0$ of the system (Figure 60). To quantify the minimum amount of energy it takes to reach an arbitrary state $\boldsymbol{x}_0$, we calculate the minimum norm solution to $\boldsymbol{x}_0 = \Psi_c\mathbf{u}$ using least squares,

$$\mathbf{u}_{\mathrm{opt}}(t) = \Psi_c^*(\Psi_c\Psi_c^*)^{-1}\boldsymbol{x}_0 = \Psi_c^* X_c^{-1}\boldsymbol{x}_0$$

where the *controllability gramian* $X_c = \Psi_c\Psi_c^*$ is computed from the **A** and **B** matrix (Zhou et al., 1999) as:

$$X_c = \frac{1}{2\pi}\int_{-\infty}^{\infty} (j\omega I - \mathbf{A})^{-1}\mathbf{B}\mathbf{B}^*(-j\omega I - \mathbf{A}^*)^{-1}\, d\omega$$

Note that $X_c = \Psi_c\Psi_c^*$ is invertible if the pair $(\mathbf{A}, \mathbf{B})$ is controllable. The minimum energy required to drive the system to state $\boldsymbol{x}_0 \in \mathbb{R}^n$ is then

$$\begin{aligned}\|\mathbf{u}_{\mathrm{opt}}\|_2^2 &= \langle \Psi_c^* X_c^{-1}\boldsymbol{x}_0, \Psi_c^* X_c^{-1}\boldsymbol{x}_0\rangle \\ &= \langle X_c^{-1}\boldsymbol{x}_0, \Psi_c\Psi_c^* X_c^{-1}\boldsymbol{x}_0\rangle \\ &= \boldsymbol{x}_0^* X_c^{-1}\boldsymbol{x}_0\end{aligned}$$

To provide a geometric interpretation for X_c, consider the set of states reachable with a fixed amount of input energy, $\mathcal{E}_c = \{\, \Psi_c\mathbf{u}\text{: } \|\mathbf{u}\|_2 \leq 1 \,\}$. From the above calculation, this set is given by

$$\mathcal{E}_c = \{\boldsymbol{x}_0^* X_c^{-1}\boldsymbol{x}_0 \leq 1,\ \boldsymbol{x}_0 \in \mathbb{R}\}$$

which is equivalent to (Dullerud and Paganini, 2000),

$$\mathcal{E}_c = \{X_c^{\frac{1}{2}}\boldsymbol{x}_c : \boldsymbol{x}_c \in \mathbb{R}^n, \|\boldsymbol{x}_c\| = 1\}$$

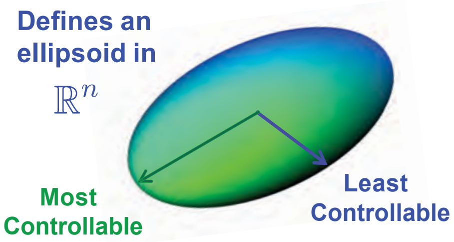

***Figure 61**: Controllability ellipsoid*

The above set defines an ellipsoid (Figure 61) whose axes lengths and directions are given by the singular values σ_j and singular vectors $\mathbf{u}_j$ of the controllability gramian X_c. These directions are typically ranked according to their respective singular values (axis lengths) and have the interpretation of the *optimal actuation inputs in the sense that they describe directions in state space that require the minimum control energy*, i.e., the *most maneuverable or reachable directions in state space*, or the directions in which the animal is most likely to move.

Note that these directions are different than the basis for the set of reachable states derived from the independent columns of the controllability matrix (Section 5.2.2) since there is an energy cost associated with each.

To quantify the degree of alignment of *Calliphora* LPTC templates to these controllability directions, we compute the absolute value of the normalized inner product of the unit singular vectors $\mathbf{u}_j$ of the controllability gramian X_c with the rows $\mathbf{c}_i$ of the $\mathbf{C}$ matrix:

$$\kappa_{ij} = \frac{1}{\|\mathbf{c}_i\|} |\langle \mathbf{c}_i, \mathbf{u}_j \rangle|$$

Hence, if controllability direction $\mathbf{u}_j$ is unobservable with LPTC template $\mathbf{c}_i$, then $\kappa_{ij} = 0$ and if LPTC template $\mathbf{c}_i$ is perfectly tuned to controllability direction $\mathbf{u}_j$, then $\kappa_{ij} = 1$. In Figures 63-66 (VS cells) and Figures 67-70 (spiking cells) we plot four cases: (i) each individual same-side (ipsilateral) LPTC template; (ii) the sum of same-type left and right hemisphere templates; and (iii) the difference of same-type left and right hemisphere templates, (iv) the maximum correlations over the sum and difference of same-type left and right hemispheres for each direction $\mathbf{u}_j$.

Next, consider the 'state to output' map $\Psi_0 \colon \mathbb{R}^n \longrightarrow L_2^m[0,\infty)$, whose action is

$$\Psi_0 : \boldsymbol{x}_0 \to \mathbf{C}e^{\mathbf{A}t}\boldsymbol{x}_0$$

This defines a map $\boldsymbol{y} = \Psi_0 \boldsymbol{x}_0$ from the initial state $\boldsymbol{x}_0$ to the output time history $\boldsymbol{y}(t) = \mathbf{C}e^{\mathbf{A}t}\boldsymbol{x}_0$, $t \geq 0$ (Figure 60). To quantify the degree of observability of a particular direction $\boldsymbol{x}_0$ in state space, we compute the energy of its image $\boldsymbol{y}(t)$ under Ψ_0, which is given by

$$\begin{aligned} \|\boldsymbol{y}\|^2_{L_2^m([0,\infty)} &= \langle \Psi_0 \boldsymbol{x}_0, \Psi_0 \boldsymbol{x}_0 \rangle_{L_2^m([0,\infty)} \\ &= \langle \boldsymbol{x}_0, \Psi_0^* \Psi_0 \boldsymbol{x}_0 \rangle_{\mathbb{R}^n} \\ &= \langle \boldsymbol{x}_0, Y_o \boldsymbol{x}_0 \rangle_{\mathbb{R}^n} \\ &= \|Y_o^{\frac{1}{2}} \boldsymbol{x}_0\|^2_{\mathbb{R}^n} \end{aligned}$$

$Y_o = \Psi_0^* \Psi_0$ is called the *observability gramian*, is computed from the $\mathbf{A}$ and $\mathbf{C}$ matrix (Zhou et al., 1999) as:

$$Y_o = \frac{1}{2\pi} \int_{-\infty}^{\infty} (-j\omega I - \mathbf{A}^*)^{-1} \mathbf{C}^* \mathbf{C} (j\omega I - \mathbf{A})^{-1} \, d\omega$$

The observability gramian defines an ellipsoid $\mathcal{E}_o$ in state space,

$$\mathcal{E}_o = \{ Y_o^{\frac{1}{2}} \boldsymbol{x}_0 : \boldsymbol{x}_0 \in \mathbb{R}^n, \|\boldsymbol{x}_0\| = 1 \}$$

whose axes lengths and directions are given by the singular values σ_j and singular vectors $\mathbf{u}_j$ of the observability gramian Y_o. These directions $\mathbf{u}_j$ are typically ranked according to their respective singular values σ_j (axis lengths) and have the interpretation of *the optimal sensor outputs in the sense that they exhibit the most energy in the signal* $\boldsymbol{y}(t)$, and equivalently *minimize the estimate covariance* (or maximize the Fisher information).

To quantify the degree of alignment of *Calliphora* LPTC templates to these observability directions, we compute the absolute value of the normalized inner product of the unit singular vectors $\mathbf{u}_j$ of the observability gramian Y_o with the rows $\mathbf{c}_i$ of the $\mathbf{C}$ matrix:

$$\kappa_{ij} = \frac{1}{\|\mathbf{c}_i\|} |\langle \mathbf{c}_i, \mathbf{u}_j \rangle|$$

Hence, if observability direction $\mathbf{u}_j$ is unobservable with LPTC template $\mathbf{c}_i$, then $\kappa_{ij} = 0$ and if LPTC template $\mathbf{c}_i$ is perfectly tuned to observability direction $\mathbf{u}_j$, then $\kappa_{ij} = 1$. In Figures 63-66 (VS cells) and Figures 67-70 (spiking cells) we plot four cases: (i) each individual same-side (ipsilateral) LPTC template; (ii) the sum of same-type left and right hemisphere templates; and (iii) the difference of same-type left and right hemisphere templates, (iv) the maximum correlations over the sum and difference of same-type left and right hemispheres for each direction $\mathbf{u}_j$.

Last, if we consider the 'disturbance to state' map $\Psi_c: L_2^r(-\infty, 0] \longrightarrow \mathbb{R}^n$, whose action is

$$\Psi_d : \mathbf{d}(t) \to \int_{-\infty}^{0} e^{-\mathbf{A}\tau} \mathbf{G} \mathbf{d}(\tau) \, d\tau$$

This defines a map $\boldsymbol{x}_0 = \Psi_d \mathbf{d}$ from past disturbances $\mathbf{d}(\mathrm{t}) \in L_2^r(-\infty, 0]$ to the state $\boldsymbol{x}_0$ of the system. This formulation is equivalent to the controllability case where the input $\mathbf{u}(\mathrm{t})$ is replaced with the external disturbance $\mathbf{d}(\mathrm{t})$. All the previous results follow. In particular, the *disturbance sensitivity gramian* is computed from the $\mathbf{A}$ and $\mathbf{G}$ matrix as follows:

$$X_d = \frac{1}{2\pi} \int_{-\infty}^{\infty} (j\omega I - \mathbf{A})^{-1} \mathbf{G} \mathbf{G}^* (-j\omega I - \mathbf{A}^*)^{-1} \, d\omega$$

which defines an ellipsoid $\mathcal{E}_d$ in state space,

$$\mathcal{E}_d = \{X_d^{\frac{1}{2}} \boldsymbol{x}_d : \boldsymbol{x}_d \in \mathbb{R}^n, \|\boldsymbol{x}_d\| = 1\}$$

whose axes lengths and directions are given by the singular values σ_j and singular vectors $\mathbf{u}_j$ of the disturbance sensitivity gramian X_d. These directions are typically ranked according to their respective singular values (axis lengths) and have the interpretation of the *worst-case disturbance directions, i.e., the combination of disturbance states that create the largest perturbations from equilibrium*.

To quantify the degree of alignment of *Calliphora* LPTC templates to these disturbance sensitivity directions, we compute the absolute value of the normalized inner product of the unit singular vectors $\mathbf{u}_j$ of the disturbance sensitivity gramian X_d with the rows $\mathbf{c}_i$ of the $\mathbf{C}$ matrix:

$$\kappa_{ij} = \frac{1}{\|\mathbf{c}_i\|} |\langle \mathbf{c}_i, \mathbf{u}_j \rangle|$$

Hence, if disturbance direction $\mathbf{u}_j$ is unobservable with LPTC template $\mathbf{c}_i$, then $\kappa_{ij} = 0$ and if LPTC template $\mathbf{c}_i$ is perfectly tuned to disturbance direction $\mathbf{u}_j$, then $\kappa_{ij} = 1$. In Figures 63-66 (VS cells) and Figures 67-70 (spiking cells) we plot four cases: (i) each individual same-side (ipsilateral) LPTC template; (ii) the sum of same-type left and right hemisphere templates; and (iii) the difference of same-type left and right hemisphere templates, (iv) the maximum correlations over the sum and difference of same-type left and right hemispheres for each direction $\mathbf{u}_j$.

5.2.4 Combined controllability/observability directions

Another possibility for the specification of the LPTC template characteristics is that the directions are chosen such that the *sensing directions and actuation directions are simultaneously optimized*. A system where this is the driving principle is optimal in the sense that it would *transfer the maximum amount of energy from the input to the output*. This can be quantified by the *Hankel operator*,

$$\Gamma_G : \mathbf{u} \rightarrow \mathbf{y}$$

which is given by the composition $\Gamma_G = \Psi_o \Psi_c$, and maps past inputs to future outputs (Figure 62). To understand which directions in state space have the largest joint controllability/observability, we balance the system by computing a state transformation $\boldsymbol{z} = \mathbf{T}\boldsymbol{x}$ that simultaneously diagonalizes the controllability and observability gramians (Figure 60).

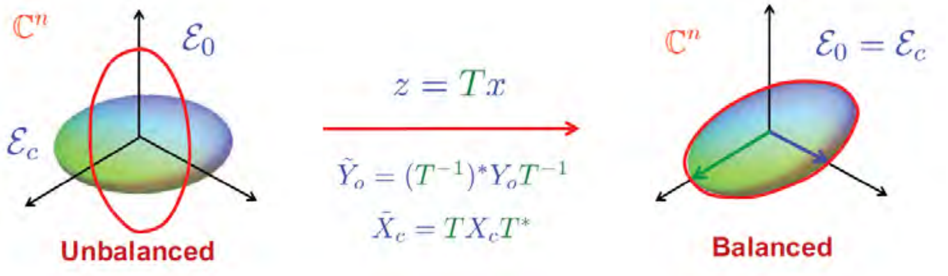

Figure 62: *Simultaneous diagonalization of the controllability and observability gramians*

In transformed coordinates, the gramians become

$$\tilde{X}_c = \tilde{Y}_o = \Sigma = \begin{bmatrix} h_1 & & \\ & \ddots & \\ & & h_n \end{bmatrix}$$

where the diagonal entries $h_i = \sqrt{\lambda_i(Y_o X_c)}$ are the Hankel singular values. These are similarity invariants that can be used to quantify the importance of each state in the corresponding input-output system (Moore, 1980). In particular, h_i ranks the combined controllability and observability in the direction $\hat{\boldsymbol{e}}_i$ of the transformed system. Hence, the most controllable/observable direction is $\boldsymbol{z} = \hat{\boldsymbol{e}}_1$, which corresponds to the direction $\boldsymbol{x} = \mathbf{T}^{-1}\hat{\boldsymbol{e}}_1$ in original coordinates. Therefore, the columns of the matrix $\mathbf{T}^{-1}$ provide the directions for comparison in the original coordinates.

To quantify the degree of alignment of LPTC templates to these directions, we compute the normalized inner product of the 8 columns of the matrix $\mathbf{T}^{-1}$ with the rows $\mathbf{c}_i$ of the $\mathbf{C}$ matrix:

$$\kappa_{ij} = \frac{1}{\|\mathbf{c}_i\|} |\langle \mathbf{c}_i, \mathbf{T}_j^{-1} \rangle|$$

Hence, if controllability/observability direction $\mathbf{T}_j^{-1}$ is orthogonal to LPTC template $\mathbf{c}_i$, then $\kappa_{ij} = 0$ and if LPTC template $\mathbf{c}_i$ is perfectly tuned to controllability/observability direction T_j^{-1}, then $\kappa_{ij} = 1$. In Figures 63-66 (VS cells) and Figures 67-70 (spiking cells) we plot four cases: (i) each individual same-side (ipsilateral) LPTC template; (ii) the sum of same-type left and right hemisphere templates; and (iii) the difference of same-type left and right hemisphere templates, and (iv) the maximum correlations over the sum and difference of same-type left and right hemispheres for each direction $\mathbf{u}_j$.

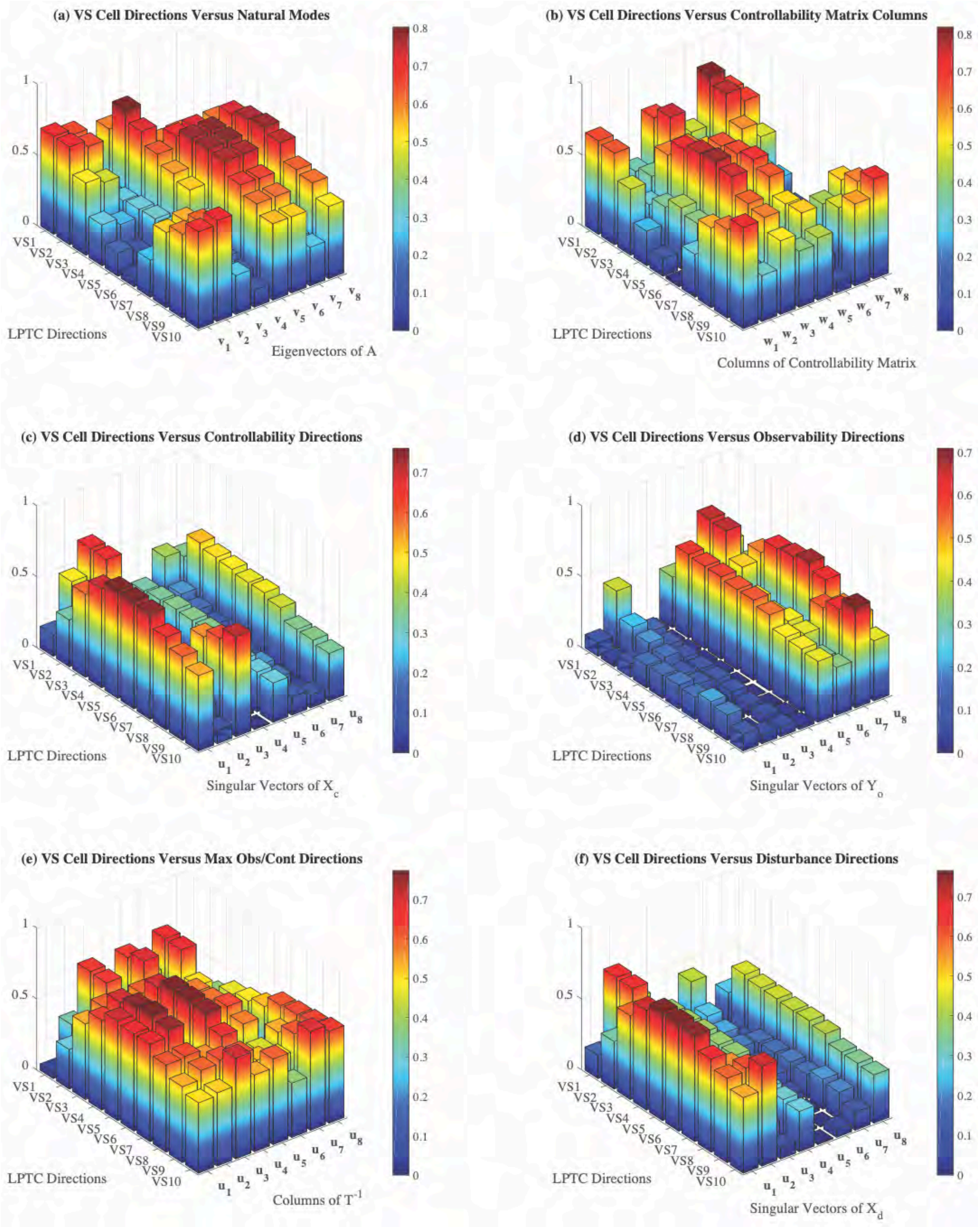

(a) VS Cell Directions Versus Natural Modes

(b) VS Cell Directions Versus Controllability Matrix Columns

(c) VS Cell Directions Versus Controllability Directions

(d) VS Cell Directions Versus Observability Directions

(e) VS Cell Directions Versus Max Obs/Cont Directions

(f) VS Cell Directions Versus Disturbance Directions

Figure 63: *VS cell (ipsilateral side only) correlations with dynamically significant directions; (a) natural modes, (b) independent columns of the controllability matrix, (c) controllability gramian, (d) observability gramian, (e) joint cont/obs, (f) disturbance sensitivity.*

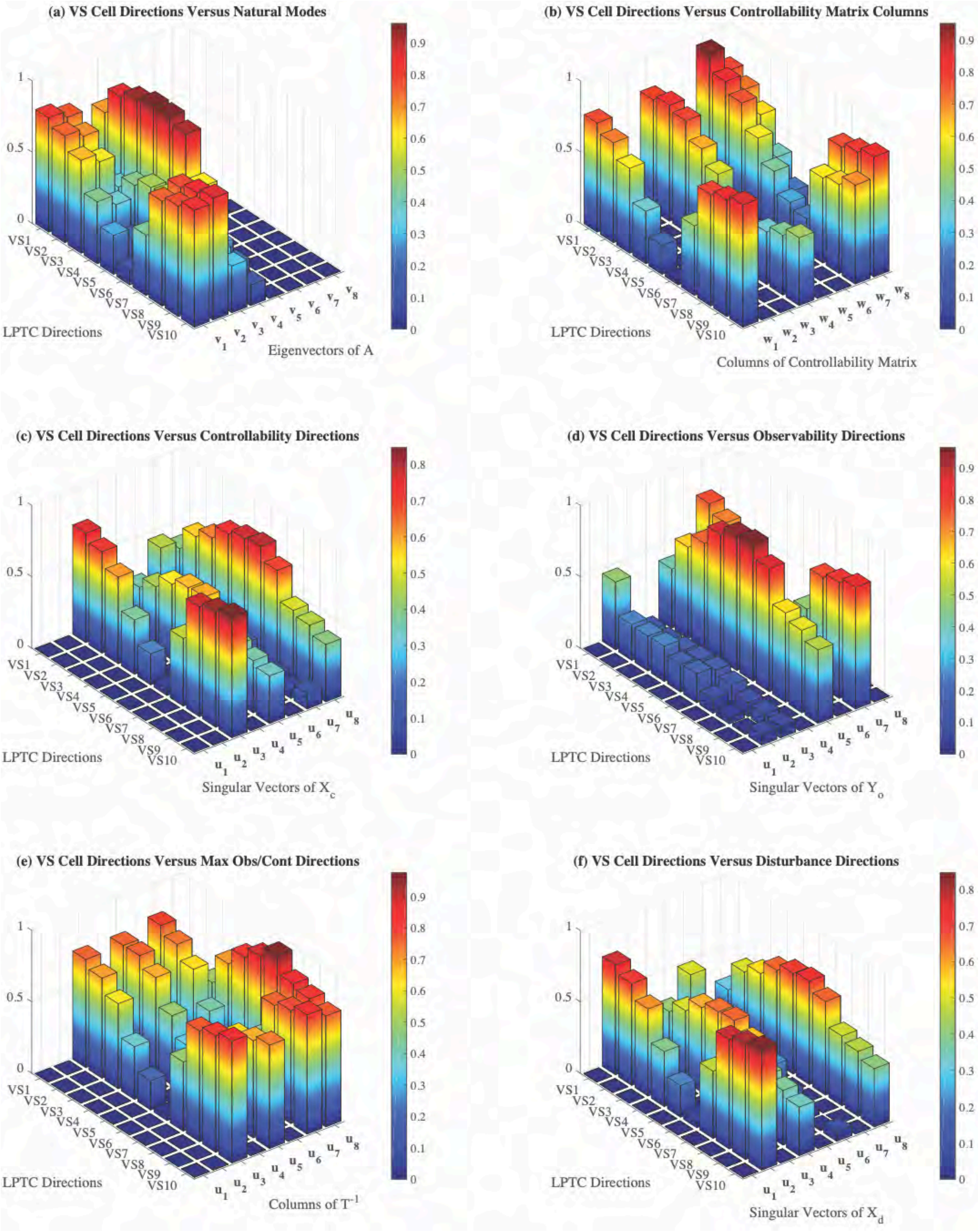
(a) VS Cell Directions Versus Natural Modes

(b) VS Cell Directions Versus Controllability Matrix Columns

(c) VS Cell Directions Versus Controllability Directions

(d) VS Cell Directions Versus Observability Directions

(e) VS Cell Directions Versus Max Obs/Cont Directions

(f) VS Cell Directions Versus Disturbance Directions

Figure 64: *VS cell (right plus left) correlations with dynamically significant directions; (a) natural modes, (b) independent columns of the controllability matrix, (c) controllability gramian, (d) observability gramian, (e) joint cont/obs, (f) disturbance sensitivity.*

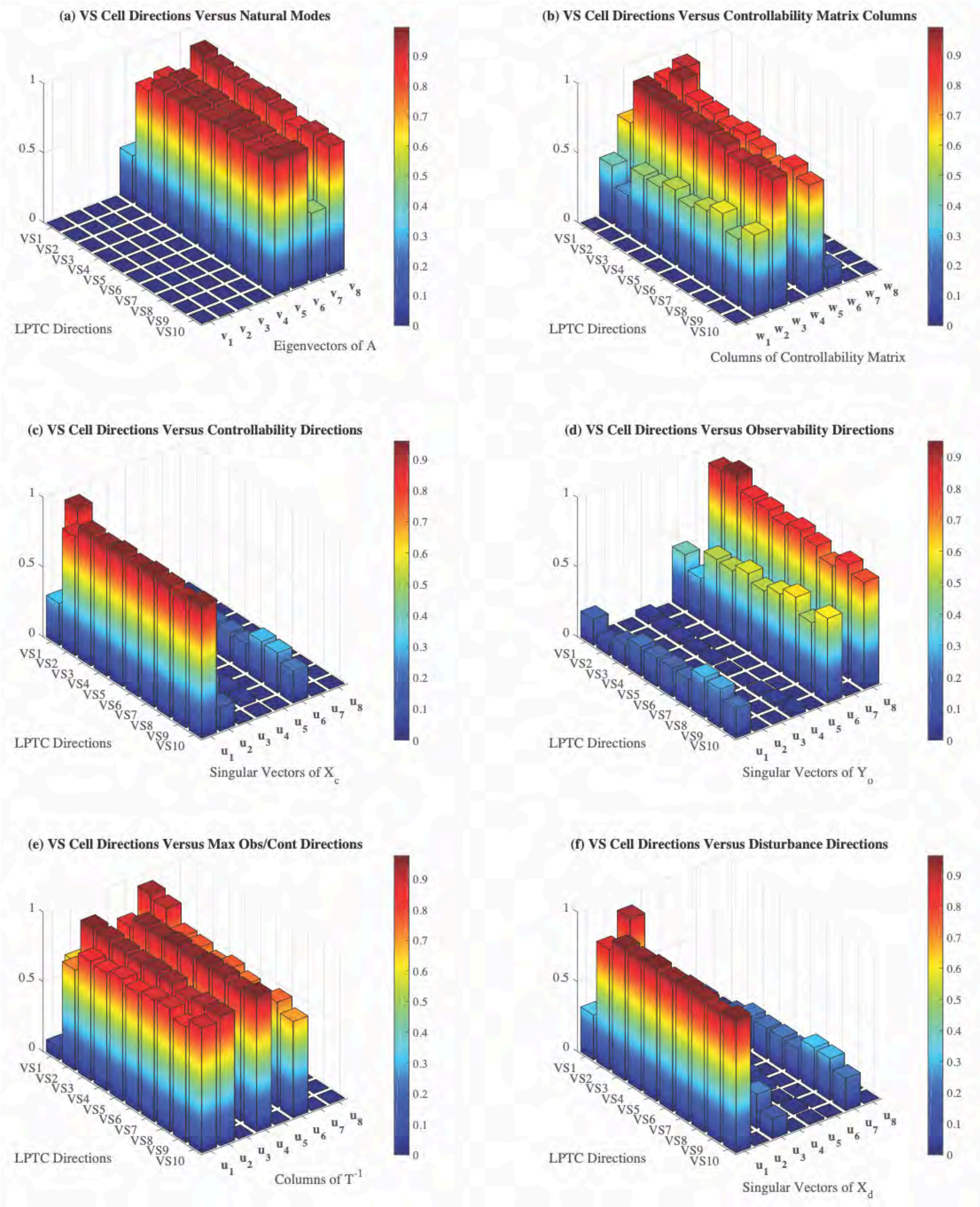
(a) VS Cell Directions Versus Natural Modes

(b) VS Cell Directions Versus Controllability Matrix Columns

(c) VS Cell Directions Versus Controllability Directions

(d) VS Cell Directions Versus Observability Directions

(e) VS Cell Directions Versus Max Obs/Cont Directions

(f) VS Cell Directions Versus Disturbance Directions

Figure 65*: VS cell (right minus left) correlations with dynamically significant directions; (a) natural modes, (b) independent columns of the controllability matrix, (c) controllability gramian, (d) observability gramian, (e) joint cont/obs, (f) disturbance sensitivity.*

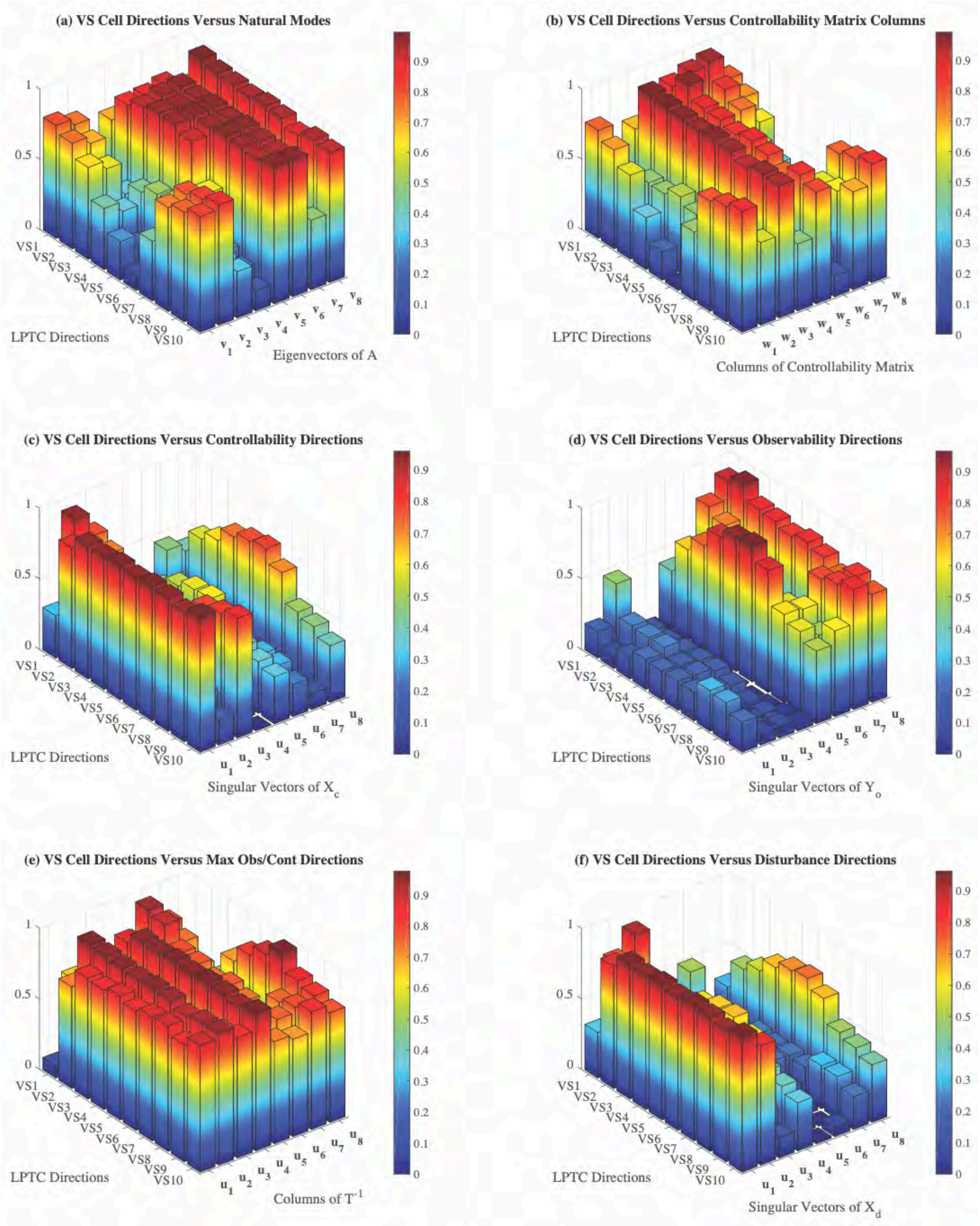

Figure 66: *VS cell (maximum over right plus left and right minus left cases) correlations with dynamically significant directions; (a) natural modes, (b) independent columns of the controllability matrix, (c) controllability gramian, (d) observability gramian, (e) joint cont/obs, (f) disturbance sensitivity.*

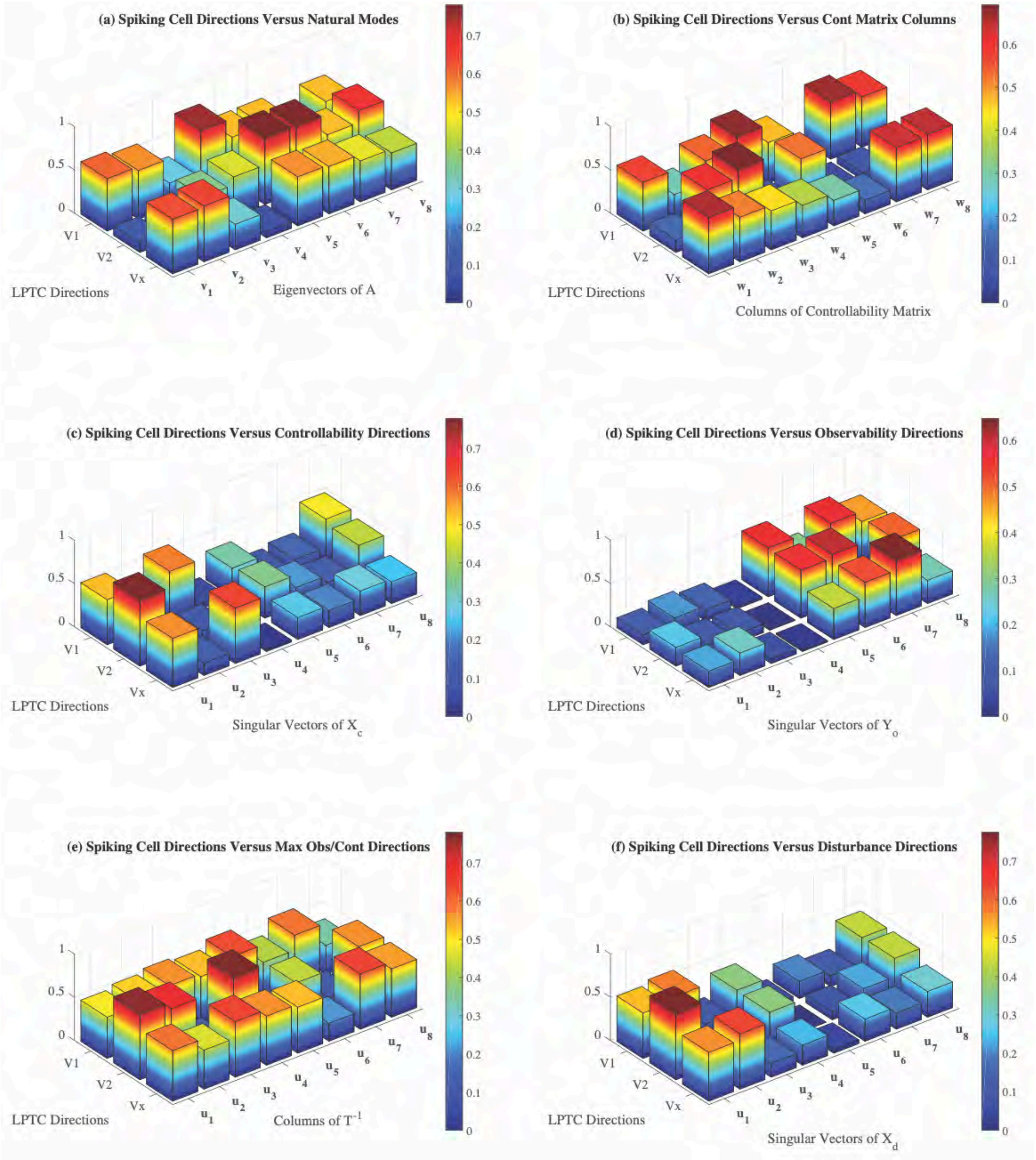

***Figure 67**: Spiking cell (ipsilateral side only) correlations with dynamically significant directions; (a) natural modes, (b) independent columns of the controllability matrix, (c) controllability gramian, (d) observability gramian, (e) joint cont/obs, (f) disturbance sensitivity.*

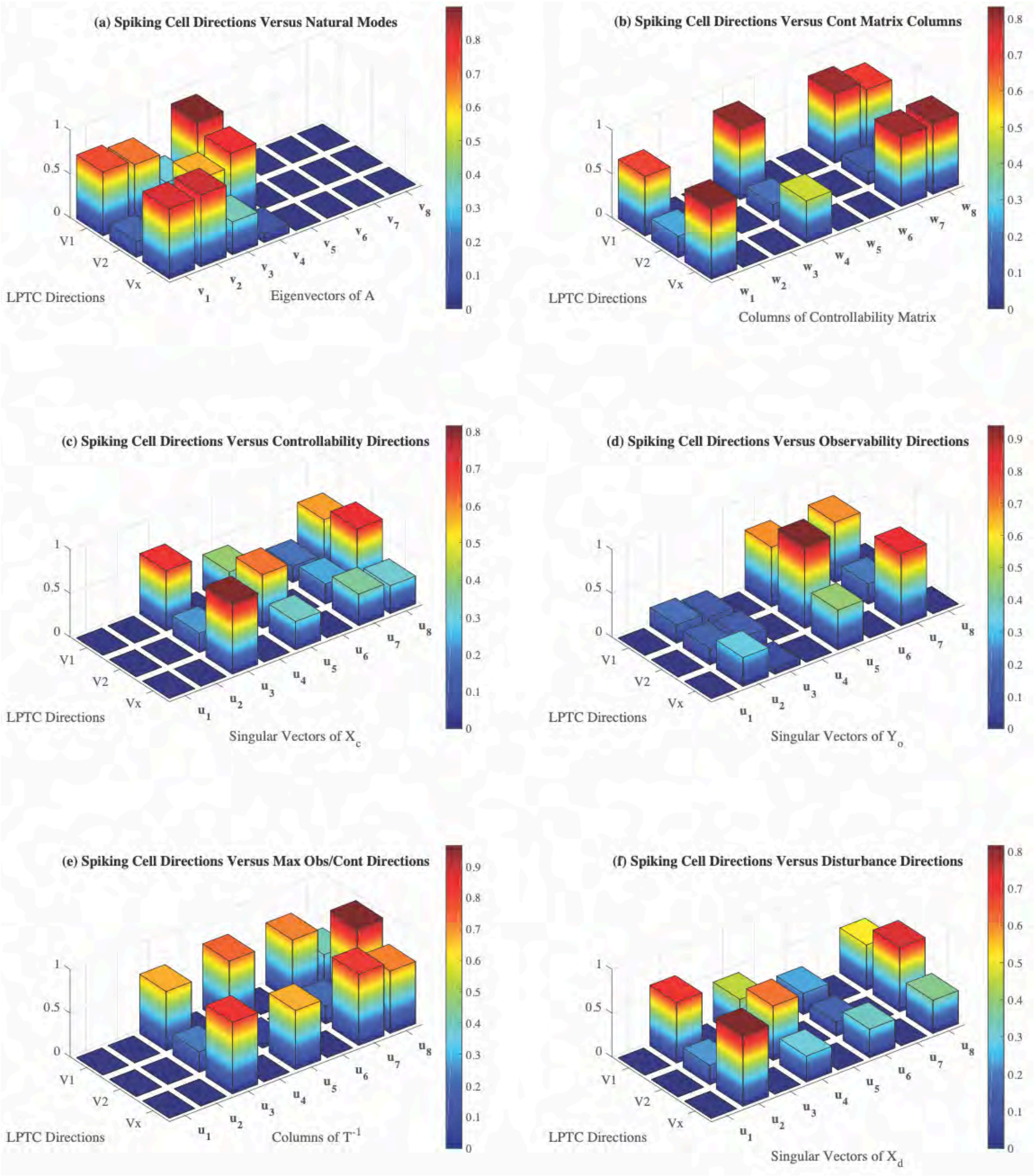

***Figure 68**: Spiking cell (right plus left) correlations with dynamically significant directions; (a) natural modes, (b) independent columns of the controllability matrix, (c) controllability gramian, (d) observability gramian, (e) joint cont/obs, (f) disturbance sensitivity.*

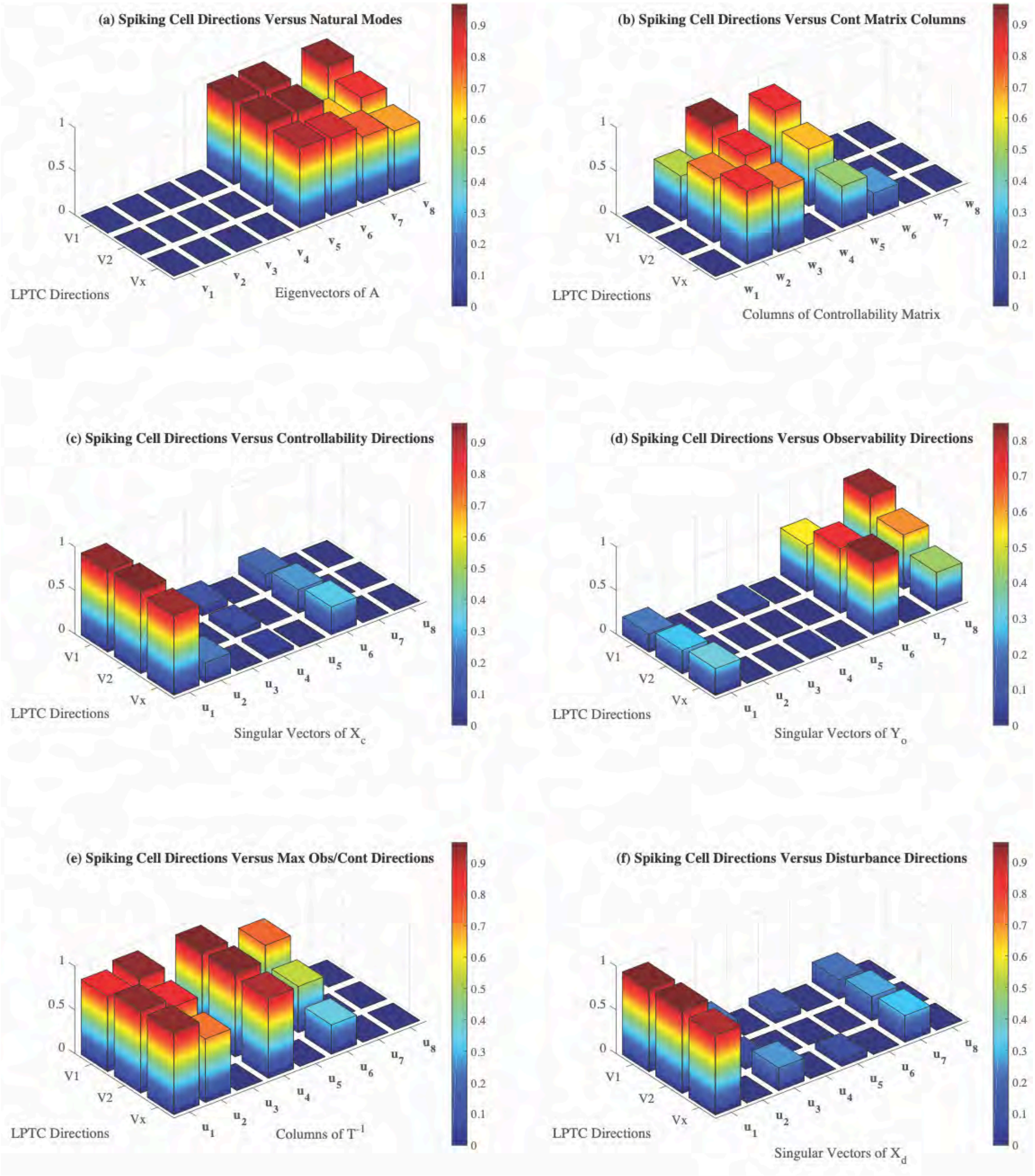

Figure 69: *Spiking cell (right minus left) correlations with dynamically significant directions; (a) natural modes, (b) independent columns of the controllability matrix, (c) controllability gramian, (d) observability gramian, (e) joint cont/obs, (f) disturbance sensitivity.*

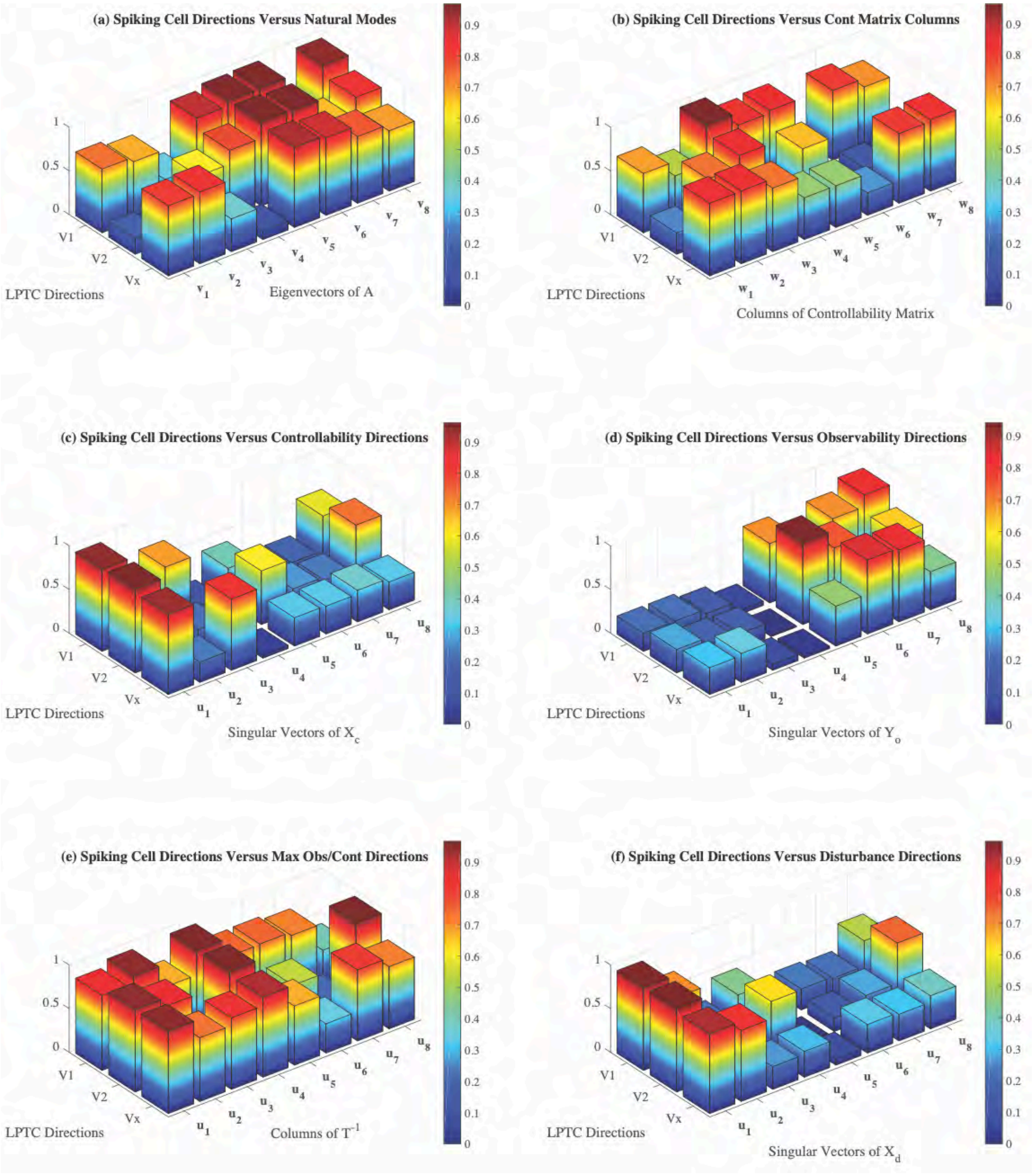

Figure 70*: Spiking cell (maximum over right plus left and right minus left cases) correlations with dynamically significant directions; (a) natural modes, (b) independent columns of the controllability matrix, (c) controllability gramian, (d) observability gramian, (e) joint cont/obs, (f) disturbance sensitivity.*

5.2.5 *Testing the mode sensing hypothesis: How do the LPTC directions* ($\mathbf{C}$ *matrix*) *match dynamically significant directions generated from the* $\mathbf{A}$, $\mathbf{B}$ *and* $\mathbf{G}$ *matrices?*

It is clear from the (a) and (b) subplots in Figures 63-70 that the VS and spiking LPTC directions correlate well with the natural modes and the independent columns of the controllability matrix, i.e., the basis for the reachable space.

The four sets of directions generated from the geometry (singular values σ_j and vectors $\mathbf{u}_j$) of the respective gramians have a natural ranking. In particular, the singular values and vectors of the gramian matrix correspond to the axis directions and lengths of ellipsoids with interpretations described previously in Sections 5.2.3 and 5.2.4. In Figure 71, the direction correlation plots in Figures 63-70 are condensed for each LPTC direction $\boldsymbol{c}_i$ using a weighted average across the corresponding singular values $\sigma_j, j = 1, \cdots, 8$:

$$\kappa_i = \frac{\sum_{j=1}^{8} \frac{|\langle \mathbf{c}_i, \mathbf{u}_j \rangle|}{\|\mathbf{c}_i\|} \sigma_j}{\sum_{j=1}^{8} \sigma_j}$$

This plot tells us how correlated each LPTC direction $\boldsymbol{c}_i$ is with the corresponding set of dynamic directions (controllability, observability, joint cont/obs, disturbance sensitivity) for the VS cells and the spiking cells. For comparison, sets of 10 or 3 random directions (for the VS or spiking cells, respectively) from the unit ball in $\mathbb{R}^8$ were chosen and substituted for the $\boldsymbol{c}_i$ in the above equation. 100 trials were performed, and the results averaged uniformly and plotted.

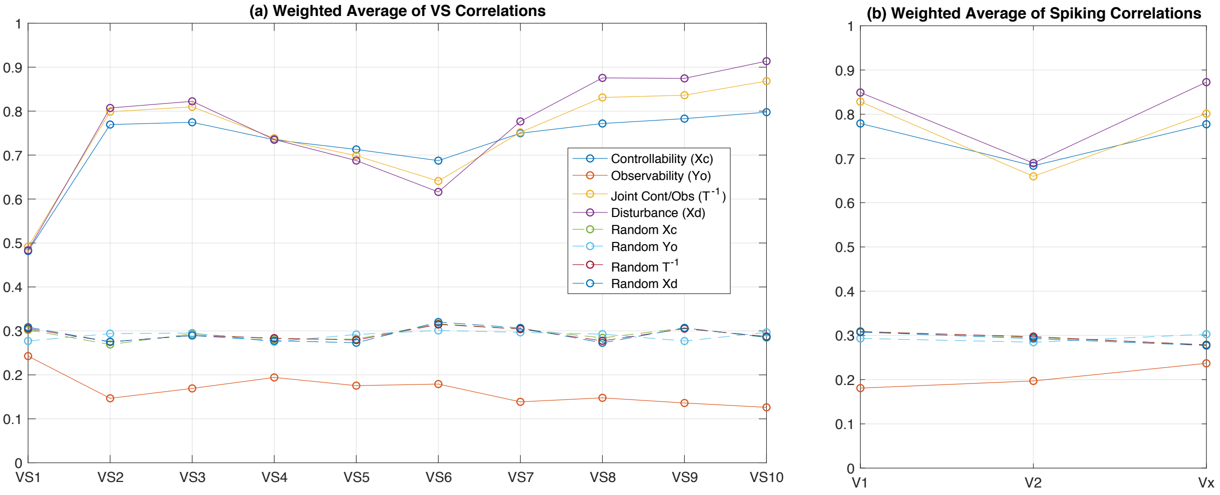

(a) Weighted Average of VS Correlations

(b) Weighted Average of Spiking Correlations

Figure 71: *Weighted average over singular values κ_i for each VS and spiking cell across the various sets of dynamic directions (controllability, observability, joint cont/obs, disturbance sensitivity). The controllability, joint cont/obs and disturbance sensitivities are strongly correlated with the VS cell directions as compared to the average of 100 random 10-direction or 3-direction trials, while the observability directions are not.*

Upon inspection of Figure 71(a) and (b), we see that in general the VS cells and the spiking cells (V1, V2, Vx) have significant weighted correlations with the controllability, joint controllability/observability and disturbance sensitivity directions. The strongest correlations occur in VS2-VS4 (V1) and VS8-VS10 (Vx). It is also interesting to note that the observability directions do not correlate well with any of the VS or spiking cell directions as they do not result in weighted correlation values larger than the sets of random 10-cell or 3-cell trials.

Additionally, we can uniformly average these plots over the set of VS cells $(k = 10)$ and spiking cells $(k = 3)$ to condense the results into a single bar plot for each set of dynamic directions (controllability, observability, joint cont/obs, disturbance sensitivity), shown in Figure 68.

$$\kappa = \frac{\sum_{i=1}^{k} \sum_{j=1}^{8} \frac{|\langle \mathbf{c}_i, \mathbf{u}_j \rangle|}{\|\mathbf{c}_i\|} \, \sigma_j}{k \, \sum_{j=1}^{8} \, \sigma_j}$$

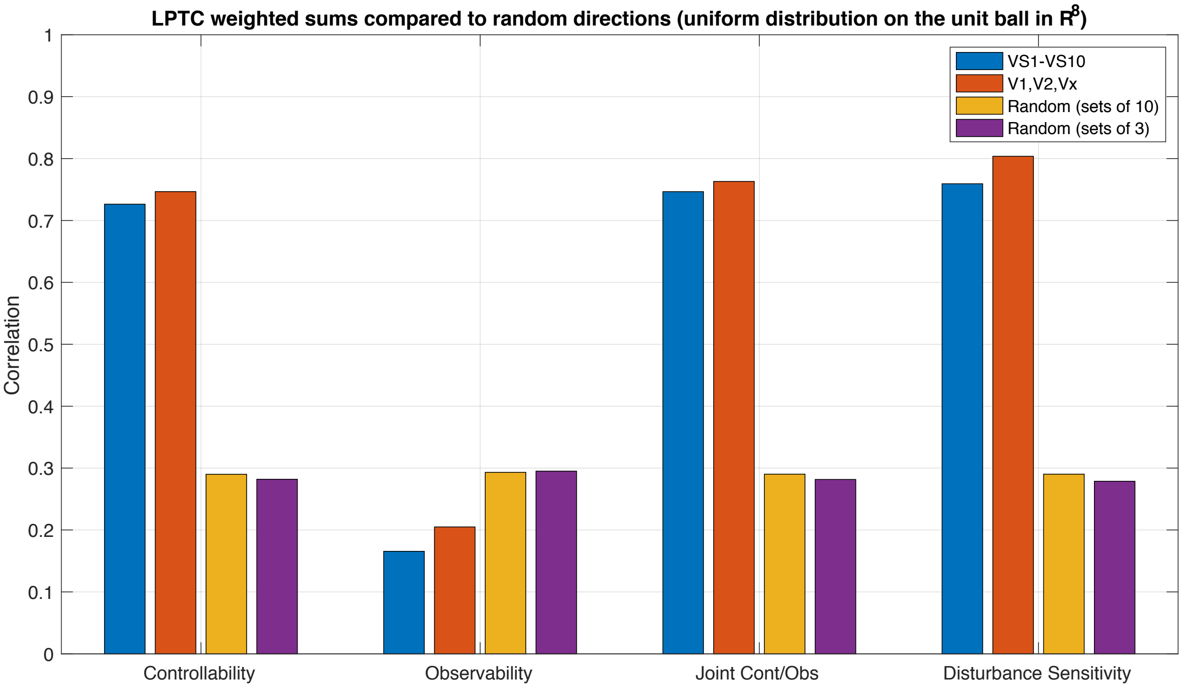

Figure 72*: Average over all VS and spiking cells of the data (Figure 71) across the various sets of dynamic directions (controllability, observability, joint cont/obs, disturbance sensitivity). The controllability, joint cont/obs and disturbance sensitivities are strongly correlated with the VS and spiking cell directions as compared to the average of 100 random 10-direction or 3-direction trials, while the observability directions are not.*

Figure 72 confirms the previous observation – the *VS and spiking LPTCs are correlated well with the controllability, joint controllability/observability and disturbance sensitivity directions but not the observability directions.*

Another interesting parameter to investigate is the equilibrium pitch angle θ_e, which is the angle between the stability axes and the body (principal) axes. To generate the above analysis, we had assumed the head (visual) axes was colinear with the stability axes (Figure 59). We can vary this angle in the code and plot the weighted correlations averaged over the VS and spiking cells (i.e., the magnitude of the bar plots in Figure 72) as a function of the θ_e parameter. Figure 73 effectively shows how the weighted correlations vary as a function of head tilt angle, where the nominal is $\theta_e = 30.4°$. It is very interesting that the spiking cells have an optimum head angle at approximately 30°, whereas the optimum for the VS cells is between 45° and 50° with very little change between 30° and 60°.

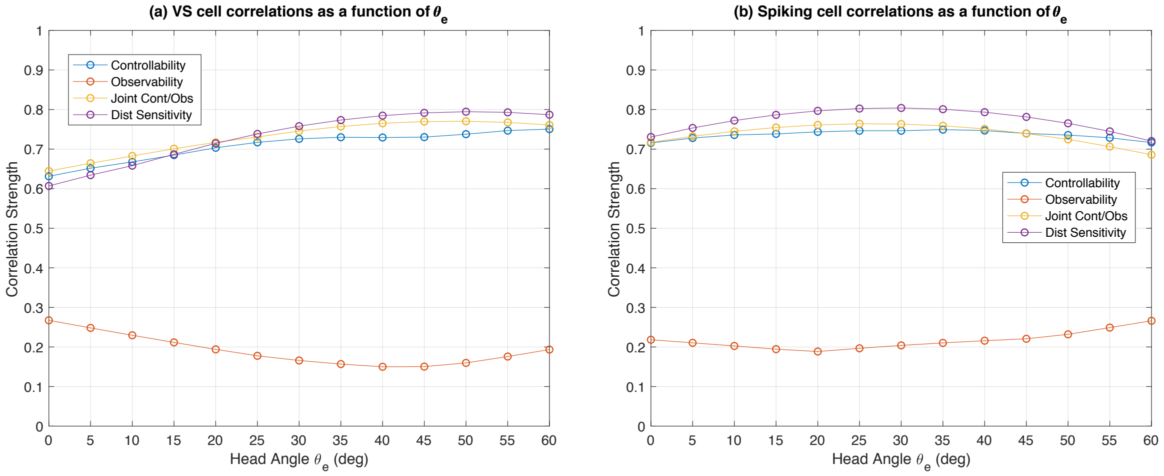

***Figure 73**: LPTC correlations as a function of equilibrium pitch angle θ_e, which is the angle between the stability axes and the body (principal) axes. The nominal value is $\theta_e = 30.4°$, which corresponds to the optimum for the spiking cells (b).*

6 References

Badrya, C., Sridharan A., Baeder, J.D., and Kroninger C.M., (2017) Multi-fidelity coupled trim anlaysis of flapping-wing micro air vehicle flight, *Journal of Aircraft*, 54 (5), 1614-1630.

Borst A. and Weber, F (2011). Neural Action Fields for Optic Flow Based Navigation: A Simulation Study of the Fly Lobula Plate Network. PLoS ONE, https://doi.org/10.1371/journal.pone.0016303

Buschbeck EK and Strausfeld NJ.: The relevance of neural architecture to visual performance: phylogenetic conservation and variation in dipteran visual systems. *Journal of Comparative Neurology*, **383**, 282-304, 1997.

Dahmen, H., Franz, M., & Krapp, H. (2001). Extracting ego-motion from optic flow: limits of accuracy and neuronal filters. In J. M. Zanker & J. Zeil (Eds.), Processing visual motion in the real world – A survey of computational, neural and ecological constraints. Berlin, Heidelberg: New York: Springer Verlag, 143–168.

Dullerud G and Paganini F (2000). A Course in Robust Control Theory – a Convex Approach. Springer, 10.1007/978-1-4757-3290-0.

Fisher, R.A.: Dispersion on a sphere. *Proc. R. Soc. Lond. Ser. Math. Phys. Sci*. **217**, 295–305, 1953. https://doi.org/10.1098/rspa.1953.0064.

Franz, M. O. & Krapp, H. G. (2000). Wide-field, motion-sensitive neurons and optimal matched filters for optic flow. *Biological Cybernetics*, 83, 185–197.

Franz, M. O., Chahl, J. S., & Krapp, H. G. (2004). Insect-inspired estimation of egomotion. *Neural Computation*, 16, 2245–2260.

Haag, J., and Borst, A. (2004). Neural mechanism underlying complex receptive field properties of motion-sensitive interneurons. Nat. Neurosci. 7, 628–634.

Haag J. and Borst A. (2007). Reciprocal inhibitory connections within a neural network for rotational optic-flow processing. Front. Neurosci. https://doi.org/10.3389/neuro.01.1.1.008.2007

Haag J and Borst A.: Electrical Coupling of Lobula Plate Tangential Cells to a Heterolateral Motion-Sensitive Neuron in the Fly. *Journal of Neuroscience*, **28** (53): 14435-14442, 2007.

Hausen, K.: The lobula-complex of the fly: structure, function and significance in visual behaviour. In: Photoreception and Vision in Invertebrates (ed. Ali, M. A.), pp. 523–559. New York: Plenum Press, 1984.

Hausen, K. (1993). Decoding of retinal image flow in insects. Rev. Oculomot. Res., 5, 203–205

Hengstenberg R, Hausen K and Hengstenberg B: (1982) The number and structure of giant vertical cells (VS) in the lobula plate of the blowfly *Calliphora erythrocephala*. J. Comp. Physiol. 149: 163-177.

Hengstenberg R. and Krapp H.: Distribution of roll motion sensitivity in the eyes of *Calliphora*: a comparison between neurons and behaviour. In: Proceedings of the 24th Göttingen Neurobiology Conference, Eds. N. Elsner, H.- U. Schnitzler, Thieme, Stuttgart, p. 349, 1996

Huang J.V., Wei Y. and Krapp H.G.: A biohybrid fly-robot interface system that performs active collision avoidance. *Bioinspir Biomim*, **14**, 065001, https://doi.org/10.1088/1748-3190/ab3b23, 2019.

Humbert, J. S., Murray, R. M., & Dickinson, M. H. (2005). Sensorimotor convergence in visual navigation and flight control systems. In Proceedings of the 16th IFAC World Congress, Praha, Czech Republic.

Humbert, J. S. & Hyslop, A. (2010). Bio-inspired visuomotor convergence. *IEEE Transactions on Robotics*, 26(1), 121–130.

Huston, S.J. and Krapp, H.G.: Visuomotor transformation in the fly gaze stabilization system. *PloS Biol*, **6**, 1468–1478, 2008.

Hyslop, A. & Humbert, J. S. (2010). Autonomous navigation in three-dimensional urban environments using wide-field integration of optic flow. *Journal of Guidance, Control, and Dynamics*, 33(1), 147–159.

Koenderink, J.J., Doorn, A.J. van: Facts on optic flow. *Biol. Cybern*. **56**, 247–254, 1987.
Krapp, H.: Repräsentation von Eigenbewegungen der Schmeissfliege *Calliphora erythrocephala* in VS-Neuronen des dritten visuellen Neuropils. PhD Thesis, University of Tübingen, Germany, 1995.

Krapp H.G. and Hengstenberg R.: Estimation of self-motion by optic flow processing in single visual interneurons. *Nature*, **384**, 463-466, 1996.

Krapp, H.G., Hengstenberg, R.: A fast stimulus procedure to determine local receptive field properties of motion-sensitive visual interneurons. *Vision Res.* **37**, 225–234, 1997.

Krapp, H.G., Hengstenberg, B., Hengstenberg, R.: Dendritic Structure and Receptive-Field Organization of Optic Flow Processing Interneurons in the Fly. *J. Neurophysiol.* **79**, 1902–1917, 1998.

Krapp, H. G., et al. (2001). "Binocular contributions to optic flow processing in the fly visual system." Journal of Neurophysiology **85**: 724-734

Krapp H.G. and Wicklein M.: Central processing of visual information in insects. In: Basbaum A.I, Kaneko A., Shepherd G.M., and Westheimer G. (eds) The Senses: A comprehensive reference. Vol. 1, Vision I, Masland R and Albright T.D. (eds.), San Diego, Academic Press, pp. 131-204, 2008.

Land MF and Eckert H.: Maps of the acute zones of fly eyes. *Journal of Comperative Physiology A,* **156**, 525-538, 1985.

Longden, K.D., Wicklein, M., Hardcastle, B.J., Huston, S.J., Krapp, H.G.: Spike Burst Coding of Translatory Optic Flow and Depth from Motion in the Fly Visual System. *Curr. Biol.* **27**, 3225-3236.e3., 2017.

MacFarlane, K., Bush, B., Faruque, I., Humbert, J.S., and Baeder, J.D. (2011) Quasi-Steady and Computational Aerodynamics Applied to Hovering Drosophila Dynamics, 29th AIAA Applied Aerodynamic Conference, Honolulu, Hawaii.

Moore B. Principal Component Analysis in Linear Systems: Controllability, Observability, and Model Reduction. *IEEE Transactions on Automatic Control*, 26, pp. 17-32, 1981.

Nagesh, I., Walker, S. M., and Taylor, G. K., (2019) Motor output and control input in flapping flight: a compact model of the deforming wing kinematics of manoeuvring hoverflies, Journal of the Royal Society Interface, 16 (161).

Parsons M.M., Krapp, H.G., and Laughlin S.B.: Sensor fusion in identified visual interneurons. *Curr. Biol.*, **20**(7), 624-628, 2010

Petrowitz R., Dahmen H., Egelhaaf M., and Krapp H.G.: Arrangement of optical axes and the spatial resolution in the compound eye of the female blowfly. *Journal of Comparative Physiology A*: **186**: 737-746, 2000.

Sun M, Wang J and Xiong Y.: Dynamic flight stability in hovering insects. *Acta Mech Sin* **23**, 231–246. DOI 10.1007/s10409-007-0068-3, 2007.

Taylor G.K. and Krapp H.G.: Sensory systems and flight stability: What do insects measure and why? *Advances in Insect Physiology*, **34**, 231 – 316, 2007.

Watson, G.S.: The Statistics of Orientation Data. *J. Geol.* **74**, 786–797, 1966. https://doi.org/10.1086/627211.

Zhou, K., et al. (1999). "Balanced Realization and Model Reduction for Unstable Systems." International Journal of Robust and Nonlinear Control **9**: 183—198.

Zhu, H. J., Meng, X. G. and Sun, M.: Forward flight stability in a drone-fly. *Scientific Reports.* **10** (1): 1975-5. DOI: 10.1038/s41598-020-58762-5, 2020.